Colossal Magnetoresistance and the Giant Magnetocaloric Effect in Transition Metal Compounds

By

Wei Li

A Thesis Submitted to the Faculty of Graduate Studies in Partial Fulfillment of the Requirements for the degree of

DOCTOR OF PHILOSOPHY

Department of Physics
University of Manitoba
Winnipeg, Manitoba

THE UNIVERSITY OF MANITOBA

FACULTY OF GRADUATE STUDIES

*****

COPYRIGHT PERMISSION

Colossal Magnetoresistance and the Giant Magnetocaloric Effect in Transition Metal Compounds

BY

Wei Li

A Thesis/Practicum submitted to the Faculty of Graduate Studies of The University of Manitoba in partial fulfillment of the requirement of the degree

Of

Doctor of Philosophy

Abstract

The magnetic properties of several doped manganites displaying colossal magnetoresistance (CMR) and of Ni-Mn-Ga alloys exhibiting a giant magnetocaloric effect (GME) have been investigated.

An analysis of the magnetic critical behaviour of a single crystal $La_{0.73}Ba_{0.27}MnO_3$, based on the use of modified Arrott plots, reveals that the 3D Heisenberg model best describes the critical behaviour of both exponent and critical amplitude values. Around 200 K, some 45 K below T_c, a structural phase transition from a high moment/temperature rhombohedral (*R*) phase to a lower moment/temperature orthorhombic (*O*) phase is observed in both the ac susceptibility and zero field cooled/field cooled (ZFC/FC) data. Similar studies on single crystal $La_{0.73}Ca_{0.27}MnO_3$ reveal for the first time a phase transition with simultaneous characteristics of both first-order and second-order phase change. These two features are coincident in the field and temperature plane, a previously unreported feature of the magnetic behaviour of manganites.

Detailed studies on a series of polycrystalline $(La_{1-x}Nd_x)_{0.67}Pb_{0.33}MnO_3$ ($0 \leq x \leq 1$) samples reveal that this system displays a phase transition from a ferromagnetic metal to a paramagnetic insulator for all x, characteristics typical of double exchange systems. Substitution of Nd^{3+} on the rare-earth site significantly changes the corresponding average A site radius and its variance. The disorder arising from ion size mismatch and site distribution plays a key role. 3D Heisenberg exponents have been extracted in highly doped samples (x = 1, 0.8). Variable range hopping processes has been found predominately in the high-temperature regime, especially at intermediate doping levels, a result which is consistent with a distribution of allowed electronic energy levels arising from both spin and site disorder.

Studies of the magnetocaloric effect were carried out on the ferromagnetic shape memory alloys system – Ni-Mn-Ga. This system typically possesses two types of phase transitions: a first-order structural and magnetic (order-order) phase transition and a higher temperature second-order ferromagnetic to paramagnetic (order-disorder) phase transition. The temperatures of both phase transitions are very sensitive to composition. By a careful compositional tuning, a maximum magnetic entropy change of -20.4 J $kg^{-1}K^{-1}$ has been produced in a field of 50 kOe in $Ni_{55.2}Mn_{18.6}Ga_{26.2}$. This enhanced magnetic entropy change has been traced to the coincidence of first-order/metamagnetic structural transition with a second-order phase transition. The larger magnetocaloric effect and ease of preparation make this system a promising candidate for magnetic refrigeration.

Acknowledgements

I am grateful to my supervisor, Dr. Gwyn Williams, for his guidance and encouragement during this study. It was a great experience to work with him and I benefited in many ways.

I would like to express my thanks to Dr. H. P. Kunkel and Dr. X. Z. Zhou for their invaluable assistance in completing this study. I would also like to thank Dr. R. M. Roshko for his instruction and discussions.

And last, but not least. I want to express special thanks to my newly-married wife, Zhan Li, for her understanding and encouragement during this study.

Table of Content

Chapter 1 Introduction **1**

Chapter 2 Phase Transitions and Critical Exponents **9**

2.1 Phase transitions and their classifications 9

2.2 Landau theory of the magnetic phase transitions 11

2.3 Critical exponents and universality 15

2.4 A treatment of the critical behaviour 18

2.5 (Modified) Arrott Plots and the Banerjee Criterion 23

Chapter 3 Experimental Apparatus-Quantum Design PPMS 6000 System **28**

3.1 Description of the equipment 28

3.2 The PPMS probe 28

3.3 The AC Measurement System (ACMS) of the PPMS 32

3.4 DC Magnetization measurements 34

3.5 AC magnetization Measurements 36

3.6 Demagnetization corrections 38

Chapter 4 Magnetic Phase Transitions in Several Systems with CMR Effects .. **41**

4.1 A brief introduction to Colossal Magnetoresistance (CMR) effects 41

4.2 A basic description of doped manganites 44

4.3 Electronic properties of manganites and double exchange 47

4.4 Magnetic polarons and transport behaviour in manganites 50

4.5 Critical analysis of single crystal $La_{0.73}Ba_{0.27}MnO_3$ 56
4.5.1 General Review 56
4.5.2 Critical behaviour in the low and medium fields 60
4.5.3 Critical Amplitude analysis 67
4.5.4 Critical analysis at higher fields 71
4.5.5 Discussions and conclusion 75

4.6 Behaviour of single crystal $La_{0.73}Ba_{0.27}MnO_3$ in the ferromagnetic regime 78

4.7 The nature of the phase transition in single crystal $La_{0.73}Ca_{0.27}MnO_3$ 87
4.7.1 Overview of the phase transitions in $La_{1-x}Ca_xMnO_3$ 87
4.7.2 Evidence suggesting a first-order phase transition 90
4.7.3 Evidence suggesting a second-order phase transition 96
4.7.4 The observation of coincident of 1st and 2nd order phase transitions 98

4.8 The magnetic properties of $(La_{1-x}Nd_x)_{0.67}Pb_{0.33}MnO_3$ 102
4.8.1 Sample preparation 102
4.8.2 General features 103
4.8.3 The critical behaviour of $(La_{1-x}Nd_x)_{0.67}Pb_{0.33}MnO_3$ 107
4.8.4 Conclusions 122

4.9 Transport behaviour in $(La_{1-x}Nd_x)_{0.67}Pb_{0.33}MnO_3$ 123
4.9.1 General behaviour 123
4.9.2 Transport behaviour in the high temperature regime 128
4.9.3 The role of disorder in $(La_{1-x}Nd_x)_{0.67}Pb_{0.33}MnO_3$ 136
4.9.4 The low temperature behaviour of $Nd_{0.67}Pb_{0.33}MnO_3$ 140
4.9.5 Conclusions 141

Chapter 5 The Magnetocaloric Effect (MCE) in the Shape Memory Alloy Ni-Mn-Ga System 143

5.1 A introduction to the Magnetocaloric Effect (MCE) 143

5.2 The thermodynamic theory of the MCE 144

5.3 MCE in paramagnets 147

5.4 Room temperature GMCE materials and magnetic refrigeration 149

5.4.1 GMCE studies near room temperature 149

5.4.2 Applications of GMCE- Magnetic Refrigeration 153

5.5 The measurement of the magnetocaloric effect 156

5.5.1 Direct Measurement 157

5.5.2 Indirect measurement from magnetization isotherms 158

5.5.3 Indirect measurement from specific heat data 159

5.6 The properties of the Heusler alloy Ni_2MnGa 160

5.7 Sample preparation and measurement techniques 164

5.8 The relationship between sequential magnetic phase transitions and MCE in the Ni-Mn-Ga system 166

5.8.1 General overview 166

5.8.2 Analysis for $Ni_{52.9}Mn_{22.4}Ga_{24.7}$ with sequential magnetic phase transitions 170

5.8.3 Analysis for $Ni_{55.2}Mn_{18.6}Ga_{26.2}$ with merged 1^{st} and 2^{nd} order phase transitions 179

5.8.4 Analysis for $Ni_{57.2}Mn_{15.9}Ga_{27.0}$ with a pure 2^{nd} order phase transition 187

5.8.5 Discussion and conclusions 190

5.8.6 Advantages of Ni-Mn-Ga system as promising refrigerants 192

Chapter 6 Concluding Summary **195**

References **201**

Chapter 1

Introduction

The presence of magnetism in substances gives rise to many interesting effects, influencing many physical properties (transport, optical, thermal, elastic, etc). Fundamentally, these effects arise from the coupling between the different physical properties. Clearly, then such properties will also reflect the presence of a magnetic phase transition – first-order, second-order or both, and indeed will show some dramatic changes in the vicinity of the critical temperature (T_c, T_N). This thesis focuses on two such important effects, viz. (i) coupling between the magnetic and the transport behaviour, namely, the magnetoresistance and (ii) magnetic-thermal coupling, specifically, the magnetocaloric effect.

The magnetoresistance is the relative change in the electrical resistance of a material on the application of an applied field; the magnetoresistance is quite small ($\leq$ 5%) in conventional metals [1]. However, the discovery of a very large magnetoresistance - termed colossal magnetoresistance (CMR) - has renewed interest in this topic, which is discussed in detail by Ramirez [2]. The CMR effect stimulated intense research into the properties of the manganese perovskites. From an applications perspective, this could lead to the development of a new generation of

electronic devices based on electron spin rather than charge, namely, a new generation of "spintronic" devices, which could be smaller, more versatile and more robust than those based currently on silicon chips and circuit elements [3]. In addition, an understanding of the CMR effect may also provide insight into the behaviour of the superconducting cuprates as well as the manganites – both display similar structural features and exhibit semiconducting behaviour at high temperature, but the low temperature superconducting phase of the cuprates is often replaced by magnetic order in doped manganites. From a fundamental point of view, CMR in doped manganite systems provides a natural platform to investigate strong coupling between spin, charge and lattice degrees of freedom, especially to explore the currently poorly understood coupling between electronic and phononic (lattice vibrations) degrees of freedom [4].

CMR effects are predominately found in manganese based perovskite oxides; these oxides have a general formula $A_{1-x}B_xMnO_3$ where A is typically a trivalent rare earth ion and B a divalent alkaline ion. Divalent cation substitution at the A sites introduces Mn^{4+} ions in order to maintain charge neutrality. In these doped manganites, the so-called double exchange mechanism was originally believed to be the dominant interaction, requiring a hopping of charge carriers from a Mn^{3+} to a Mn^{4+} ion through an intermediate oxygen ion. This mechanism was first proposed by Zener [5], and then developed by Anderson and Hasegawa [6]. These authors treated the core spin of each Mn ion classically, but the mobile electron quantum

mechanically and found that the Zener level splitting induced by this mechanism is proportional to $\cos(\theta/2)$; this contrasts with the $\cos(\theta)$ angular dependence of both direct and superexchange interactions, where θ is the classical angle between the core spins. The double exchange mechanism can explain qualitatively the concurrence of metallic and ferromagnetic behaviour; however, it fails to explain quantitatively the complex detailed behaviour of the doped manganites. This is especially true of the high temperature transport behaviour and the situation around the transition temperature. In order to get a more comprehensive understanding of the doped manganites, the electron-lattice interaction must be taken into account. This includes the effect of the static crystal structure on electron hopping as well as dynamical electron-phonon coupling [4]. The former arises from the ionic size mismatch which can be measured by the so called tolerance factor [7]; the latter is linked to the instantaneous deviation of atoms from their ideal crystallographic positions. The electron-lattice coupling can be tuned by a small change in the chemical composition; for example, a change in the ratio between trivalent and divalent ions at the A site, i.e. changing the average ionic radius of the ions on the A site. Basically, this will modify the Mn-O-Mn bond angle, (which is 180^0 in the ideal perovskite structure) between 150^0 and 180^0 for different compositions and substitutions [8, 9]. The bond angle, as well as the bond length, is closely related to the magnetic and transport properties of the doped manganites. For instance, the Curie temperature, T_c, increases with a decrease in the bond angle and the residual resistivity increases by an order of

magnitude when the bond angle decreases [2]. This thesis focuses on investigations of the effects of substitution at the rare earth site at fixed divalent cation doping; in other words, the ratio of Mn^{3+}/Mn^{4+} is held constant while changes are made to the average A site radius. It is known [10] that such substitution induces disorder arising from ionic size mismatch between the various ions at this same crystallorgraphic site; it also affects the lattice parameters and bond angle, thus the band structure and bandwidth. In these types of systems, the correlation between the paramagnetic/ferromagnetic phase transition and the insulator/metal transition are investigated, focusing on the detailed critical analysis of data acquired near the magnetic critical temperature.

Single crystal specimens, having many fewer grain boundaries and defects than their polycrystalline counterparts, provide an ideal platform to investigate the nature of these phase transitions. Comparisons of transport studies [11] on polycrystalline and single crystal samples suggest that the scattering from grain boundaries also plays a significant role, especially at low temperature. In this thesis, two single crystal specimens - $La_{0.73}Ca_{0.27}MnO_3$ and $La_{0.73}Ba_{0.27}MnO_3$ - were subjected to detailed critical analysis. Ca doped manganites have a smaller average A site cation radius than their Ba doped counterparts, and they exhibit complex physical behaviour due to both orbital and charge ordering phenomena [12]. Among the optimally doped manganites $LaAMnO_3$ (A=Ca, Sr, Ba), Ba doping produces the largest mean A

site radius with lattice parameters close to those of the ideal cubic structure, and the associated Mn-O-Mn bond angle is closest to 180° [8, 13].

The second section of this thesis concentrates on magnetic - thermal coupling, i.e. the magnetocaloric effect. The magnetocaloric effect reflects the thermal response of materials to the application or removal of an external magnetic field. In the presence of a magnetic field, the spin aligns and the magnetic entropy decreases. Under adiabatic conditions (for which the total entropy remains constant), the material heats up; with removal of the field, the magnetic entropy increases and the material cools. This effect was first discovered by Warburg in 1881 in pure iron [14] and it is an intrinsic property of all magnetic materials. Its most famous early application was in adiabatic demagnetization refrigeration [15] to achieve low/extremely low temperature in a small volume. Research interest in this area was enhanced significantly with the discovery of a giant magnetocaloric effect (GMCE) in the Gd-based $Gd_5(Si_2Ge_2)$ system [16] and the transition-metal-based (MnFe)(PAs) system [17], where the enhanced magnetic entropy change is due to a concomitant first-order magnetic and crystallographic structural phase transition. The discovery of GMCE makes magnetic refrigeration a practical possibility. In 1997, the Astronautics Corporation of America and the Ames Laboratory jointly demonstrated that magnetic refrigeration is a viable technology for applications near room temperature, including large scale building air conditioning [18]. This thesis focuses on the Ni-Mn-Ga system, which was originally studied because it displayed shape memory

effects and superelasticity [19]. This system usually possesses two well-separated phase transitions: a low temperature structural martensitic to austenitic first-order phase transition and a higher temperature ferromagnetic-paramagnetic second-order phase transition. It is, therefore, an excellent choice to investigate the relationship between the MCE and the order of the phase transitions. Motivation for the above investigation arose as a result of studying single crystal $La_{0.73}Ca_{0.27}MnO_3$, where a simultaneously occurrence of first-order and second-order phase transitions was first observed. The coincidence of a first-order magnetic transition and its attendant structural phase transition with a second-order magnetic transition leads to an enhanced GMCE in $Ni_{55.2}Mn_{18.6}Ga_{26.2}$.

As mentioned above, both CMR and GMCE relate closely to the underlying phase transitions. The identification of the order of the phase transition is a principal task of the present study, and (modified) Arrott plot techniques were utilized in an attempt to do so. For well-defined second order phase transitions, critical exponents describing the behaviour of various physical quantities near the critical point are deduced, and these, in turn, are related to the nature of the underlying interactions. The scaling approach provides an effective and simple way to establish functional relationships between critical exponents and relevant physical quantities via power laws. This approach is based on one assumption, namely, near the critical point the correlation length is the only characteristic length scale in terms of which all other quantities with the appropriate dimensions are to be measured.

In terms of organisation, this thesis is divided into two major sections based on the two topics that are emphasized – CMR and GMCE. Prior to a detailed discussion of these two effects, phase transitions, as well as their classification, are introduced on the basis of the Landau theory in chapter 2, and then critical exponents and universality are discussed. Two approaches for extracting critical exponents are utilised, one is based on field and temperature dependent ac susceptibility data and the second uses the magnetization isotherms around the critical region (the so-called (modified) Arrott Plot).

A brief description of the experimental apparatus and measurement techniques is presented in chapter 3. This begins with the Quantum Design PPMS 6000 system which was used to carry out magnetic properties measurements, emphasizing the role of its principal component - the ACMS probe. Then the AC/DC magnetization/susceptibility measurement principles, as well as the demagnetization factor corrections, are reviewed.

The CMR effect, a basic property of the doped manganites, together with electronic and transport mechanisms in the doped manganites are introduced in chapter 4. Subsequently, magnetic data from a single crystal $La_{0.73}Ba_{0.27}MnO_3$ specimen are analyzed in terms of its structural and magnetic phase transitions. Following this, magnetic data on a single crystal $La_{0.73}Ca_{0.27}MnO_3$ sample are analysed to reveal a novel type of phase transition around the critical temperature, T_c

$\approx$ 232 K. Finally, a summary of an investigation of both the magnetic and transport properties of a series polycrystalline $(La_{1-x}Nd_x)_{0.67}Pb_{0.33}MnO_3$ samples is provided.

In chapter 5, the MCE and its thermodynamic basis are introduced, and then magnetic refrigeration is reviewed with particular reference to materials with GMCE near room temperature. The study of a series of composition related Ni-Mn-Ga samples is reported and discussed, based on the relationship between the GMCE and the associated phase transitions. Prior to this, the properties of the parent compound – Heusler Ni_2MnGa - are introduced. The principal conclusions of this thesis are summarized in chapter 6.

Chapter 2

Phase Transitions and Critical Exponents

2.1 Phase Transitions and their Classifications

A phase transition is the transformation of a thermodynamic system from one phase to another. The phase transition is often accompanied by an abrupt change in one or more physical properties, such as the volume, specific heat, magnetization, susceptibility, etc. Phase transitions can occur in many systems; some typical examples include: the phase transition between liquid, solid and gas phases, the emergence of superconductivity in certain metals when cooled below a critical temperature, quantum condensation of bosonic fluids (such as Bose-Einstein condensation and the superfluid transition in liquid helium) amongst others. In particular, in magnetic systems, due to the diversity of phases possible - ferromagnetic, paramagnetic, antiferromagnetic, ferrimagnetic, superparamagnetic - the phase diagram can be extremely complicated. Generally speaking, a phase transition can occur when the Gibbs free energy in a system is non-analytic (the

variable cannot be expressed as a convergent power series) for some specially selected variables.

The earliest classification of phase transitions was on the basis of the level to which a system is non-analytic, the so called Ehrenfest classification scheme. Following this scheme, a first-order phase transition is defined as one in which the first derivative of the Gibbs free energy with respect to a thermodynamic variable exhibits a discontinuity. For example, the martensitic structural transition in Ni-Mn-Ga shape memory alloys around the critical temperature is characterized as a first-order phase transition. For a second-order phase transition, the second derivative of the Gibbs free energy shows a discontinuity, which, in a magnetic system, is reflected in the susceptibility, the second derivative of the free energy with respect to the magnetic field. In essence the Ehrenfest classification scheme is based on a mean field approach which is flawed in the vicinity of the phase transition since it neglects the role of thermodynamic fluctuations. Thus the Ehrenfest classification scheme is not a sophisticated theory and it was soon replaced by a more modern classification, based on the role of the latent heat. This leads to two classes of phase transitions: discontinuous and continuous transitions. Discontinuous phase transitions are those involving a change of latent heat. During such a transition a system either absorbs or releases a fixed (and typically large) amount of energy. Because energy cannot be instantaneously transferred between the system and its environment, discontinuous (or first-order) transitions are associated with "mixed-phase regimes" in which some

parts of the system have completed the transition while others have not. Mixed-phase systems are difficult to study, because their dynamics are difficult to control. A continuous phase transition or a second-order phase transition usually does not involve a latent heat. Besides these two basic types of phase transitions, there are several special transitions known as infinite order phase transitions. They are continuous, but break no symmetries. The most famous example is the Berezinsky-Kosterlitz-Thouless transition in the two-dimensional XY model [20]. Many quantum phase transitions in two-dimensional electron gases also belong to this class. However, this kind of phase transition is beyond the scope of the discussion relevant to this thesis.

2.2 Landau Theory of Magnetic Phase Transitions

Landau theory represents an early attempt to find a general theory for second-order/continuous phase transitions. Landau provided a different approach to thermodynamic potentials [21] based on two assumptions. One is that the free energy in any system is analytical; the second is that the free energy follows the symmetry of the Hamiltonian. Using these two criteria, an order parameter for the system was introduced and the free energy was expanded as a power series in terms of this order parameter. Generally, the order parameter is a function of temperature and is defined to be zero in the high symmetry phase and nonzero in the lower symmetry ordered

phase. This treatment of phase transitions affected the physics profoundly, even after the development of more complicated and newer methods such as those that examine the so called critical exponents based on the renormalization group theory.

For a magnetic system, the order parameter is the magnetization. From general Landau and related thermodynamic theory, it is known, firstly, that the free energy $F(T,m)$ is an analytical function of the magnetization M, and can be expanded in a power series:

$$F(T,m) = F_0(T) + \alpha_0(T)m + \alpha_2(T)m^2 + \alpha_3(T)m^3 + \alpha_4(T)m^4 + \ldots \qquad (2.1)$$

where m is the reduced magnetization

$$m = M_S(T)/M_S(0) \qquad (2.2)$$

$M_S(0)$ is the spontaneous magnetization at $T = 0K$; so m will be much less than one when the temperature approaches the critical temperature, T_c. Thus with m small, higher order terms can be neglected in the critical region. If the system possesses inversion symmetry, only even terms in the power series need be kept. In other words, reversing the direction of the magnetization and thus changing the sign ofm should not affect the value of the free energy; thus the free energy in equation (2.1) can be rewritten as

$$F(T,m) = F_0(T) + \alpha_2(T)m^2 + \alpha_4(T)m^4 + \ldots \qquad (2.3)$$

Notice that the $F_0(T)$ term can also be ignored in practice since the energy zero is generally arbitrary. Around the critical region, where m is small, only the first several

terms in the expansion need be retained; thus, the free energy can be further simplified as:

$$F(T,m) = \alpha_2(T)m^2 + \alpha_4(T)m^4 \tag{2.4}$$

The equilibrium state can be found by minimizing the free energy F(T,m) with respect to the order parameter m, yielding

$$\frac{\partial F(T,m)}{\partial m} = 2\alpha_2(T)m + 4\alpha_4(T)m^3 = 0 \tag{2. 5}$$

Furthermore, Equation (2.5) should yield a minimum rather than maximum, so there is a stability condition

$$\frac{\partial^2 F(T,m)}{\partial m^2} > 0 \tag{2.6}$$

Both equations (2.5) and (2.6) require that the coefficient $\alpha_4(T)$ be a positive number; this also ensures that $F(T,m)$ increases with in relatively far away from the minima.

The solutions for equation (2.5) are:

$$m = 0 \tag{2.7}$$

$$m = \pm\sqrt{\frac{-\alpha_2(T)}{2\alpha_4(T)}} \tag{2. 8}$$

Since $\alpha_4(T) > 0$, the nature of above solutions strongly depend on the sign of the expansion coefficient $\alpha_2(T)$.

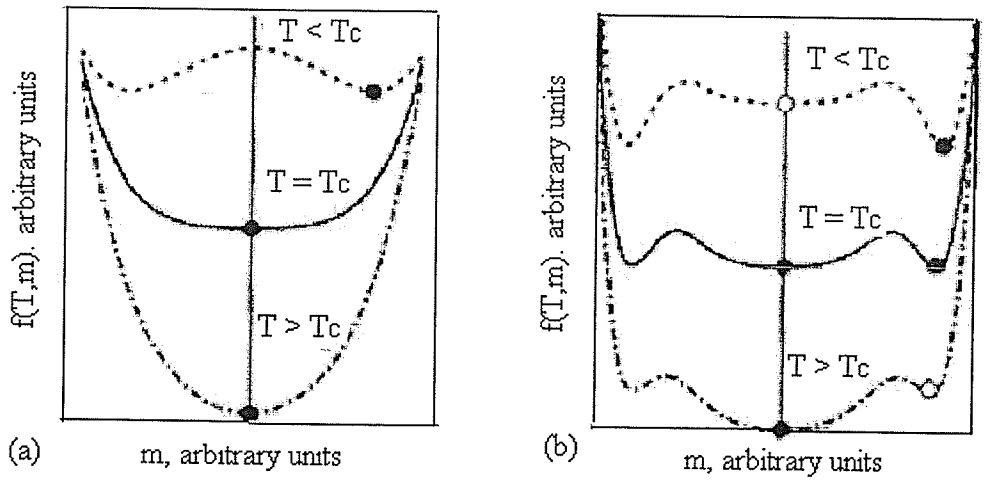

Figure 2.1 The Gibbs free energy $F(T,m)$ *as a function of the reduced magnetization* m *for (a) a second-order phase transition and (b) first-order phase transition.*

Figure 2.1 shows the shape of the isothermal free energy curves $F(T,m)$ for these two solutions. Obviously, when $T \to T_C$, if $\alpha_2(t)$ is positive, there is only a trivial solution, $m = 0$; for a negative $\alpha_2(t)$, there are two real non-trivial solutions for the free energy. In essence, this reflects the nature of the first- and second-order phase transitions. Namely, when the temperature approaches the critical temperature, the free energy in a continuous/second-order phase transition only has a single minimum at $T=T_c$ (Figure 2.1a). However, for first-order transitions, the free energy minima correspond to three m values; $m = 0$ and $m = \pm m_0$ (Figure 2.1 b). The corresponding relations can be further clarified in the form of magnetization

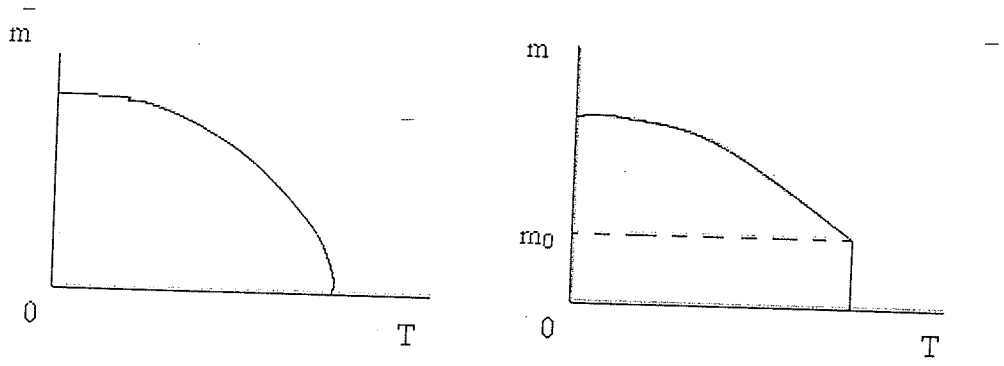

Figure 2.2 Reduced magnetization m as a function of temperature for a second-order phase transition (a) and a first-order phase transition (b).

curves as a function of temperature, as shown in Figure 2.2. For a first-order phase transition at the critical temperature (see Figure 2.2 (b)), two phases coexist; one has a zero magnetization, the other has a finite magnetization m_0. This is the origin of the discontinuity in the magnetization for a first-order transition.

2.3 Critical Exponents and Universality

A second-order/continuous phase transition is much easier to investigate than a first-order/discontinuous phase transition, due to the absence of a latent heat; much interesting work has been done on second-order/continuous phase transitions. Second-order/continuous phase transitions can be characterized by so-called critical exponents which describe the behaviour of various physical quantities near critical points [22]. For a magnetic system, it has been shown that a number of physical

properties such as the specific heat(C), magnetization (M), susceptibility (χ) and the correlation length (ξ) exhibit a power law dependence on external variables in the vicinity of the critical region. Some typical asymptotic power laws are listed below in terms of the reduced temperature t, which is defined as $t = (T - T_c)/T_c$.

1. $C \propto |t|^{-\alpha}$ (2.9)

where C is heat capacity (the second derivative of the free energy with respect to temperature) and α is the heat capacity critical exponent.

2. $m \propto |t|^{\beta}$ (2.10)

where m is the reduced magnetization and β is the order parameter critical exponent.

3. $\chi \propto |t|^{-\gamma}$ (2.11)

where χ is the initial susceptibility (the second derivative of the free energy with respect to the field) and γ is the susceptibility critical exponent.

4. $m \propto h^{\delta} \quad (t = 0, h \to 0)$ (2. 12)

where δ is the equation of state critical exponent.

Some of these exponents are related via the Widom equality

$\gamma = \beta(\delta - 1)$ (2. 13)

(An inequality in general, which ensures thermodynamic stability, and becomes an equality under the so-called scaling hypothesis)

Model \ exponents	α	β	γ	δ
Mean field theory	1.75	0.5	1	3
3D Heisenberg	-	0. 369	1. 396	4. 783
3D Ising	0. 11	1. 237	0. 326	4. 789
3D XY model	-	1. 318	0. 349	4. 780
Experimental Data	0. 0-0. 2	0. 30-0. 36	1. 2-1. 4	4. 2-4. 8

Table 2.1 the critical exponents from several model simulations and experimental data.

A careful study of critical exponents in certain kinds of phase transitions exhibits a striking feature – different systems seem to possess the same set of critical exponents, despite their structural differences. This phenomenon is known as universality, and systems displaying the same exponents are said to belong to the same universality class. However, Landau theory overestimates the concept of a universality class, in that all systems belong to the same class. In reality, different systems can belong to totally different universality classes; these include those for the Heisenberg model [23], mean field model [22], 3D Ising model [24], 3D XY model [25], superfluides [26], etc. i.e., the universality class (exponents) shows a model dependence. Landau theory gives exactly the same exponents as mean field theory model calculations, as will be shown in the following chapters.

The critical exponents predicted by various models, as well as those deduced from a selection experimental data, are summarized in Table 2.1. Given the various power

law relations, equation (2.9)-(2.12), critical exponents are often determined experimentally from the slope of log-log plots of relevant data. Besides some basic exponents and relations mentioned above, there are a large number of relationships between the various critical exponents which result from fundamental thermodynamic and statistical mechanical considerations (examples include those due to Fisher, Rushbrooke and Josephson). The treatment of critical behaviour can thus be complicated and difficult, and a number of different approaches have been employed in an attempt to do so.

2.4 A Treatment of the Critical Behaviour– Scaling Theory

Following earlier works by Widom [27], Domb and Hunter [28] and Patashinskii and Pokrovskii [29], Kadanoff [30] proposed the scaling approach to understand critical phenomena. It was intended as an alternative to the direct approach of solving standard models because of the technical difficulties presented by the latter. Using scaling theory it is possible to derive the following general expression for the magnetic equation of state [22]

$$m(t,h) = t^{\beta} F_{\pm}(h / t^{\gamma+\beta}) \tag{2.14}$$

where t is the reduced temperature and $h \sim H/T_C$ (H is the internal field). Based on Landau theory, the function (2.14) appearing here is a universal function for all

systems, and is called the equation of state. It is not difficult to show that this relation can be reduced from three variables (h, t, m) to two $(m/|t|^{\beta}, h/|t|^{\gamma+\beta})$. This reduction of the total number of variables was considered the first important contribution of scaling theory. While the general behaviour of the scaling function $F_{\pm}$, a homogenous function of its arguments, remains unspecified, its asymptotic behaviour for small and large values of its argument will give asymptotic power laws, which will be derived below.

In zero-field, $H = 0 \Rightarrow h = 0$; then $F(h/t^{\gamma+\beta}) \rightarrow F(0) = \text{Const.}$. Equation (2.14) changes to

$m(0,t) \propto Bt^{\beta}$, i.e. the spontaneous magnetization is given by

$$M_s(0,T) = M_S(0)t^{\beta} = M_S(0)\left(1-\frac{T}{T_c}\right)^{\beta} \quad \text{with } T < T_c \tag{2.15}$$

where $M_S(0)$ is the spontaneous magnetization at $T = 0$.

From equation (2.14), the susceptibility, which is the first derivative of the magnetization, m, with respect to field h, is

$$\chi = \frac{\partial m}{\partial h} = t^{\beta}(t^{-(\gamma+\beta)})\dot{F}(h/t^{\gamma+\beta}). \tag{2.16}$$

where $\dot{F}$ is the derivative of F with respect to its argument $h/t^{\gamma+\beta}$, For $h = 0 \Rightarrow \dot{F}(0) = \text{const.}$

and the initial susceptibility becomes $\chi(0,t) \propto Ct^{\beta}t^{-(\gamma+\beta)} = Ct^{-\gamma}$, i.e.

$$\chi(0,T) = \chi_0 t^{-\gamma} = \chi_0 \left(\frac{T}{T_c} - 1 \right)^{-\gamma} \quad \text{with } T > T_c \tag{2.17}$$

At the Curie temperature, $T = T_c \Rightarrow t = 0$; hence $t^{\beta} \to 0$ and $1/t^{\gamma+\beta} \to \infty$. In order to make $m(h,0)$ measurable (a finite value), the variable t in equation (2.14) must be cancelled. Thus, equation (2.14) must have the form

$$m(h,0) \propto t^{\beta} \left(\frac{h}{t^{\gamma+\beta}} \right)^{\beta/\gamma+\beta} = h^{\frac{\beta}{\gamma+\beta}} \tag{2.18}$$

Using the Widom relationship $\beta\delta = \gamma + \beta$, at the Curie temperature T_c, the magnetization as a function of field should follow the power law

$$m(h,0) = Dh^{1/\delta} \tag{2.19}$$

From the above discussion, it can be seen that the static scaling law or homogeneous function approach does not directly produce specific numerical values for any critical point exponents, rather the scaling hypothesis predicts functional relationships between the critical point exponents. In addition, once the general form of the thermodynamic equation of state (2.14) is deduced, which takes the form of a homogeneous function of field and temperature, an alternative way to extract the power law relations, hence the critical exponents can be evaluated.

The susceptibility, equation (2.16), can be rewritten as

$$\chi = h^{-\gamma/(\gamma+\beta)} (h/t^{\gamma+\beta})^{\gamma/(\gamma+\beta)} \dot{F}(h/t^{\gamma+\beta}) = h^{-\gamma/(\gamma+\beta)} H(h/t^{\gamma+\beta}) \tag{2.20}$$

Where $H(x) = x^{\gamma/(\gamma+\beta)} \dot{F}(x)$

From equation (2.20) any function of the susceptibility measured in a fixed field (h=constant), such as a maximum, is predicted to exhibit the following dependence on a reduced temperature, t_m ;

$$\left(\frac{\partial \chi}{\partial t}\right)_{t=t_m} = 0 \qquad \text{ie} \qquad \dot{H}(h/t_m^{\gamma+\beta}) = 0 \tag{2.21}$$

The above equation is satisfied when the argument of the function H is a constant, thus

$$t_m \propto h^{1/\gamma+\beta} \tag{2.22}$$

and using the Widom equality (2.13), the susceptibility at this peak temperature becomes

$$\chi(h, t_m) \propto h^{(1-\delta)/\delta} \tag{2.23}$$

In equation (2.22), $(\gamma+\beta)$ is called the cross-over exponent and the equation itself demonstrates that the peak in the ac susceptibility occurs at a reduced temperature, t_m, which shifts upwards in temperature with increasing magnetic field. Equation (2.23) indicates that the amplitude of the susceptibility peak decreases with increasing field (provided $\delta > 1$) along the cross-over line in the (h,t) plane. The measurement of δ along the cross-over line is clearly independent of the choice of T_c, a particular advantage over the original scaling approach in which not only is T_c required to be well defined, but also the measuring temperature must have sufficient stability.

The physical origin of these susceptibility peaks can be understood as follows; the cross-over line separates two regimes, one is a temperature dominated region

where $(\partial\chi/\partial t)_h < 0$ and the other is field dominated in which $(\partial\chi/\partial t)_h > 0$. According to the fluctuation-dissipation theorem [22], the susceptibility obeys the expression

$$\chi(H,T) \sim \frac{1}{T}(\langle S_z^2 \rangle - \langle S_z \rangle^2) \tag{2.24}$$

In the high temperature regime, $\chi(H,T)$, measured in any fixed field H, varies as T^{-1} since $\langle S_z^2 \rangle \to S(S+1)/3$ and $\langle S_z \rangle \to 0$, thus $\chi \sim S(S+1)/3T$ and $(\partial\chi/\partial t)_h < 0$; here thermal fluctuations are dominant. On the other hand, when the temperature approaches the critical temperature, T_c, from above, any non-zero field drives the magnetization towards saturation, causing a decrease in magnetic fluctuations. This process becomes more marked with increasing field; thus based on the fact that $\langle S_z^2 \rangle - \langle S_z \rangle^2$ is a direct measure of such fluctuation, $\chi(H,T)$ decreases as T approaches T_c from above and $(\partial\chi/\partial t)_h > 0$. A maximum must therefore result from these two opposite temperature dependence. The above behaviour of the susceptibility as a function of temperature and field has been confirmed experimentally in many systems including metallic alloys [31, 32], the pyrochlore $Tl_2Mn_2O_7$ [33], and the single crystal Ba doped perovskite among others. Theoretical model calculations of the temperature dependence of the susceptibility in a Sherrington-Kirkpatrick (SK) like model [34] qualitatively agree with the behaviour predicted by the above equations deduced from the scaling approach, however, such

a model, as expected, displays mean field exponents. Other model approaches investigated recently also confirm this behaviour for so-called Heisenberg system [23].

2.5 (Modified) Arrott Plots and the Banerjee Criterion

For ferromagnetic materials, there is a significant spontaneous magnetization when the temperature is below the Curie temperature. In the vicinity of the Curie temperature, the reduced magnetization, m, is small. Including the contribution to the free energy in the presence of a field, H , the Landau expansion becomes:

$$F(T,m) = \alpha_2(T)m^2 + \alpha_4(T)m^4 - Hm \tag{2.25}$$

where $\alpha_2(T)$ and $\alpha_4(T)$ are coefficients which in general depend on temperature. From the previous discussion, the critical point corresponds to the temperature T_c where $\alpha_2(T)$ changes sign, thus $\alpha_2(T)$ can be expanded in powers of $(T-T_c)$. To leading order, equation (2.25) becomes

$$F(T,m) = \alpha_0(T - T_c)m^2 + \alpha_4(T)m^4 - Hm \tag{2.26}$$

Minimizing the free energy $F(T,M)$ with respect to its parameter m and rearranging the terms, then

$$\frac{H}{m} = 2\alpha_0(T - T_c) + 4\alpha_4(T)m^2 \tag{2.27}$$

This is the basis of the so called Arrott Plot. It was first suggested by Arrott [35] at a conference with no published proceedings, and then discussed (together with other methods used at the time) in an unpublished internal report of the General Electric Co. Arrott plots are widely used for the experimental determination of the Curie temperature. Here, we present a simple derivation from the Landau expansion. A more sophisticated derivation based on the molecular field theory and the Brillouin function can be found in several books on magnetism [36].

Based on the previous discussion, equilibrium and stability conditions require $\alpha_4(T) > 0$ for a second-order/continuous phase transition. Thus the initial slope of a (H/M) vs M^2 plot, which yields the coefficient $\alpha_4(T)$, was used to decide the order of a phase transition. This criterion is sometimes known as the Banerjee Criterion, since it was first proposed by Banerjee [37]. However, in some circumstances, such as for $La_{0.73}Ca_{0.27}MnO_3$, although the initial slopes of Arrott/Banerjee plots are positive, negative slopes appear at a larger value of m. This cannot be simply interpreted as the sign of the coefficient $\alpha_4(T)$; however, it can be fully understood by extending the Banerjee criterion, namely, by including an addition term $\alpha_6(T)m^6$ in the Landau expansion of equation (2.26). Applying the equilibrium and stability conditions will yield a modified slope for a second-order/continuous phase transition, viz.

$$\alpha_4(T) + 3m^2\alpha_6(T) > 0 \qquad (2.28)$$

It is immediately evident from equation (2.28) that in order to ensure a second-order phase transition, the higher-order coefficient $\alpha_6(T)$ should also be positive. Failure to satisfy this equation – a negative slope in higher fields, not simply the initial slope – indicates the appearance of a first-order/discontinuous phase transition. Obviously this criterion can be further extended by including an $\alpha_8(T)m^8$ term, and so on, leading to the conclusion that for a second-order/continuous phase transition, all the coefficients in the Landau expansion should be positive. Any negative coefficients will lead to a first-order/discontinuous phase transition. This modified criterion has been successfully applied to the Ni-Mn-Ga system (discussed in detail in chapter 5), which generally possesses two sequential transitions as a function of temperature.

Once a second-order/continuous phase transition is identified, a set of critical exponents can be extracted based on equations (2.15)-(2.19). The Arrott plot mentioned above provides a effective way to estimate the spontaneous magnetization, $M_s(T)$ and the initial susceptibility, $\chi_i(T)$. In practice, as a result of technical contributions and complications arising from crystalline anisotropy, Arrott plots do not always form perfect straight lines, for data taken in low to moderate applied field, extrapolation from technical saturation, where such contribution are constant / saturated, are employed. A modified form of equation (2.28), known as the Arrott-Noakes equation of state [38], is used in these cases where mean field exponents are not appropriate.

$$\left(\frac{H}{M}\right)^{\frac{1}{\gamma}} = \frac{T - T_C}{T_C} + \left(\frac{M}{M_1}\right)^{\frac{1}{\beta}} \tag{2.29}$$

here M_1 is a material specific constant, and γ and β are general susceptibility and order parameter critical exponents. Equation (2.28) is clearly a special case of the Arrott-Noakes equation with the mean field theory exponents ($\beta = 0.5, \gamma = 1, \delta = 3$). In the several cases, values for γ and β (which show a model dependence) are then chosen so that (2.29) yields a set of straight lines. For $T > T_c$, in the paramagnetic state, the intercept on the horizontal axis gives the inverse of the susceptibility $1/\chi_i(T)$; for $T < T_c$, in the ferromagnetic state, the intercept with the vertical axis gives the spontaneous magnetization, M_s. The straight line isotherm which passes through the origin corresponds to the magnetization curve measured at the Curie temperature (in practice, this usually involves an interpolation between the temperatures of two or so curves having the smallest positive and negative intercepts). Thus the Arrott-Noakes approach provides an alternative way to estimate the ordering temperature, T_c, the spontaneous magnetization, M_S, and the initial susceptibility, $\chi_i(T)$, of bulk magnetic materials experimentally. With these preliminary exponent estimates, the power-law relations, equation (2.15) - (2.19), can be (re)tested until a truly self-consistent exponent set is achieved. Namely, the modified Arrott plot and the power-laws yield the same exponents values. However, in using the (modified) Arrott Plot, the following points should be remembered: (a)

the critical exponents γ and β can vary substantially without a significant change being evident in the modified Arrott plot; many exponent choices can yield a set of straight lines. (b) There is no way to eliminate the inconsistency of the very low field data, which represents averaging over domains magnetized in different directions [38]. The best recourse is to discard the low magnetization data in the fits. (c) Obviously, curvature can be observed far beyond the critical region, when, for example, the magnetization along the critical isotherm shows saturation effects in high fields (i.e. δ increases). Thus this method can only be applied with materials showing weak ferromagnetism at any temperature, with strong magnets in their paramagnetic phase, or in their ferromagnetic phase very close to the critical region.

Chapter 3

Experimental Apparatus – the Quantum Design PPMS Model 6000 System

3.1 Description of the Equipment

Basically, all the susceptibility and magnetization measurements were carried out in a commercial measurement system – a Physical Property Measurement System (PPMS) produced by Quantum Design [39]. A block diagram of the system is shown in figure 3.1. From this diagram it can be seen that the system contains several major components: the CPU board (processor), the motherboard (system integration), the system bridge board (temperature readings), gas valves and gas lines (temperature control), the front panel (user interface) and rear panel (connections), the measurement probe and a helium dewar. In this system a temperature range from 1.8 K to 400 K can be accessed and magnetic field up to 9 Tesla can be produced by a superconducting solenoid.

3.2 The PPMS Measurement Probe [40]

The probe is the key part of the PPMS system and it is located within the liquid helium bath and inside the dewar. Its intricate design incorporates all of the elemental temperature control hardware, the superconducting magnet, the helium level meter, a variety of electrical connections, gas lines and sample puck connectors.

As figure 3.2 shows, there are two concentric tubes - outer and inner vacuum tubes - with a sealed, evacuated region between them. This prevents heat exchange between the sample tube and helium bath from increasing the system's helium consumption. Another vacuum space between the outer and inner vacuum tubes contains reflective super insulation in order to minimize radiative power loss from the helium bath. Inside inner vacuum tube, there is a sample tube which contains two thermometers, and a heater below the connector at the bottom of the sample tube. The sample temperature is monitored by these two thermometers. One is a platinum resistance thermometer and the other is a negative temperature coefficient (NTC) thermometer. The NTC thermometer operates below 100K, while the platinum resistance thermometer works above 80K. In the range 80-100K, a weighted average of the readings from the two thermometers is used. Between the sample tube and the inner vacuum tube, there is a special region called the cooling annulus. Helium exchange gas will flow in and out of this space through the impedance assembly in order to change the temperature of the sample space. The impedance assembly contains a very narrow tube, a heater to warm this tube and a thermometer. In

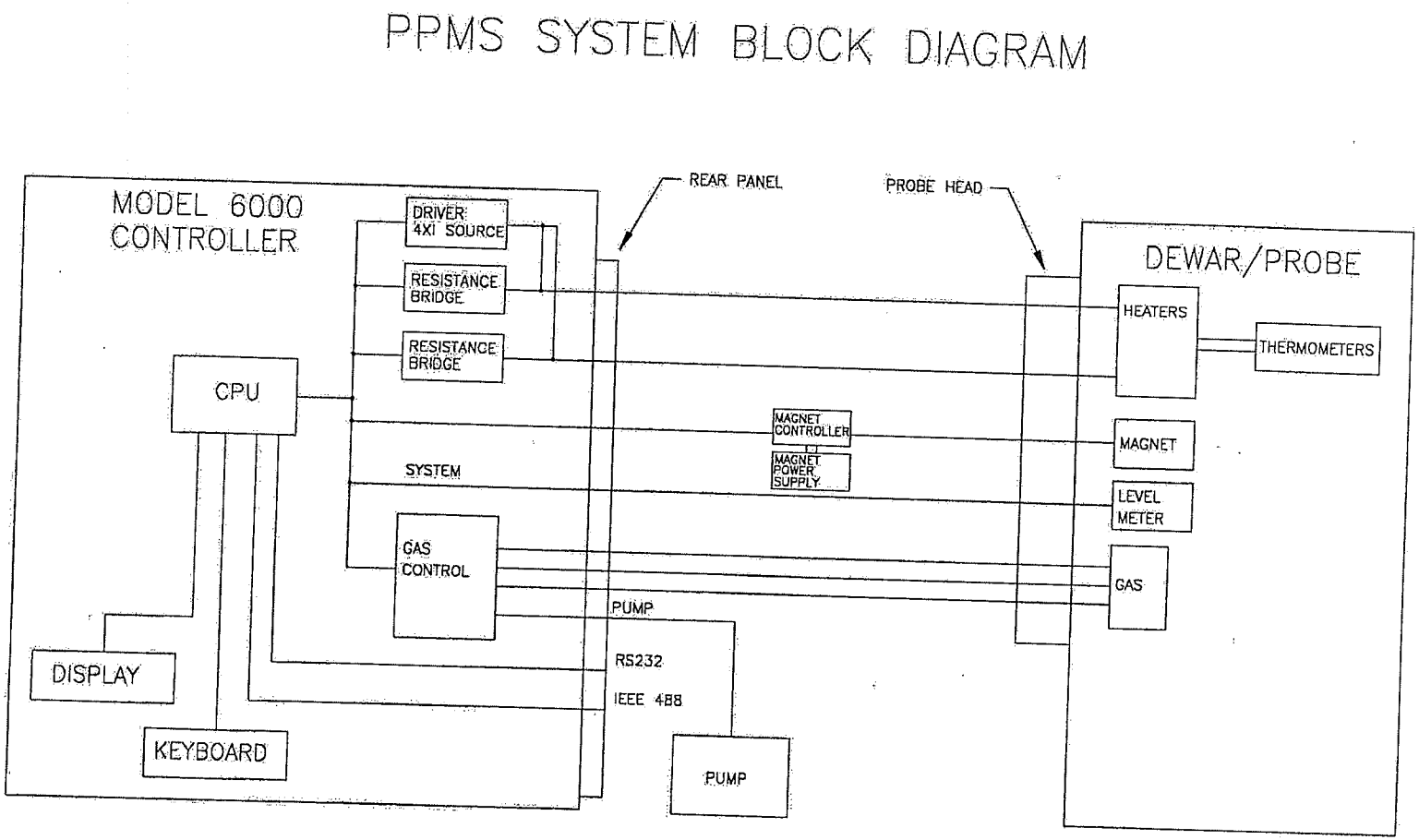

Figure 3.2 The PPMS system block diagram [40].

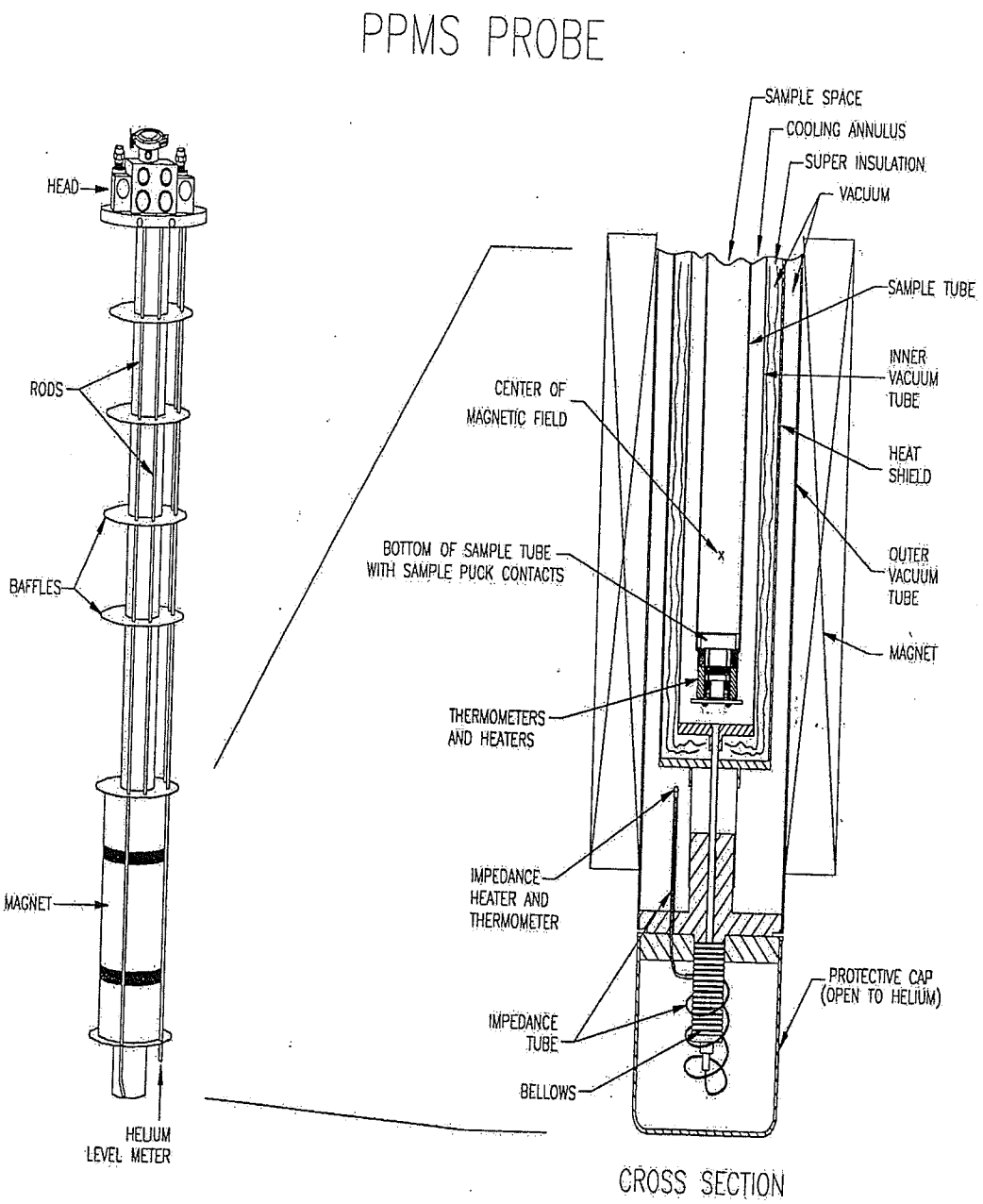

Figure 3.2 the PPMS measurement probe and the enlarged cross section [40]

addition to these major components, there is a superconducting magnet, baffle rods, a helium level meter, a protective cap and the probe head.

One of the most important functions of the PPMS probe is to control the temperature. The cooling annulus is the active region to control the temperature. For temperature above and below 4.2 K, there are two operational modes for the PPMS probe for temperature control. Above 4.2K, upon cooling, the helium vapour is drawn into the cooling annulus through the impedance tube by the vacuum pump to cool the outside of the sample tube. When warming, a block heater, which is mounted on the base of the sample tube, heats the sample to the desired temperature. The heater warms the vapour in the cooling annulus simultaneously; thus the entire sample tube is warmed more uniformly. Temperatures below 4.2 K are achieved by filling the cooling annulus with a controlled amount of liquid helium and manipulating the helium's boiling point. In other words, temperature control below 4.2 K is obtained through a flow control valve connected to the vacuum pump. For cooling, the valve is opened to decrease the pressure above the liquid helium, subsequently decreasing the helium's boiling point. Temperatures down to 1.8 K can be achieved this way. Warming is achieved by closing the valve slightly, allowing the pressure in the cooling annulus to increase, thus raising the helium's boiling point.

3.3 The AC Measurement System (ACMS) of the PPMS

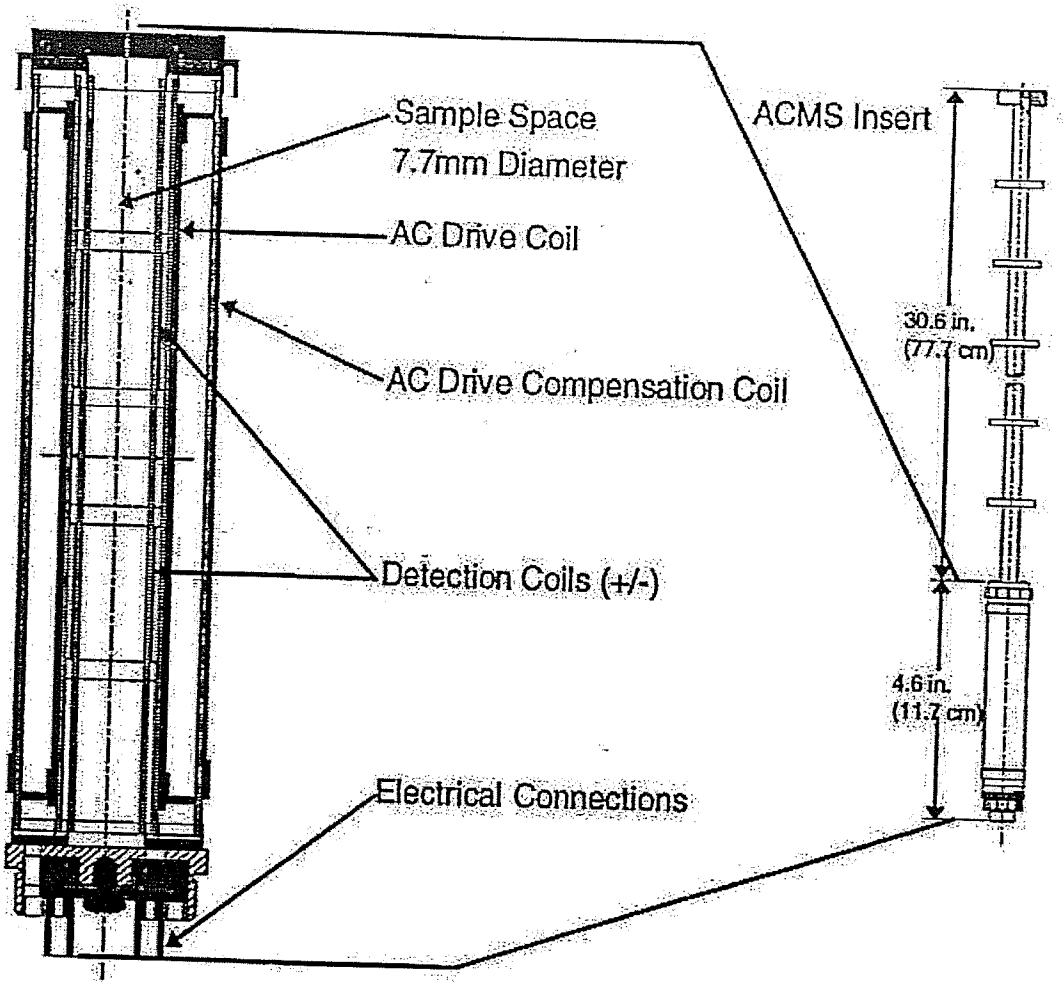

Figure 3.3 The diagram of the ACMS insert and coil set [40].

The ACMS system provides a capability to perform both AC susceptibility and (extraction) DC magnetization measurement without changing the hardware configuration. Sensitivity is quoted as 10^{-8} emu for AC susceptibility and 2.5 x 10^{-5} emu for DC magnetization. AC driving field amplitudes available range between 2

mOe and10Oe rms and AC frequencies range between 10 Hz and 10 KHz. Figure 3.2 shows the core elements of the ACMS system - the ACMS insert and an enlarged view of the coil section.

The ACMS insert houses the system's drive and pickup coils, the compensation coil, the "user" thermometer and associated electrical connections. Specifically, the AC drive coil provides an alternating driving field and the pickup coils detect the response from both sample moment and excitation field. A compensation coil is located outside the AC drive coil. The drive coil and compensation coil are counterwound and connected in series so that they receive the same excitation signals. A special feature of the Quantum Design PPMS 6000 system is that the pickup coil contains a low-inductance calibration coil which increases the accuracy of the phase and amplitude measurement. In addition to the alternating fields supplied by the ACMS drive coil, the host PPMS superconducting magnet can generate DC magnetic fields up to 90 kOe (9 T) during both DC and AC measurement processes. The following subsections describe, in detail, the principles of the DC magnetization and AC susceptibility measurement in the PPMS model 6000 system.

3.4 DC Magnetization Measurements

Magnetic materials show the same characteristics as the magnetic moment associated with a current loop. Letting dm be the magnetic moment associated with volume dV in a bulk sample, the magnetization per unit volume can be defined as

$$M = \frac{dm}{dV} \tag{3.1}$$

In practice, in addition to the volume magnetization, the mass magnetization and the molar magnetization has been used under different circumstances. DC magnetic measurements determine the equilibrium value of the magnetization in a sample. The sample is magnetized by an applied magnetic field and the induced magnetic moment is measured, producing a magnetization curve M(H). In the PPMS model 6000 system, during a DC measurement, a static field is applied to the measurement region and the sample is moved quickly between two sets of detection coils inducing a signal following Faraday's law [41],

$$\varepsilon = -\frac{\partial \Phi_B}{\partial t} \tag{3.2}$$

where ε is induced voltage and Φ_B is magnetic flux. This type of measurement is referred to as the extraction method. The signal in the detection coil depends on both the extraction speed and the sample's magnetic moment. The DC servo motor in the PPMS 6000 system can provide an extraction speed up to approximately 100 cm/sec, which dramatically increases the signal and decreases the contribution due to the time-dependent errors. The high extraction speed makes many scans possible in a

short period of time, and the averaging of these scans for each measurement point can reduce the random error; usually, 5 scans for each measurement was typically employed in the present work.

3.5 AC Magnetization Measurements

Since the magnetic moment characterizing the bulk materials can often be time dependent, AC measurements are quite important. AC measurements can provide some information about magnetic dynamics in ways which are not possible with a DC measurement (for example, frequency effect). In AC magnetic measurements, a small AC driving magnetic field is superimposed on the DC field, causing a time dependent moment to induce a current in the pickup coils, thus allowing measurements without sample motion. The detection circuitry is configured to detect in only a narrow frequency band, normally at the fundamental driving frequency.

For low frequency measurements, AC magnetometry is quite similar to a DC measurement. The magnetic moment of the sample follows the M(H) curves that are measured in the DC measurement. The susceptibility is the slope of such M(H) curves.

$$\chi = \frac{dM}{dH} \tag{3.3}$$

Susceptibility measurements play an important role in the current work. As different parts of the magnetization curves have different slope, a series of susceptibility values can be obtained. One of the advantages of the AC measurement is that it is very sensitive to the small changes of the moment. Since the AC measurement is sensitive to the slope of the M(H) curve and not the absolute value of the moment, small magnetic moment changes can be detected even when the absolute moment is large. This is favorable for the present study where the temperature dependence of the susceptibility is measured in different static biasing fields.

In a high frequency measurement, because of dynamic effects, the AC moment of the sample does not follow the curves of the DC measured M(H). The change of the magnetization frequently lags the driving field. Typically, an AC measurement gives us two components: the magnitude of the susceptibility, χ , and the phase shift, φ. Alternatively, one can think of the susceptibility as having an in phase component, χ', and out of phase part (imaginary part), χ''. These quantities are related by the following:

$$\begin{aligned} \chi' &= \chi\cos(\varphi) \\ \chi'' &= \chi\sin(\varphi) \end{aligned} \qquad (3.4) \qquad \text{and} \qquad \begin{aligned} x &= \sqrt{\chi'^2 + \chi''^2} \\ \varphi &= \arctan(\chi''/\chi') \end{aligned} \qquad (3.5)$$

The imaginary component, χ'', usually indicates that dissipative processes are present in the sample. In conductive samples, the dissipation can be produced by eddy currents. Relaxation and irreversibility are most prevalent in spin glasses and give

rise to a non-zero imaginary susceptibility χ''. In ferromagnets, a nonzero χ'' can indicate irreversible domain wall movement or absorption due to a permanent moment. In particular, both the real and imaginary parts of the susceptibility are very sensitive to the presence of a thermodynamic phase transition; such measurements are thus a basic tool for this research. Additionally, in the quantum design PPMS 6000 system, numerous useful parameters can be recorded in a single measurement. Besides the real χ' and imaginary part χ'' of the susceptibility and the phase angle φ, other important quantities are recorded including averaging time, temperature, DC magnetic field, frequency, amplitude of the driving field etc, enabling a comprehensive analysis to be performed.

3.6 Demagnetization Corrections

The demagnetization correction is important for a sample with a finite dimension. If a magnetic body is magnetized, free magnetic poles are induced at the both ends of the sample. These need to be taken into account as they introduce a demagnetizing field H_d, which is proportional to the magnetization M, often opposing it. The internal magnetic field is given by

$$H_i = H_a - NM \tag{3.6}$$

where H_a is applied field and N is demagnetizing factor. If the measured susceptibility is defined as $\chi_m = dM/dH_a$, the true susceptibility is given by $\chi_t = dM/dH_i$ and these two quantities are related by:

$$\chi_t = \frac{\chi_m}{1 - N\chi_m} \tag{3.7}$$

The measured susceptibility is thus not an intrinsic property of sample itself, but reflects the sample geometry. The demagnetizing correction is especially necessary in low field measurement.

In principle, the demagnetizing factor can only be calculated for ellipsoidally shaped samples in which the demagnetizing field is uniform. For any other non-ellipsoid body, the calculation is only an approximation and gives an average internal field over the whole sample volume. Practically, in order to eliminate the demagnetizing field and appraise the intrinsic properties of magnetic materials, the demagnetizing factor is often measured experimentally, as follows:

From equation (3.7), the measured (external) susceptibility can be expressed as:

$$\chi_m = \frac{1}{\frac{1}{\chi_t} + N} \tag{3.8}$$

Thus, if the sample have an infinite true susceptibility χ_t (as is predicted to occur in zero field at a ferromagnetic phase transition), the measured susceptibility is equal to $1/N$, i.e. the reciprocal of the demagnetizing factor. Experimentally, magnetization

curves were measured in low fields around the transition temperature, T_c, and from the limiting slope of these curves, the so called shearing curve, the demagnetizing factor N can be estimated.

Chapter 4

Magnetic Phase Transitions in Several Systems Displaying CMR Effects

4.1 The Colossal Magnetoresistance (CMR) Effects - A brief Introduction

Magnetoresistance is the resistance change (positive or negative) when a material is subjected to an external magnetic field. This effect was first discovered in 1857 by William Thomson. In normal metals, the magnetoresistance (MR) defined as

$$MR = \frac{\rho(H=0) - \rho(H \neq 0)}{\rho(H=0)} \times 100\% \qquad (4.1)$$

never exceeds 5% and therefore has few applications. In 1969, a very large magnetoresistance was reported in doped manganese oxide perovskites and this effect was named colossal magnetoresistance (CMR) after its rediscovery, analogous to the GMR effect found later in magnetic superlattices [42]. The magnetoresistance in CMR systems can be as large as 99.999...%. Figure 4.1 is a schematic sketch of the CMR effect. With an applied field, the peak resistivity decreases tremendously in amplitude and moves towards higher temperature. Thus, the magnetoresistance in

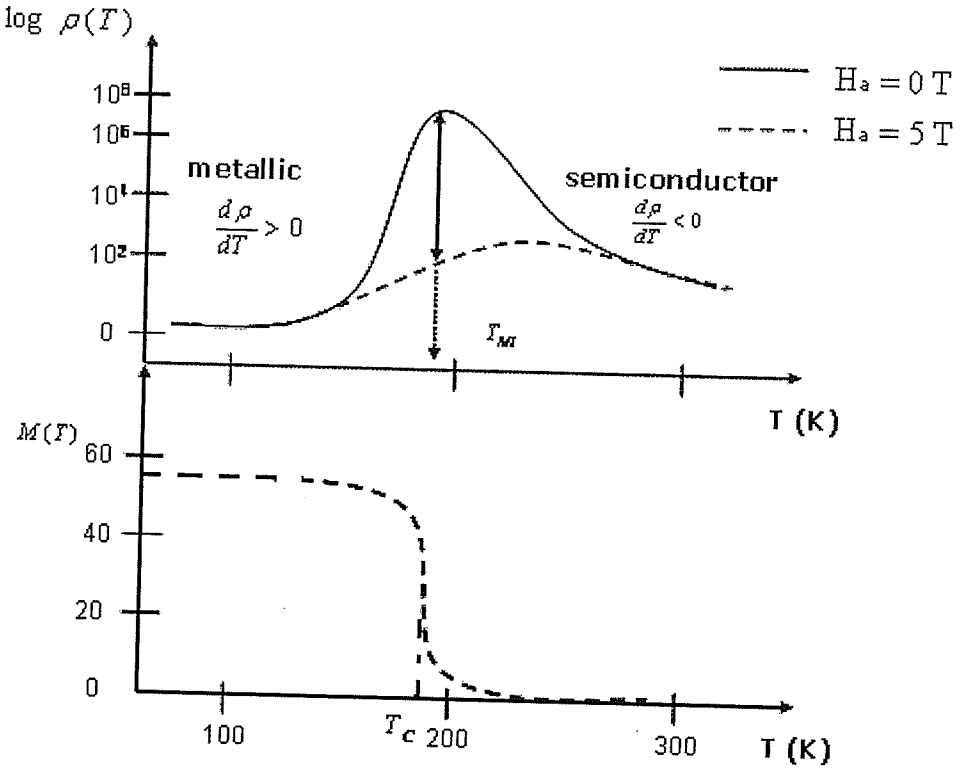

Figure 4.1 Schematic sketches of resistivity vs. temperature and the corresponding magnetization vs. temperature curve for a CMR material. With an applied field, the peak resistivity decreases in amplitude and moves toward higher temperature.

CMR systems is negative (instead of positive as in normal metals where it arises from the Lorentz force). Below the transition temperature, the temperature dependence of the resistivity has a metallic character, i.e. a positive resistivity temperature coefficient (RTC), $d\rho/dT > 0$. However, above the transition temperature it shows semiconductor-like behaviour with a negative RTC, $d\rho/dT < 0$. Accompanying this resistive transition from metallic to semiconductor character,

there is a magnetic phase transition from a ferromagnetic to a paramagnetic state, characterized by a Curie temperature, T_c.

There are many systems showing CMR effects; these include doped manganites, manganese oxide pyrochlores [43], europium hexaborides [44] and double perovskites [45]. Among these, the mixed-valence manganites have been the focus of the majority of studies because they present some unusual physical properties, which dramatically differ from other systems. For example, the manganites cover a wider range of transition temperatures typically 100 – 400 K; the carrier density in manganites is higher that in other systems; the ferromagnetic ordering in manganites is controlled by the carriers through a double exchange process whereas in other systems superexchange between localized ions dominates.

To summarize, since the (re)discovery of the CMR effect in manganites, it has been a subject of intense experimental and theoretical studies [2]. Experimentally, it has great potential for use in magnetic sensors or in magnetic recording heads, although the manganites usually possess a large residual resistivity which is not favorable for the latter. In terms of fundamental physics, understanding the behaviour of CMR systems has been identified as one of the most significant challenges facing the materials science community. These systems are regarded as important examples of strongly correlated electronic systems, offering a unique combination of coupling between charge, spin, orbital and phononic degrees of freedom.

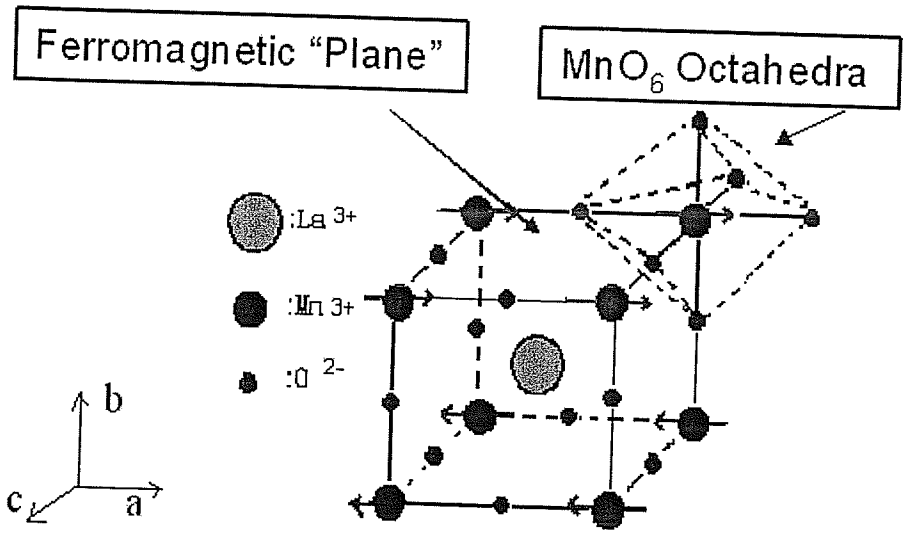

Figure 4.2 A schematic sketch of the perovskite manganite structure. LaMnO3 consists of a large Lanthanum ion at the center surrounded by manganese and oxygen ions. A manganese and six neighboring oxygen ions form a series of regular octahedra.

4.2 A basic description of doped manganites

Doped $LaMnO_3$, termed "manganites", has been studied for more than 40 years. These compounds have a general formula $A_{1-x}B_xMnO_3$, where A is a trivalent cation (e.g. La^{3+}, Pr^{3+}) and B is a divalent cation (typically an alkaline-earth Ca^{2+}, Sr^{2+} or Ba^{2+}). The parent compound $LaMnO_3$ was a major subject of early studies. X-ray diffraction work by Yakel [46] showed that $LaMnO_3$ has an orthorhombic structure with space group *Pnma*. Later, the ground state of $LaMnO_3$ was labeled as an A type antiferromagnet by Wollan et al. [47]. A sketch of this structure is shown in the

Figure 4.2. It consists of a (larger) lanthanum ion situated in the center of a cubic structure, surrounded by manganese and oxygen ions. At each corner, there is an oxygen octahedron with a Mn ion at its center. The magnetic moments in the a-c plane are ferromagnetically coupled and between two successive planes along the b axis, the magnetic moments are antiferromagnetically coupled. Here the magnetic moments interact via the superexchange interaction and the Mn-O-Mn bond angle is close to 180^0 [48], but the slight variation in the lattice constants result in superexchange interaction of differing sign. Jonker and Van Santen [7] showed that the only possible valence for oxygen in this system is O^{2-}, regardless of the composition, x, or the states of the other elements. Thus, the parent compound, $LaMnO_3$, contains only Mn^{3+} cations. However, any other composition, x, falling between 0 and 1, must introduce Mn^{4+} cations into system in order to maintain charge neutrality. Thus, with divalent doping, where a number of La^{3+} are substituted by divalent ions, the resulting compound has a formula $A^{3+}_{1-x}B^{2+}_{x}Mn^{3+}_{1-x}Mn^{4+}_{x}O^{2-}_{3}$ and the ratio of Mn^{3+}/Mn^{4+} is equal to the ratio of A^{3+}/B^{2+}. Because of the co-existence of both Mn^{3+} and Mn^{4+}, such systems are also known as mixed-valence manganites. The co-existence of two valence states strongly influences the electrical and magnetic properties of these systems. In terms of the structure, the doped lanthanum manganites possess a so-called perovskite structure which will be discussed in the next subsection; thus this system is also known as doped perovskite manganites.

In the mixed-valence manganites, the actual crystal structure is still basically cubic, as in the parent compound, but slightly distorted. The distortion arises from several sources. First, the mismatch of the ionic size on sites A and B. The size of the cations at site A and B can be very different and this causes the oxygen octahedra to both tilt and twist. This distortion can be measured by the so-called tolerance factor [7]

$$t = \frac{(r_B + r_O)}{\sqrt{2}(r_A + r_O)} \tag{4.2}$$

where r_A, r_B and r_O are the radii of the ions at the A site, the B site and of the oxygen ions, respectively. In the ideal cubic structure, the tolerance factor is unity. Detailed studies on several A site (La, Pr, Nd) and B site (Ca, Sr, Ba, Pb) substituted manganites showed that a stable perovskite structure can be retained for $0.85<t<0.91$[2]. Another source of distortion is the size difference between Mn^{3+} and Mn^{4+} ions. According to the ionic radii provided by Shannon [49], the radius of Mn^{3+} (0.645 Å) is 18% larger than Mn^{4+} (0.530 Å), which leads to a distribution of larger and smaller octahedra. Moreover, the Jahn-Teller effect will deform the oxygen octahedra further and this results in a removal of the degenerate e_g states as detailed in the following subsection. As a result of the distortion, the Mn-O-Mn bond angle, which is 180^0 in the ideal perovskite structure, can vary between 150^0-180^0 for different compositions. The bond angle, θ, together with bandwidth, are closely related to the magnetic and transport properties of the manganites; the Curie

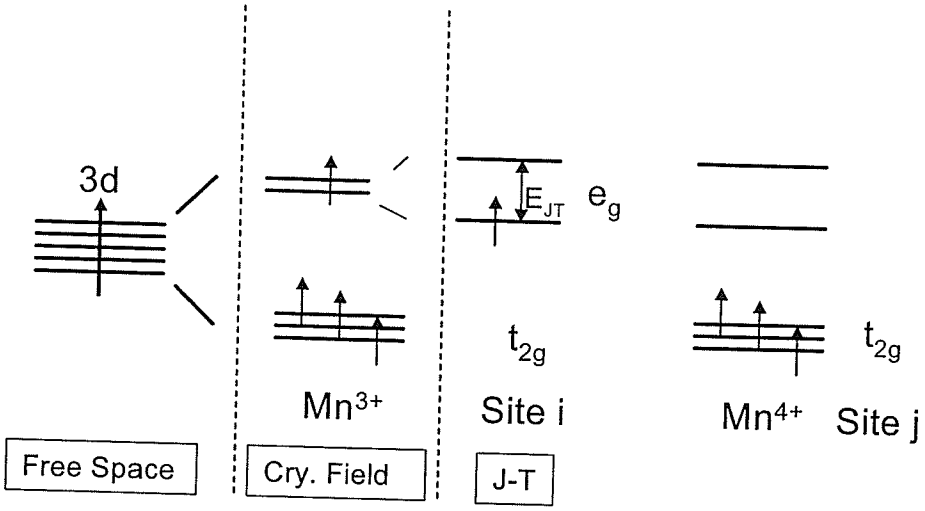

Figure 4.3 In the presence of a crystal field, the five Mn 3d orbitals in the free space will split into doubly degenerate e_g states and triply degenerate t_{2g} orbital states. The Jahn-Teller effect will further split the e_g state and will lift the e_g state by 0.25 eV.

temperature T_c increase with a decrease of the bond angle and the residual resistivity decreases by an order of magnitude when the bond angle decreases over the range mentioned earlier.

4.3 Electronic Properties of Manganites and Double Exchange

In the mixed-valence manganites, the oxygen atoms are believed to have a full outer shell (2p), being in an O^{2-} state, and the Mn ions have an incomplete d shell. The ground state electronic configuration for the Mn^{3+} and Mn^{4+} is $3d^4$ and $3d^3$ respectively. According to Hund's rules, in order to maximize the total spin

(minimize the energy), all unpaired electrons in the d-shell must have their spins parallel to one another, as figure 4.3 shows (only the majority spin states are shown, the minority spin states are much higher in energy). The five d orbitals, which are five-fold degenerate in an isolated atom, will be split into a three-fold degenerate t_{2g} level and a two-fold degenerate e_g level by the presence of a cubic crystal field. The t_{2g} level has a lower energy than the e_g level, by about 1.5 ev [50]; equivalently, the t_{2g} electrons can be considered as localized carriers with the total spin of the t_{2g} level (S=3/2) usually referred to as the core spin. Specifically, for Mn^{4+} ions with 3 electrons in a d shell, according to Hund's rules, these electrons will occupy the lower energy t_{2g} level and leave the e_g level empty. Mn^{3+} possesses an extra electron, which will occupy the e_g level, giving a total spin of S=2. Theoretically, the saturation magnetization at zero temperature can be evaluated, based on a spin-only assumption, as

$$M_S = (1-x)\times Mn^{3+}(S=2) + x\times Mn^{4+}(S=\frac{3}{2}) = 4(1-x)\mu_B + 3x\mu_B = (4-x)\mu_B$$

where μ_B is the Bohr magneton. This offers an effective way to estimate the sample's composition experimentally. Another effect that has to be taken into account is the Jahn-Teller distortion. The Jahn-Teller Theorem, published in 1937, states [51]: "any non-linear molecular system in a degenerate electronic state will be unstable and will undergo distortion to form a system of lower symmetry and lower energy thereby removing the degeneracy". The Mn^{3+} ion is known to be an ion with a

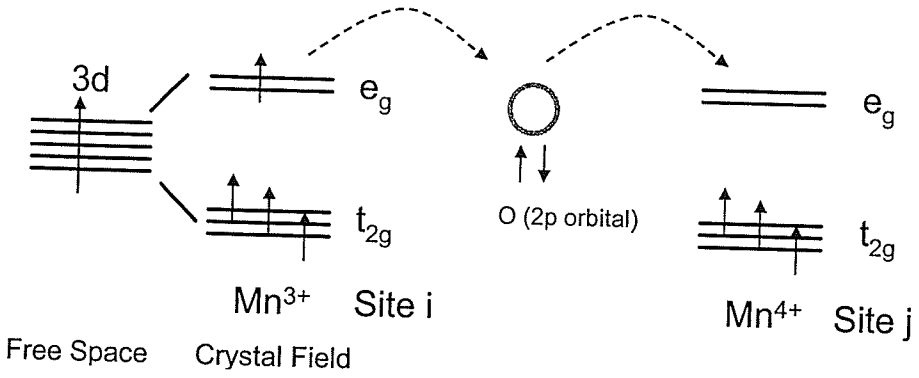

Figure 4.4 According to Hund's rule, the spin (S=1/2) of the e_g electron should be parallel to the "core spin" (S=3/2) of the three t_{2g} electrons in order to maximize the total spin. The e_g electron on a Mn^{3+} site hops to a 2p electronic state on O^{2-} site; ***simultaneously,*** *a 2p electron on the O^{2-} site hops to an empty e_g state on the Mn^{4+} site*

strong Jahn-Teller effect when it occupies an octahedral site, as in the manganites. Thus, the e_g level in the Mn^{3+} ions will be further split as figure 4.3 shows. The energy between the two e_g levels is about 0.25 eV.

After Jonker and Van Santen [7] identified the strong relationship between ferromagnetism and metallic conductivity in mixed-valence manganites, Zener proposed the so-called double exchange model to explain this behaviour [5]. He introduced two configurations: Mn^{3+}-O^{2-}-Mn^{4+} and Mn^{4+}-O^{2-}-Mn^{3+} and suggested that the exchange interaction between Mn^{3+} and Mn^{4+} ions occurs via an oxygen ion; specifically, the transfer of an electron from the Mn^{3+} to the oxygen and simultaneously from the oxygen to the neighboring Mn^{4+} ion (see Figure 4.4). This

process is fundamentally different from the conventional superexchange interaction, which dominates the antiferromagnetic parent compound. Because of the strong Hund's rule coupling, the core spins of neighbouring Mn ions must align ferromagnetically if hopping is to occur in the metallic state. Thus, double exchange is always ferromagnetic. If the Mn core spins are not parallel to one another, the electron mobility decreases and transfer becomes more difficult. Further studies of double exchange by Anderson and Hasegawa [6] found that the transfer integral for double exchange is proportional to $\cos(\theta/2)$ instead of $\cos(\theta)$ as in the superexchange case, where θ is the angle between two adjacent core spins. Clearly, electrons hopping maximises when the corresponding core spins are parallel ($\theta = 0$) and vanish when they are antiparallel ($\theta = 180^0$). The application of an applied magnetic field depresses the spin disorder and aligns core spins, leading to a lower resistivity. The double exchange model successfully explains qualitatively the co-occurrence of ferromagnetic and metallic states in the mixed-valence manganites; however, it fails to explain the high and low temperature transport and magnetic behaviour quantitatively.

4. 4 Magnetic Polarons and Transport Behaviour in Manganites

As far as the transport properties are concerned, there are essentially two kinds in the mixed-valence manganites: those which undergo a transition from metallic to

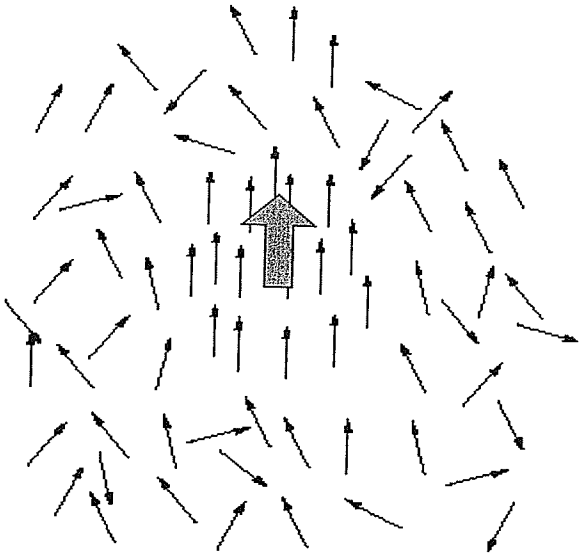

Figure 4.5 An ordered ferromagnetic cluster acts as a magnetic potential well where the carriers can get trapped.

semiconductor-like behaviour and those which retain their metallic / semiconductor characters regardless of the composition and magnetic state (i.e. the $La_{1-x}Pb_xMnO_3$ system [52] and $La_{0.8}Mg_{0.2}MnO_3$ [53]). The high temperature transport behaviour in the manganites can be understood quantitatively in terms of polaron formation. Magnetic polarons are formed from a localized carrier coupled to a lattice deformation. Two types of magnetic polarons have been introduced: the free and bound polarons. The free magnetic polaron is a ferromagnetic cluster embedded in a paramagnetic background, namely, a region of order in a disordered matrix of localized core spins. This local order will act as a potential well and trap the carrier

as shown in Figure 4.5. In the case of a bound magnetic polaron, the force which traps the carrier is the Coulomb interaction between the carrier and the surrounding impurity ions. Polarons in manganites have been widely reported, especially in the high-temperature regime, where the magnetic correlations become negligible compared with charge/lattice and charge/charge interactions. The polaronic transport in manganites can be simply expressed as:

$$\rho(T) = \rho_0 T^n \exp(E_a / K_B T) \tag{4.3}$$

Here E_a is the activation energy which is, namely, the energy required for an electron to delocalize from the potential well. There are two physical limits for this hopping process which depend on the magnitude of the associated phonon frequency. If lattice distortions are slow compared to the charge carrier hopping frequencies, the hopping is adiabatic; otherwise it is non-adiabatic. In the adiabatic limit, $n = 1$, and the resistivity is:

$$\rho(T) = \rho_0 T \exp(E_a / K_B T) \tag{4.4}$$

Some doped manganites in the high temperature regime obey this relation very well [54, 55]. In the non-adiabatic limit, $n = 3/2$, and corresponding resistivity is

$$\rho(T) = \rho_0 T^{3/2} \exp(E_a / K_B T) \tag{4.5}$$

Transport in the non-adiabatic limit is accomplished by electron transfer between polarons rather than by the field-induced movement of the polaronic entities themselves. The transport behaviour in $La_{1-x}Mg_xMnO_3$ ($x<0.4$) is consistent with the

predictions for carrier transport by small polarons* hopping in both the paramagnetic and ferromagnetic phases [56]. $La_{0.67}Ca_{0.33}MnO_3$ thin films also show a non-adiabatic small polaron behaviour in zero field [57]. Besides these two kinds of hopping processes, thin films or polycrystalline samples with small grains exhibit a variable-range-hopping (VRH) behaviour, which is described by

$$\rho(T) = \rho_0 \exp(T_o/T)^{\frac{1}{4}} \tag{4.6}$$

Here ρ_0 is a prefactor and T_0 is a characteristic temperature. The high temperature transport in $(La_{1-x}Nd_x)_{0.67}Pb_{0.33}MnO_3$ samples shows a VRH behaviour in a wide composition range ($0.2 \le x \le 1.0$) (details will be given in chapter 4); similar results can be found in the work of Coey et al [50].

The low temperature transport properties of manganites have been studied in detail only recently; it turns out to be much more complicated than that of normal metals. In non-magnetic metals, the electrical resistivity is often assumed to follow Matthiessen's rule

$$\rho(T) = \rho_0 + \rho_1 T^p \tag{4.7}$$

where the first term, ρ_0, is the residual resistivity arising from scattering by impurities and defects and the second term is the intrinsic contribution from lattice (phonon) scattering of charge carriers, which usually has a dependence with $p = 5$ in normal metals. In low temperature manganites, spin waves are also expected to play

* If the carrier, together with its associated crystalline distortion, is comparable in size to the cell parameter, the object is called a small polaron.

an important role, so the contribution of magnons must be taken into account. Studies [12] in $La_{1-x}Ca_xMnO_3$ (x=0.2, 0.33, 0.45) samples have suggested that the low temperature resistance data can be fitted to equation (4.7) with $p = 2.5$. If an additional T^2 term, for electron-electron scattering, is added, the data can be fitted to equation (4.7) with $p = 4.5$ which is the prediction for electron-magnon scattering in a double-exchange system [58]. A T^5 dependence will arise if electron-phonon scattering dominates. Akimotot et al. [59] also claim that the low temperature resistivity behaviour is closely related to the conduction electron bandwidth of the sample. Some comparisons [11] between polycrystalline and single crystal samples suggest that the scattering from grain boundaries also plays a significant role in the low temperature transport behaviour. Although good fits to various powers of the temperature, T , (T^5, $T^{4.5}$....) have been found, the underlying transport mechanism is still elusive.

In summary, both the low and high temperature properties (magnetic and transport) in manganites have been studied intensely. This thesis will focus mainly on the rarely studied temperature regime – the critical region. In the following sections of this chapter, critical analysis of single crystal $La_{0.73}Ba_{0.27}MnO_3$ and $La_{0.73}Ca_{0.27}MnO_3$ samples will be presented. Subsequently, the critical behaviour of a series of polycrystalline $(La_{1-x}Nd_x)_{0.67}Pb_{0.33}MnO_3$ ($0.2 \leq x \leq 1.0$) samples will be

analyzed together with high temperature transport behaviour, the latter showing a variable range type hopping dependence.

4.5 Critical Analysis of Single Crystal $La_{0.73}Ba_{0.27}MnO_3$

4.5.1 General Review

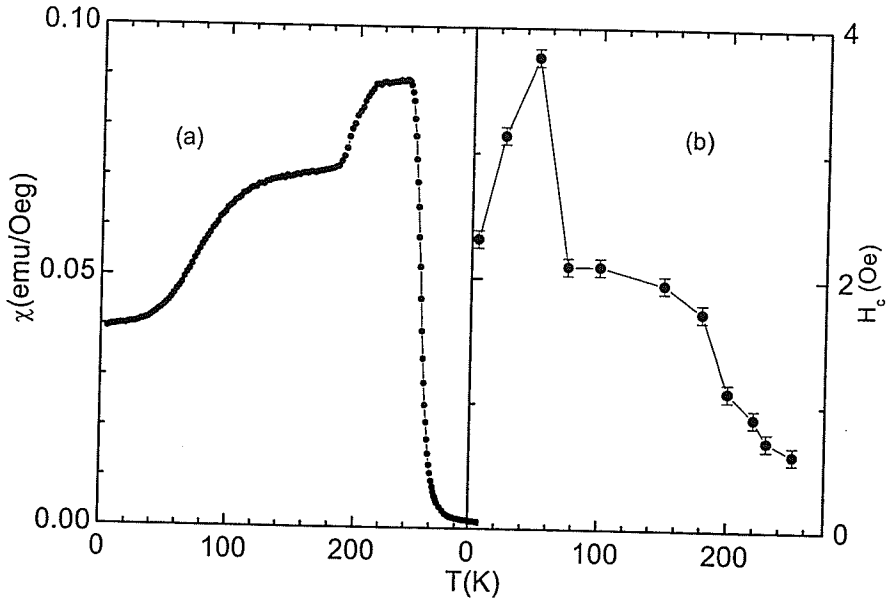

Figure 4.6(a) The zero-field ac susceptibility curve for $La_{0.73}Ba_{0.27}MnO_3$ measured on warming; (b) the coercive field H_c measured from the complete hysteresis loops as a function of temperature.

Figure 4.6(a) presents the zero-field susceptibility $\chi(0,T)$ as a function of temperature between liquid Helium temperature (4.2 K) and 300 K measured on warming following zero field cooling at 300 Hz in a 0.1 Oe rms driving field. The shape of this curve shows a complex structure; obviously, the marked susceptibility

drop above 250 K suggests a transition from a ferromagnetic state to a paramagnetic state. By finding the temperature corresponding to the minimum slope $d\chi/dT$, a preliminary ordering / Curie temperature $T_C \approx 248$ K can be estimated. The relatively flat plateau between 212 K and 240 K corresponds to a measured susceptibility of $\chi = 0.089$ emu/g Oe, which, if identified with a (lower) demagnetization limit N^{-1}, yields a demagnetization factor $N = 1/\chi = 11.2(4)$ g Oe /emu. This result is confirmed by theoretical calculation [60]; treating this specimen as an ellipsoid and evaluating the corresponding elliptic integral, a demagnetization factor $N = 9.94$ g Oe /emu is obtained (based on a theoretical density of 6.76 g /cm^3). The susceptibility drop around 200 K in figure 4.6(a) has been attributed to a structural change from a higher temperature, higher moment rhombohedral (R) $R\bar{3}c$ phase to a lower temperature Orthorhombic (O) *Pbnm/Imma* counterpart. The decrease below 100 K in figure 4.6(a), often linked to an increasing coercive field, likely arises from a different source here, as discussed below. Features emerging below 50 K in figure 4.6(a) will also be discussed in the next subsection. However, the focus of the present subsection is to investigate the nature of the phase transition around the magnetic ordering temperature, i.e. the secondary peak structure appearing around 250 K in figure 4.6(a).

Figure 4.7(a) shows a selection of magnetization isotherms measured in the vicinity of the ordering temperature, T_c. The magnetization isotherms around T_c

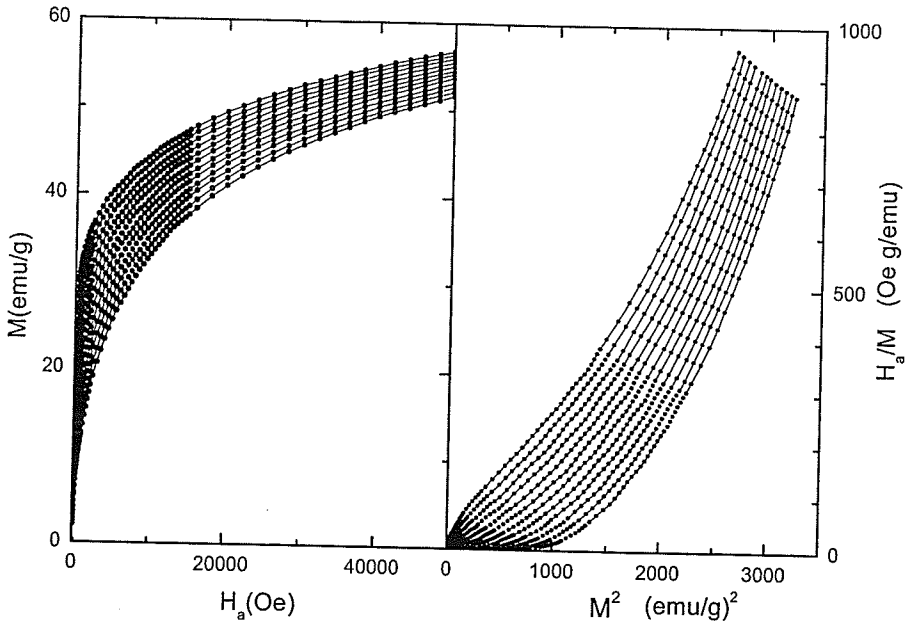

Figure 4.7 (a) Magnetization isotherms between 240 K(top) and 251 K (bottom) in 1 K step. (b) The same data in (a) replotted in H/M versus M^2 format

display no "S" shaped characteristics in fields up to 50 kOe. As discussed previously, the "S" shaped behaviour of magnetization isotherms is usually related to a first-order phase transition, where the metamagnetic field, H_M, derived from such curves delineates the boundary separating a ferromagnetic state from a paramagnetic state. Thus, the magnetization isotherms reproduced here suggest the transition around 250 K is a second-order/continuous one; this assertion is confirmed in figure 4.7(b) by replotting the corresponding magnetization isotherms in a M^2 versus H/M format (Arrott plots). Arrott plots for this specimen show no indication whatsoever of a

negative slope, neither initially (corresponding to the coefficient $\alpha_4(T)$ in the Landau expansion) nor at higher magnetization. The clear curvature apparent in figure 4.7(b) also indicates that the conventional Arrott plot cannot apply to this sample, namely, mean field critical exponents ($\gamma = 1$, $\beta = 0.5$, $\delta = 3$) cannot describe the critical behaviour of the present sample. A carefully examination of the very low field magnetization isotherms in figure 4.7(a) also reveal the technical/magnetic soft character of this specimen, the rapid increasing of magnetization near H_a=0 likely arises from the motion of domain walls. The soft characteristics are also suggested by the appearance of the flat plateau in the zero-field susceptibility curve, i.e. low ac driving fields (0.1Oe here) drive soft magnetic materials to the demagnetization limit. The temperature dependence of the coercive field also confirms such soft features, as figure 4.6(b) shows. These coercive fields do not exceed 5 Oe at any temperature between 5 K and 250 K; above 250 K, the sample is paramagnetic. From the low field isotherms measured around the ordering temperature, where they approach a shearing curve limited behaviour, a demagnetization factor N = 10.62 g Oe/ emu can be deduced by using data over an applied field range -50 Oe $\leq H_a \leq$ 50 Oe. The three demagnetization factors deduced above agree with each other within 5%. In the following discussion, an average demagnetization factor of N= 10.9(3) g Oe/emu from the two experimental values will be used. Indeed, due to the non-uniform sample shape, data involving demagnetizing fields (NM) above 50% of the applied

field H_a – essentially for H_a < 350 - 400 Oe - will be excluded in the following analysis, as indeed was done previously for single crystal $La_{0.75}Sr_{0.25}MnO_3$ [61].

4.5.2 Critical behaviour in low and medium fields

Previous studies in doped manganites suggest the magnitude of the magnetoresistance around T_c is inversely proportional to the ordering temperature T_c and is also closely linked to the order of the ferromagnetic to paramagnetic phase transition [2]. For example, $La_{1-x}Sr_xMnO_3$ ($0.2 \leq x \leq 0.5$) possess some of highest T_c values and a weak magnetoresistance accompanying a second-order phase transition; by contrast, $Pr_{1-x}Ca_xMnO_3$ ($0.1 \leq x \leq 0.3$) exhibits an enhanced magnetoresistance at a significantly lower T_c, accompanying a first-order phase transition [62]. In the Ba doped system, available transport data [63, 64] shows a moderate magnetoresistance (40-50%) with a relatively higher T_c (for example, 245 K in the present sample). Following the trend mentioned above, a continuous/ second-order phase transition is expected in the present sample. The following discussion, based on the magnetization isotherms, will reveal a continuous phase transition with 3D Heisenberg exponents.

As discussed in Chapter 2, from the equation of state (2.14), the asymptotic behaviour of the scaling function for the larger and smaller values of its argument will lead to the power-law relationships, namely, equation (2.15) – (2.19). From these

relationships, critical exponents, which are model-dependent, can be extracted in a self-consistent way from these power-law relationships. Obviously, all these power-laws should be evaluated based on the contribution arising from magnetic critical fluctuations alone; however, the measured magnetization isotherms contain contributions from both the singular magnetic response as well as technical components. In order to reveal the nature of the critical phase transitions, such technical contributions, as well as complication arising from the crystalline anisotropy, must be eliminated. This can be accomplished by using the Arrott-Noakes equation of state (equation 2.29) [38]. The spontaneous magnetization, M_S, and initial susceptibility, χ_i, can be obtained by extrapolating from the "high" field regime, viz, the technically saturated regime. Arrott plots in figure 4.7(b) are nothing but a special case of the above equation with mean field exponents ($\gamma = 1$, $\beta = 0.5$, $\delta = 3$); thus equation (2.29) is usually referred to as a Modified Arrott plot.

Figure 4.8 presents the modified Arrott plots for the present specimen. Exponents γ and β in this figure are chosen by trying different values between mean field theory ($\gamma = 1$, $\beta = 0.5$, $\delta = 3$) and 3D Heisenberg exponents ($\gamma = 1.387$, $\beta = 0.365$, $\delta = 4.8$) [23]; the former corresponds to long-range interactions and the latter to a system with short-range interactions. For the appropriate set of exponents, the isotherms shown in figure 4.7(b) are transformed into a series of parallel straights lines, as shown in figure 4.8. From such plots, the temperature dependence of the spontaneous magnetization, Ms(T), and initial susceptibility, $\chi_i(T)$, can be obtained from the

intercepts of these straight lines on the horizontal and vertical axes, respectively. The straight line extrapolating through the origin gives the critical temperature; in practice, this procedure usually involves the extrapolation of several curves near the ordering temperature to find the minimum absolute intercept and then interpolating. Using this technique, an improved estimate, $T_c = 245 \pm 0.5$ K, was found, as shown in figure 4.8. A detailed examination of the exponents used in figure 4.8 reveals values very close to the predictions of the 3D Heisenberg model. However, as discussed previously, the critical exponents γ and β can vary substantially without a significant change in the modified Arrott plots. Thus, the power-law relationships mentioned above should be tested for self-consistency using the spontaneous magnetization, M_S, and initial susceptibility, χ_i, obtained from modified Arrott plot intercepts. True self-consistency is achieved when the modified Arrott plots and the power-laws yield the same set of critical exponents. This is summarized in figures 4.9 to 4.11. Figure 4.9 shows the temperature dependence of the spontaneous magnetization (from the horizontal intercepts in figure 4.8); while the inset of this figure represents the same data plotted against the reduced temperature on a double logarithmic scale. A test of the power law prediction of equation (2.15) is provided by the least-square fit in the inset of figure 4.9, which yields an order parameter critical exponent

$$\beta = 0.364 \pm 0.003, \quad \text{for } 2\times 10^{-3} \leq |t| \leq 2 \times 10^{-2}$$

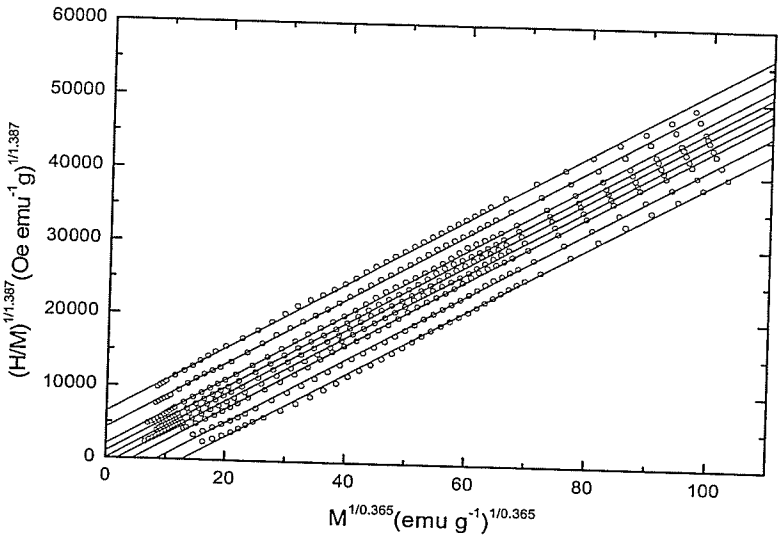

Figure 4.8 $M^{1/\beta}$ versus $(H/M)^{1/\gamma}$ (Modified Arrott plots) using Heisenberg model exponents (β = 0.365, γ = 1.387) for a selection of magnetization isotherms at temperatures of 242 (top), 243, 244, 244.5, 245, 245.5, 246, 247 and 248 K (bottom).

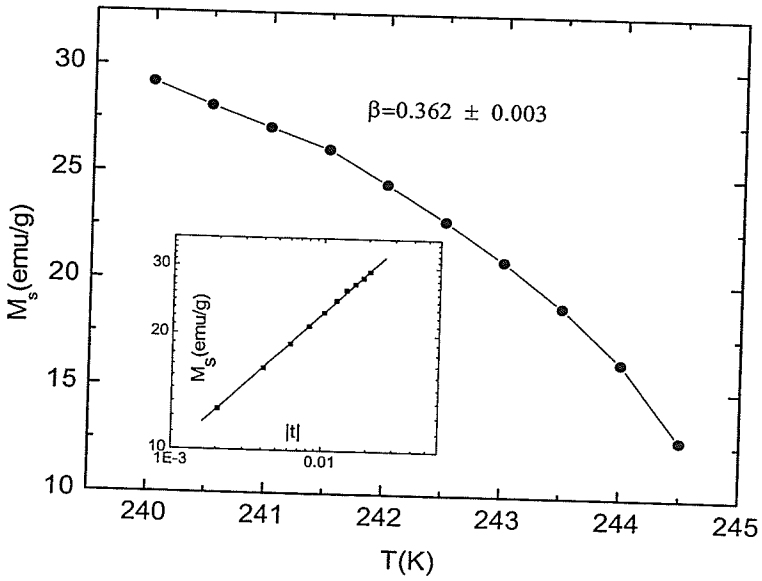

Figure 4.9 The spontaneous magnetization, M_S, plotted against temperature. The inset shows M_S versus reduced temperature plot on a double-logarithmic scale as a test of equation (2.15).

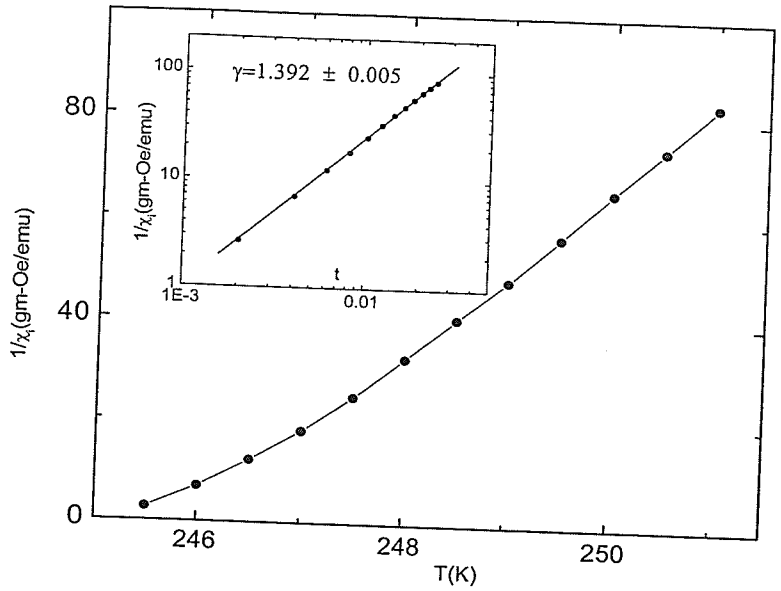

Figure 4.10 The reciprocal of the initial susceptibility, χ_i, plotted against temperature. The inset presents a $1/\chi_i$ versus reduced temperature plot on a double-logarithmic scale as a test of equation (2.17)

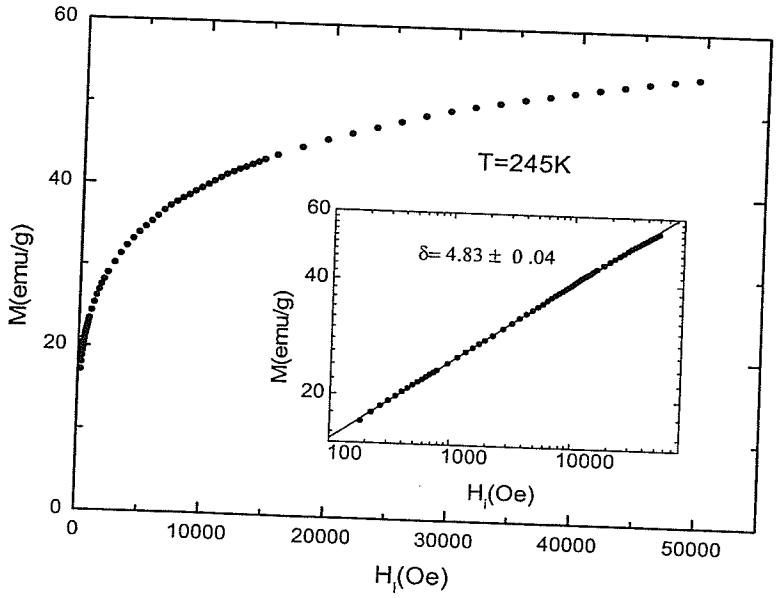

Figure 4.11 The critical isotherm – the zero intercept in figure 4.8. The inset shows the same data replotted in a log-log scale as a test of equation (2.19); the straight line yields the critical exponents δ.

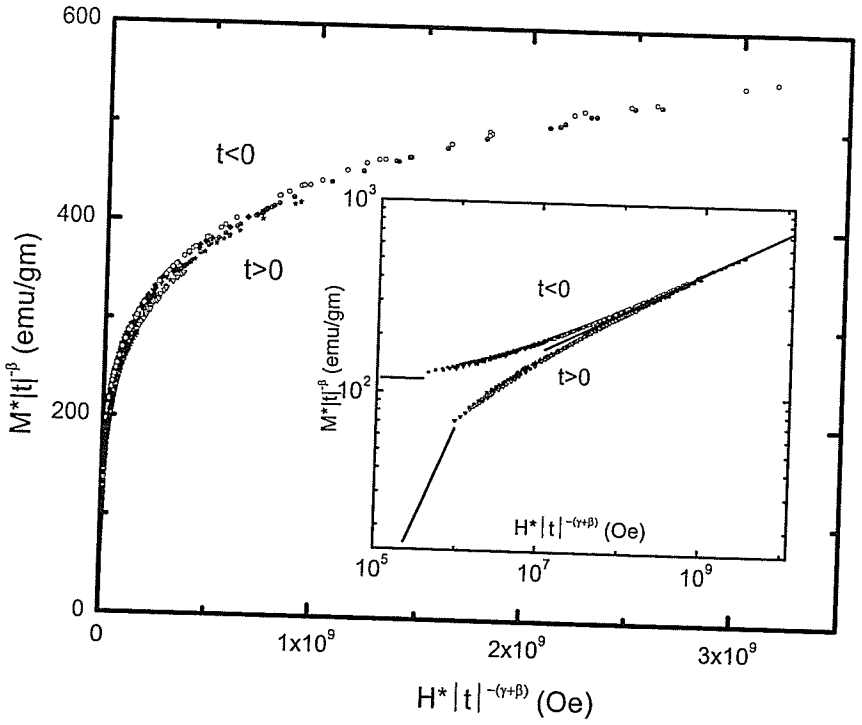

Figure 4.12 A scaling plot with the exponents and T_c value obtained from the previous three figures. The different symbols stand for different temperatures. While the linear plot in the main body of this figure shows evident differences at higher fields, the log-log scale of the inset emphasises differences in lower fields and also demonstrates the collapse of magnetization isotherms in the critical regime onto the two branches of the scaling function. The solid lines drawn in this inset represent the asymptotic forms of the scaling function discussed in the text.

Similarly, figure 4.10 shows the reciprocal of the initial susceptibility $1/\chi_i$, found by extrapolating the straight line to the vertical axis in figure 4.8, as a function of

temperature. The linear fit drawn in the inset of this plot yields the susceptibility exponent,γ, from equation (2.17) of

$\gamma = 1.392 \pm 0.005$, for $2\times 10^{-3} \leq t \leq 3 \times 10^{-2}$

Figure 4.11 shows the magnetization along the critical isotherm as a function of field; the inset in figure 4.11 reproduces these data replotted on a log-log scale, and the slope of this line yields the critical exponent

$\delta = 4.83 \pm 0.04$, 200 Oe $\leq H_i \leq$ 50 000 Oe

Overall, the critical exponents obtained from the above power-law relations agree very well with those predicted by the 3D Heisenberg model, as indeed do the exponents used to construct the modified Arrott plots in figure 4.8, as the self-consistency condition ensures. This can be further tested by the scaling plot - figure 4.12 Rearranging the state of equation (equation 2.14), the scaling function can be written as $F_{\pm}\left(h/|t|^{\gamma+\beta}\right) = m(h,t)/|t|^{\beta}$; thus, with the current value for the ordering temperature, T_c, and the critical exponents β and γ, all the magnetization isotherms around the critical region should collapse onto the two branches of the scaling function (F_+, $t>0$; F_-, $t<0$) when replotted in an $M/t^{-\beta}$ versus $H/t^{-(\gamma+\beta)}$ format. Figure 4.12 demonstrates complete scaling of all such magnetization data acquired in the temperature interval $242.0 \leq T \leq 247.5$ K and the field range $200 \leq H \leq 50{,}000$ Oe . Clearly, in light of the sign of the reduced temperature, t, all data fall onto two branches of the scaling function, (especially in high fields where demagnetization

effects become less important); the inset in this plot, being double logarithmic-scale in nature, emphasizes the differences in low field. While the functional form of the scaling functions $F_{\pm}$ is not known in general, the asymptotic behaviour at large and small values of the argument ($H/t^{-(\gamma+\beta)}$) can be deduced as follow:

$$F_{-}(0) = M_S(0) \quad (H \to 0, T < T_C) \tag{4.8}$$

$$F_{+}\left(\frac{h}{t^{\gamma+\beta}}\right) \sim \chi_0 \frac{h}{t^{\gamma+\beta}} \quad (H \to 0, T >> T_C) \tag{4.9}$$

$$F_{\pm}(\infty) \sim \left(\frac{1}{D}\frac{h}{t^{\gamma+\beta}}\right)^{1/\delta} \quad (t = 0, H > 0) \tag{4.10}$$

The solid lines drawn in the inset of figure 4.12 represent the asymptotic forms of the scaling function $F_{\pm}$ for the present specimen.

4.5.3 Critical amplitude analysis

In addition to checking the critical exponents (γ,β,δ) associated with a phase transition, another effective way to test the universality class of the transition is by estimating the critical amplitudes, the coefficients in equations (2.15), (2.17) and (2.19). The critical amplitudes $M_S(0)$, χ_0 and D for the present specimen were determined by fitting the corresponding power laws in the insets of figures 4.9-4.11; the values are summarized in upper panel of table 4.1. Both critical exponents and critical amplitudes show model dependence, more importantly, critical amplitudes

Critical Amplitude	Ms(0)	χ_0	D	
Value	120.8 ± 1.6	6.8 ± 0.2	$1.8 \pm 0.4 \times 10^{-4}$	
Reduced Critical Amplitude	Mean – Field S = 1/2: S = 1.87	fcc Heisenberg S=1/2 : S = ∞	fcc Ising S =1/2 : S=3/2	Experimental
$\frac{M_S(0)}{M_{sat}(0)}$	1.73:1.53	1.69: 1.22-1.44	1.49:1.31	1.40 ± 0.01
$\frac{\mu_{eff} H_0}{k_B T_c}$	1.73:2.99	1.58	1.52	$0.49 \pm 0.01 \mu_{eff}$
$\frac{D M_S(0)^{\delta}}{H_0}$	1.0	1.55:1.23-2.07	1.88	$1.2^{+0.26}_{-0.04}$

Table 4.1 Upper panel: critical amplitudes obtained by fitting corresponding power law relations; lower panel: reduced critical amplitudes in various models for a range of spin values, and the corresponding experimental values.

also depend on spin values. Usually, reduced critical amplitudes $M_S(0)/M_{Sat}(0)$, $\mu H_0/k_B T_C$, $DM_S(0)^{\delta}/H_0$ are used rather than the critical amplitudes themselves. In mean field theory, the spin dependence of the reduced critical amplitudes is well established [65]:

$$\frac{M_S(0)}{M_{sat}(0)} = \left\{ \frac{10(S+1)^2}{3(2S^2+2S+1)} \right\}^{1/2} \tag{4.11}$$

$M_{sat}(0)$ being the zero temperature saturation magnetisation

$$\frac{\mu_{eff} H_0}{k_B T_C} = \left\{ \frac{30S^2}{(2S^2+2S+1)} \right\}^{1/2} \tag{4.12}$$

where $\chi_0 H_0 = M_S(0)$ and μ_{eff} is the associated fluctuating moment, while

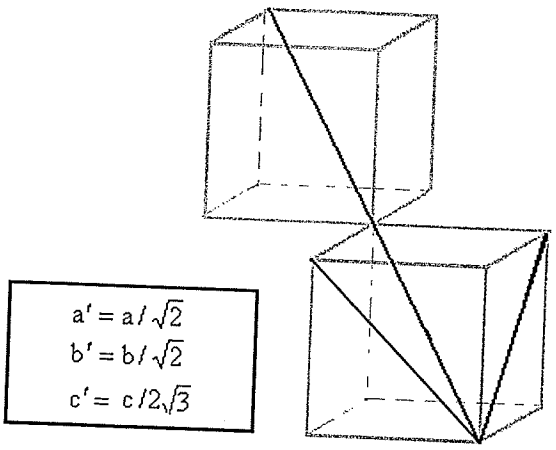

Figure 4.13 The illustration showing the relationship between the rhombohedral unit cell (the three vectors in black) and the "pseudo" cubic unit cell (the cubes in light gray).

$$\frac{D M_S(0)^{\delta}}{H_0} = 1 \tag{4.13}$$

Table 4.1 summarizes the reduced critical amplitudes in various models for a range of spins values, along with the critical amplitudes estimated from the experimental data. The (reduced) critical amplitudes show not only a spin and model dependence, but also a structural dependence. In table 4.1, the theoretical critical amplitudes were quoted for an fcc lattice, mainly because results are available for a wider range of spin values on such a lattice [66-68]. As far as lattice structure is concerned, $La_{1-x}Ba_xMnO_3$ near the optimal doping level ($x \sim 0.3$) is usually described by a rhombohedral unit cell with $R\bar{3}c$ space group. The relationship between this rhombohedral unit cell and the "pseudo" cubic primitive cell is illustrated in figure

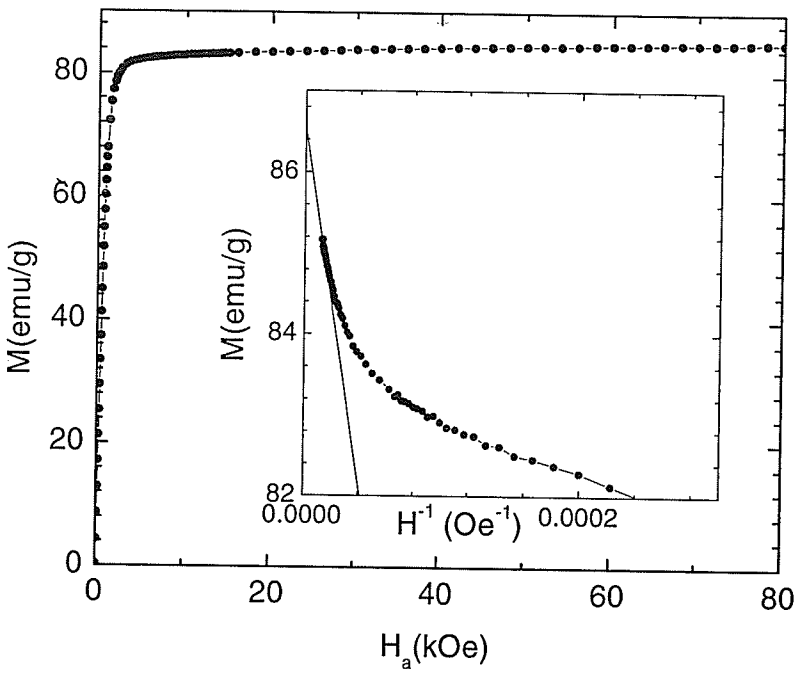

Figure 4.14 The main body of this plot represents the magnetization isotherm measured at 2 K up to 80 kOe; the inset shows the magnetic moment versus 1/H plot, where the vertical intercept from a linear fit to several high field points yields an estimate of the saturation magnetization.

4.13. Typically, from room temperature lattice parameter data (Moutis et al [69]), "pseudo" cubic dimensions a=b=3.9120 Å, c=3.9001 Å can be deduced; data from Beznosov et al. [13] indicates the same type of unit cell with marginally larger dimensions a=b=3.9165 Å, c=3.9061 Å.

The zero-temperature saturation magnetization $M_{sat}(0)$=86.25emu/g, estimated from the 2 K magnetization isotherm using an M vs H_a^{-1} plot for data between 60 – 80 kOe, is shown in figure 4.14. Based on the spin only assumption, the Ba composition is

estimated to be x=0.27(0) ± 0.003; the average spin value μ is 1.87. The experimentally deduced critical amplitude $M_S(0)/M_{sat}(0)$ is about 1.40, which agrees with the theoretical prediction of the Heisenberg model with S>1/2. From $\chi_0 H_0 = M_S(0)$, a field H_0, as high as 1780 kOe, can be estimated. By assuming a reduced critical amplitude, $\mu_{eff}H_0/k_BT_C$, which follows the Heisenberg picture (1.58), the effective moment is deduced to be $\mu_{eff} = 3.22\ \mu_B$; comparing with the low temperature spin-only estimation, $\mu_{eff} = 3.73\ \mu_B$, there is about 14% difference, which suggests that the spin-only assumption may overestimate the effective moments, possible due to spin canting. The reduced critical amplitude $DM_S(0)^{\delta}/H_0$ is estimated using the δ value obtained from the critical analysis ($\delta = 4.83$) and yields a value of 1.15; obviously, the D value is marginally higher than the prediction of mean field theory. Moreover, it is also higher than the lowest limit of the fcc Heisenberg prediction in classic limit ($S \rightarrow \infty$). However, taking into account the uncertainty in D by comparing isotherms within the quoted error of ± 0.5 K of T_c, the upper limit for D will fall into the range of the Heisenberg model prediction for the classical limit.

4.5.4 Critical analysis at higher fields from ac susceptibility data

In addition to the critical analysis mentioned above using magnetization isotherms, critical analysis based on the temperature-dependent ac susceptibility data has been performed between fields of 20 and 85 kOe. Figure 4.15 presents ac

susceptibility as a function of temperature in various static biasing fields. As discussed in Chapter 2, such plots provide an alternate way to extract the critical exponents. Specifically, equations (2.17), (2.21) – (2.23) relate the peak susceptibility, χ_m, the (reduced) peak temperature, t_m, (and T_m) to the internal field, H_i, in various ways. The principal features of this figure are the peaks near 250 K, which shift toward higher temperature, with an associated amplitude (χ_m) decrease, with increasing static field. These maxima delineate the crossover line (the dotted line in figure 4.15); above this line the magnetic response is temperature dominated, while below this line the magnetic response is field dominated. Figure 4.16(a) plots the peak temperatures T_m against $H_i^{1/(\gamma+\beta)}$ (the 3D Heisenberg values $\gamma+\beta=1.75$ was used here)' from which T_c=240.2 K was obtained on extrapolating data points to zero internal field. Comparing with the Curie temperature estimated from the modified Arrott plots (figure 4.8), the ordering temperature estimated here is about 2% smaller; this may be due to the different measurement processes*. Figure 4.16(b) replots the reduced temperature t_m versus internal field H_i on a double logarithmic scale as a test of equation (2.22); the slope of these data points yields $\gamma+\beta = 1.74 \pm 0.02$, which shows excellent self-consistency. The susceptibility exponent $\gamma = 1.38 \pm 0.01$ is obtained by fitting the temperature dependence of the peak susceptibility, χ_m, namely,

* Magnetization isotherms are measured at a fixed set of temperatures by sweeping the field, while the ac susceptibility data presented in figure 4.15 are collected by scanning temperature in a fixed field. Small differences can thus result due to the use of finite sweep rates in both cases.

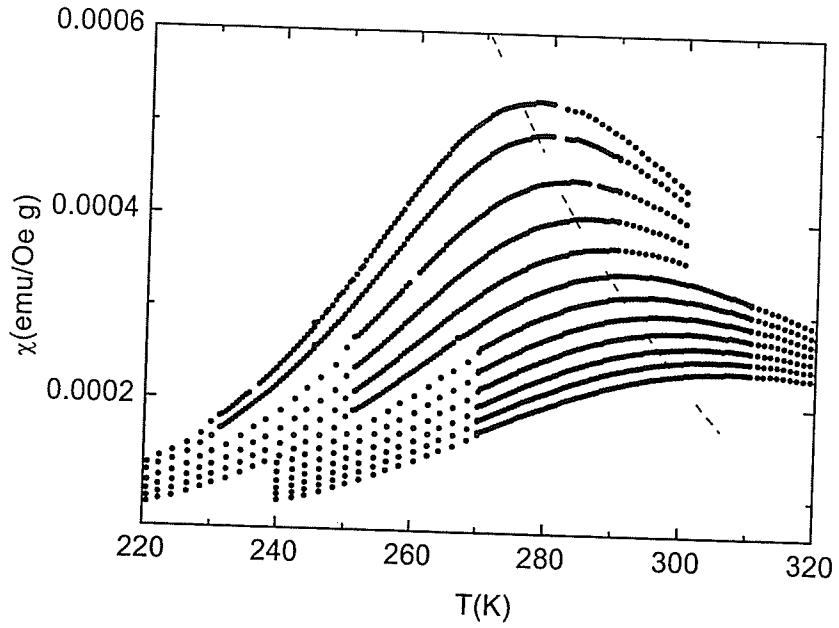

Figure 4.15 Selected temperature dependent ac susceptibility curves measured at static biasing fields of 32 kOe (top), then 35 kOe to 85 kOe (bottom) in 5 kOe steps; the dotted line indicates the crossover line.

χ_m vs $t_m^{-\gamma}$, which is consistent with the value obtained from low field (< 35 kOe) magnetization isotherms. Figure 4.16(d) reproduces a test of equation (2.23), namely, $\chi(h, t_m) \propto h^{(1-\delta)/\delta}$. A least-square fit yields the equation of state exponent $\delta = 4.84 \pm 0.09$, again in excellent agreement with the value from the critical isotherm (figure 4.11). Most importantly, the δ value found here is independent of the choice of the ordering temperature, T_c, while the value obtained from critical isotherm shows a strong dependence on the choice of T_c. From the above discussion, the 3D Heisenberg-like critical behaviour of the present specimen can be extended to an

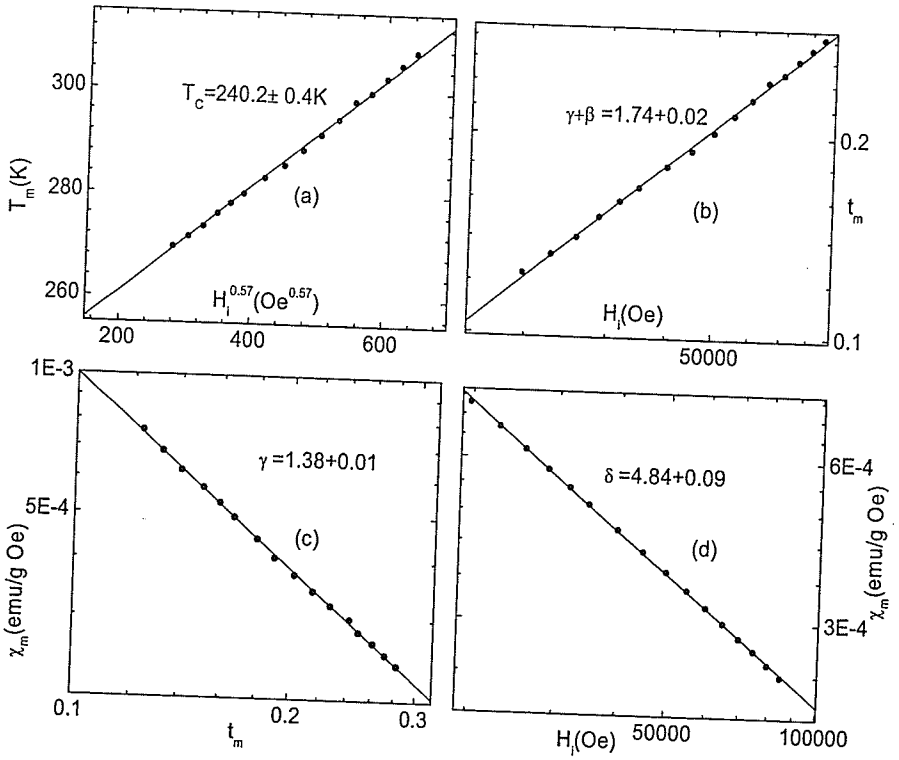

Figure 4.16 The plots showing the susceptibility data fits to find critical exponents.

applied field as high as 85 kOe, without any indication of a crossover phenomenon (frequently to mean field values).

In recent studies of the critical behaviour of single crystal $La_{1-x}Sr_xMnO_3$, Kim et al [61] reported exponents values ($\gamma = 1.27 \pm 0.06$, $\beta = 0.40 \pm 0.02$, $\delta = 4.12 \pm 0.33$ and $\alpha = 0.05 \pm 0.07$ for $x = 0.25$) which fall between mean-field and 3D Ising model

predictions ($\gamma = 1.237$, $\beta = 0.326$, $\delta = 4.789$, $\alpha = 0.11$) [24]; studies in a single crystal $La_{0.7}Sr_{0.3}MnO_3$ specimen [70] also show similar critical exponents ($\gamma = 1.22 \pm 0.03$, $\beta = 0.37 \pm 0.04$, $\delta = 4.25 \pm 0.2$) intermediate between the two models mentioned above. In an attempt to evaluate the applicability of the 3D Ising model to the present system, the following analysis also was carried out. Arrott plots based on Ising critical exponents yield plots of comparable quality plot as figures 4.8 (not reproduce here), which supports the earlier assertion – critical exponents can vary over a certain range without a significant change in the modified Arrott plot. However, the corresponding power-law plots using $M_S(T)$ and $\chi_i(T)$ deduced from such modified Arrott-plots are not self-consistent. They iterate towards higher (i.e. Heisenberg-model) exponent values. This indirectly supports Heisenberg - like behaviour in the present Ba substituted sample.

4.5.5 Discussions and conclusions

In a double exchange system with a second-order phase transition, a Monte Carlo simulation [71] indicated that such a transition should belong to the universality class of the isotropic short range 3D Heisenberg model, as confirmed experimentally in this sample from a careful critical analysis. Critical analysis of a single crystal $La_{0.7}Pb_{0.3}MnO_3$ specimen reported a field-induced crossover from the mean-field model to the Heisenberg model at a field of 10 kOe [72]. Obviously, the critical

analysis reported here, based on magnetization isotherms in fields up to 30 kOe, do not support this scenario and the ac susceptibility data extends the range of validity of 3D Heisenberg exponents to a higher field of 85 kOe .

The deviations from Heisenberg exponents in two single crystal Sr specimens [61, 70] mentioned above have been interpreted using a shape induced uniaxial anisotropy (Kim et al.[61]). From the relationship between the anisotropy energy, $K\xi^3$, and the thermal energy, k_BT_c, Kim et al. proposed a criterion to decide the crossover temperature from the 3D Heisenberg to the 3D XY and then to 3D Ising model exponents. If the hard-axis anisotropy energy, $K_H\xi^3$, is on the order of the thermal energy, k_BT_c, a crossover from the 3D Heisenberg to 3D XY model exponents should occur near a reduced temperature of $t \sim 0.02$; at a lower temperature, $t \sim 4 \times 10^{-3}$, a crossover from 3D XY to 3D Ising model behaviour should be expected. (This crossover temperature is obtained by comparing the easy-axis anisotropy energy and the thermal energy, i.e. $K_E\xi^3 \sim k_BT_c$). Critical analysis, from both magnetization isotherms and temperature-dependent ac susceptibility data, in the present sample, do not show any crossover effects. This behaviour would require the product $K_H\xi^3$ to be at least an order of magnitude smaller than in the corresponding Sr doped system. As far as the critical analysis is concerned, Ba doped manganites have not been studied as extensively as the Sr substituted system. Available data on a polycrystalline $La_{0.67}Ba_{0.33}MnO_3$ specimen [69] showed some exponents ($\gamma = 1.29$ and $\beta = 0.464$) intermediate between mean-field and Heisenberg exponents, while critical analysis

on an epitaxial film ($La_{0.7}Ba_{0.3}MnO_3$) [73] yielded mean-field exponents ($\gamma = 1.04 \pm 0.04$, $\beta = 0.54 \pm 0.02$, $\delta = 3.08 \pm 0.04$) over a comparable reduced temperature range to that covered in the present studies. These latter exponent values might possibly arise as a result of a change from Heisenberg to Ising behaviour induced by a tetragonal distortion in the film, accompanied by an enhanced dipole-dipole interaction [74, 75] (emanating from large spin moments). It is also possible that the correlation length exceeded the film thickness of 150 nm close to T_c causing complications due to reduced dimensionality; a detailed check, however, on this possibility has yet to be made.

In summary, the analysis of detailed magnetization measurements in low and intermediate fields, supplemented by high static biasing field ac susceptibility data, on single crystal $La_{0.73}Ba_{0.27}MnO_3$ reveal the occurrence of a second-order/continuous ferromagnetic to paramagnetic phase transition. The nature of this transition can be described by the isotropic 3D Heisenberg model. Such a result is consistent with a model simulation for a double-exchange system, where anisotropy does not play a significant role.

4.6 Behaviour of Single Crystal $La_{0.73}Ba_{0.27}MnO_3$ in the Ferromagnetic Regime

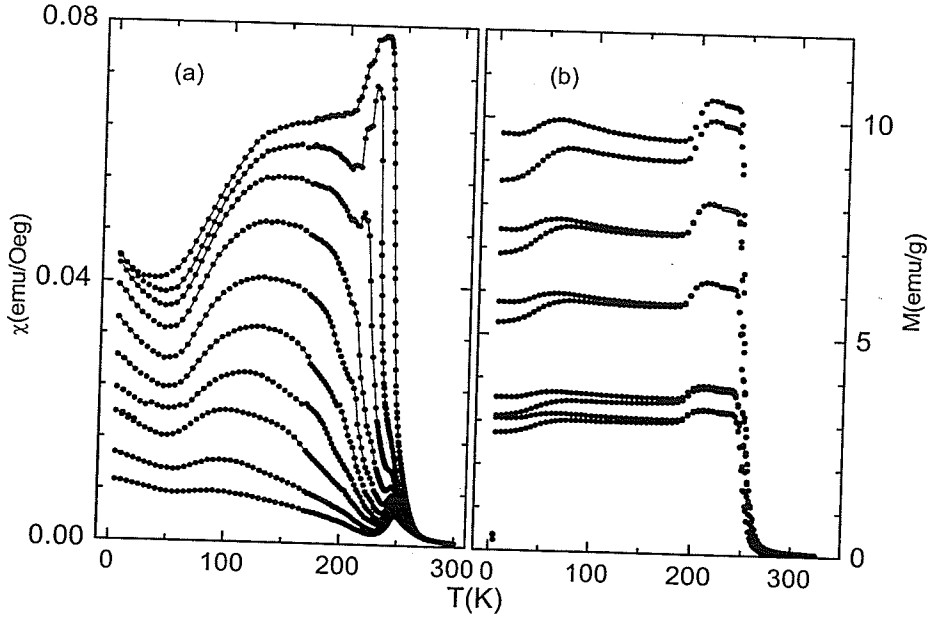

Figure 4.17 (a) ac susceptibility measured on warming in static applied fields of 200 Oe (top) 400 – 1000 Oe (in 100 Oe steps), 1200 Oe and 1400 Oe (bottom); (b) the temperature dependence of the field – cooled (FC) and zero-field-cooled (ZFC) magnetization measured in nominal applied fields of 30 Oe (bottom) , 40 Oe, 60 Oe, 80 Oe and 100 Oe (top).

As shown in figure 4.6(a), the zero-field ac susceptibility curve of $La_{0.73}Ba_{0.27}MnO_3$ is complex, as can be seen in more detail in figure 4.17(a). Here the temperature dependent ac susceptibility in different static basing fields is reproduced. The secondary peak near 250 K in figure 4.17(a) has been analyzed from a

conventional critical behaviour point of view, from which Heisenberg-like critical exponents have been extracted. The point that needs to be addressed here is the susceptibility drop/moment reduction near 200 K.

Previous studies suggest that structural changes can result in a moment reduction in $La_{1-x}Ba_xMnO_3$ at a certain doping level. Laukhin et al. [76] found a structural phase transition from a high temperature rhombohedral (*R*) to a low temperature orthorhombic (*O*) phase near 175 K in a single crystal $La_{0.8}Ba_{0.2}MnO_3$ specimen; accompanying this structural phase transition, there is a reduction in the magnetization and some incremented change in the resistance. The temperature dependent X-ray data from the same sample provided direct evidence of the existence of a structural phase transition from an *O* phase ($R\bar{3}c$) to an *R* phase (*Pbmn*); moreover, the *Pbmn* and $R\bar{3}c$ phases coexist, at least within the temperature interval $185 < T < 196$ K. Similar moment reductions associated with a first-order $R\bar{3}c \Leftrightarrow$ Imma structural phase transition has also been observed in a Ba-substitution single crystal sample with optimal doping ($x \approx 0.33$) [77]. The composition of the present sample (x=0.27) falls in the composition range defined by the two specimens mentioned above. The moment reduction around 200 K evident in figure 4.6(a) and 4.17(a) unquestionably is linked to a phase transition from a high moment/temperature *R* phase to a lower moment / temperature *O* phase. A careful examination of figure 4.17(a) reveals that features characterizing such a structural change are suppressed by increasing fields; it eventually vanishes above a static field

of 500 Oe. These characteristics are confirmed in figure 4.17 (b), where the field cooled (FC) and zero field cooled (ZFC) curves in several different fields are reproduced. Both the FC and ZFC branches display a very clear moment/magnetization drop around 200 K; below T_c, irreversibility between FC and ZFC branches is observed.

The low temperature structure evident in Fig 4.6(a) and 4.17(a) in the interval 50 - 100 K – particularly the fall in $\chi_{ac}(0,T)$ – mirrors the moment reduction established near 200 K. As a result, a careful analysis of the magnetic properties below 100 K of this system was undertaken. While the full details of this investigation are presented elsewhere [78, 79], a summary is presented here for completeness.

Figure 4.18(a) and (c) reproduce a set of low temperature ($T< T_c$) isotherms that confirm the anomalous behaviour first revealed by ac susceptibility below 100 K. Figure 4.18 (b) presents the magnetization isotherms replotted in M^2 versus H/M format, i.e. Arrott plots for this specimen. A set of linearized lines outside the critical region indicate that the mean field exponents are appropriate to describe the behaviour, although the critical region shows 3D Heisenberg-like critical behaviour. However, the principle focus here is to present a summary of the thermal variation of low temperature spontaneous magnetization determined earlier. As discussed earlier, the spontaneous magnetization was estimated from the high field extrapolation in order to eliminate the technical contribution in low fields and

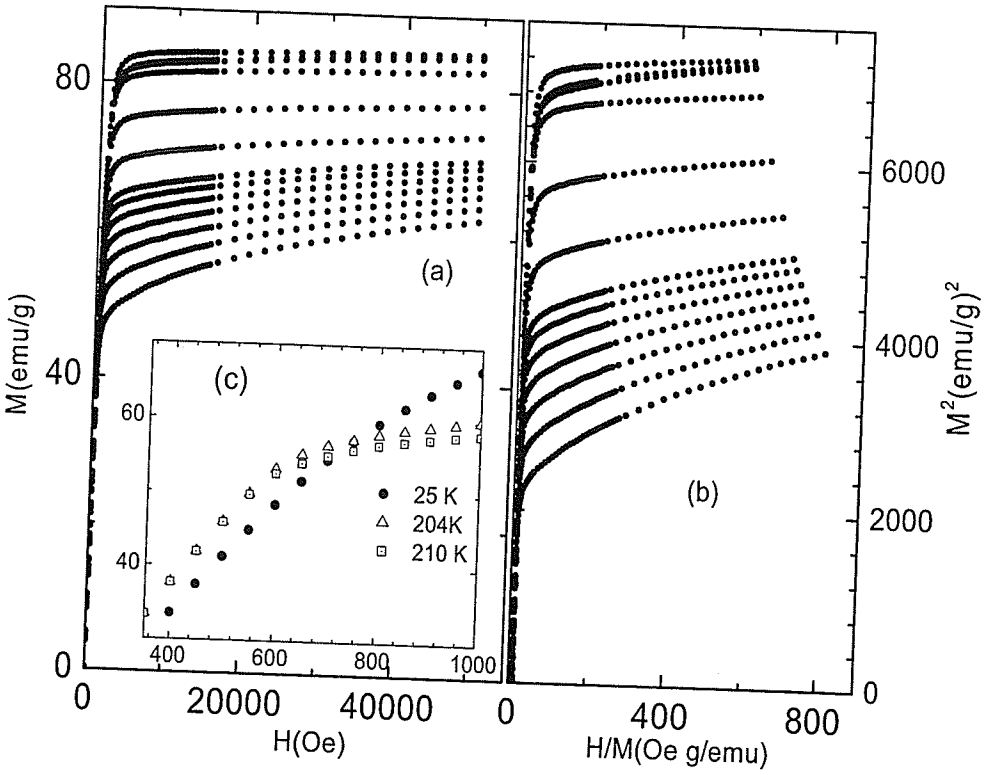

Figure 4.18 (a) Selected magnetization isotherms measured at 50 K (top), 5 K, 25 K, 100 K, 150 K, 180 K, 200-230 K (bottom) in 5 K steps; figure (b) the same data of (a) replotted in M^2 versus H/M format; (c) the selected low field curves of (a) indicate the crossover at 25 K (●), 204 K(△) and 210 K (□).

the temperature dependence of spontaneous magnetization estimated from intercept in figure 4.18(b) is reproduced in the main body of figure 4.19.

The spontaneous magnetization below 150 K so estimated can be fitted using a conventional approach based on low-lying acoustic mode spin-wave excitations, viz:

$$\hbar\omega_{ac} = \Delta + Dq^2 \tag{4.14}$$

Where Δ is the gap, a constant offset to account for small anisotropies or the application of an external magnetic field; D is the stiffness constant and q is wave vector. It is known that such a dispersion relation should result in the "Bloch $T^{3/2}$ law", namely, a spontaneous magnetization having a temperature dependence of [80]

$$\frac{M_S(T)}{Ms(0)} = 1 - \frac{1}{NS}\left(\frac{k_B T}{4\pi D}\right)^{3/2} \cdot \xi\left(\frac{3}{2}, \frac{\Delta}{k_B T}\right) \tag{4.15}$$

where $M_s(0)=Ng\mu_B S$ is the spontaneous magnetization at zero-temperature; $\xi(3/2)$ is Riemann-zeta function, defined as

$$\xi\left(\frac{3}{2}\right) = \sum_{a=1}^{a=\infty} a^{-3/2} \tag{4.16}$$

A least-square fit to the data between 60 and 140 K in the main body of figure 4.19 yields a gap $\Delta = 0.45\pm0.02$ meV and a stiffness constant $D = 65.7\pm2.5$ meV Å^2; low-temperature (below $0.1T_c$) field-dependent magnetization studies on a $La_{0.7}Sr_{0.3}MnO_3$ sample showed a much larger stiffness constant ($D = 154\pm5$ meV Å^2) [81]; neutron scattering data [82] on single crystal $La_{0.7}Ba_{0.3}MnO_3$ yielded a smaller gap ($\Delta = 0.20\pm0.04$ meV) and a larger stiffness constant D ($D = 152\pm3$ meV Å^2). Such compositional variations are consistent with those reported in the $La_{1-x}Ca_xMnO_3$ system [83, 84] ($D \approx 46$ meV Å^2 at $x = 0.2$, rising to 170 meV Å^2 at $x = 0.33$).

From figure 4.19, below 50 K, there is a clear magnetization drop from its "expected" value, which is emphasized in this figure by only plotting data below 30

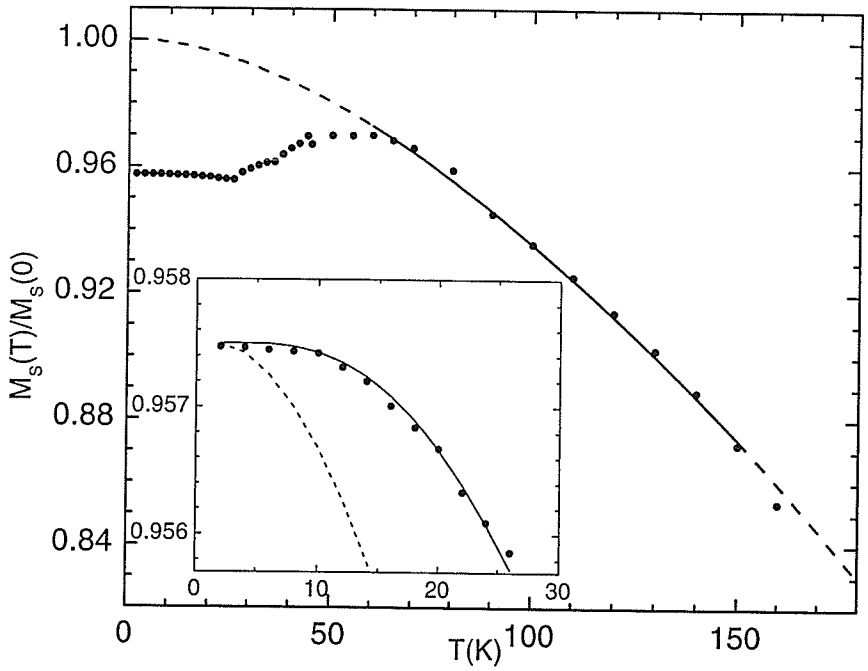

Figure 4.19 Plots of the reduced spontaneous magnetization ($M_s(T)/M_s(0)$) against temperature. Main figure: the solid line represents a fit to equation (4.15) between 60 and 140 K using D=65.7 meV Å^2 and Δ = 0.45 meV; the dashed line extends this fit beyond the temperature interval specified. Inset shows data below 30 K; the dashed lines uses the parameters corresponding to the main figure scaled to $M_s(T)/M_s(0)$ = 0.9575; the solid line uses the same D and scaling factor but with Δ increased to 2.35 meV.

K. Obviously, the fit using high temperature parameters (dotted line) cannot describe the low temperature behaviour here, it will yield a much stronger temperature dependent in $M_s(T)$ than is observed. A modified fit based on equation (4.15) was thus employed by using the higher temperature D (D = 65.7±2.5 meV Å^2) and a revised spontaneous magnetization Ms_{at}=0.9575($Ng\mu_B S$) = 81.73 emu/g. A least-square

fit, the solid line in the inset of figure 4.19, yields a gap $\Delta = 2.35$ meV, which is significantly larger than the value obtained from the higher temperature fit ($\Delta = 0.45$ meV); this gap is however close to the value ($\Delta = 2.51 \pm 0.46$ meV) reported in a single crystal $La_{0.7}Pb_{0.3}MnO_3$ sample [85]. Irrespective of the specific approach used or the parameters characterizing it, the 4% decline in the spontaneous magnetization as expressed in the modified $M_s(0)$ appearing in the fit to equation (4.15) unequivocally reflects an effective moment reduction; however, the mechanism leading to such reduction is very difficult to identify from such macroscopic measurements.

Nevertheless the origin of this fall is clearly revealed by the magnetization isotherms in figure 4.18 (a) and (c); magnetization isotherms measured below 60 K lie below those measured above 60 K. Such an inversion leads to a moment reduction in $M_s(T)$ below 60 K. The crossover of these isotherms near 700 Oe can be clearly seen in figure 4.18(c). It should be emphasized that this process is a gradual one without any signatures of metamagnetic transitions. The exact origin of moment reductions in present specimen is still unclear; however, spin canting - a long expected result in double exchange system [86] - is one possibility. As discussed in the review of CMR effects, the interaction energy in double exchange system scales with $\cos(\theta/2)$, and competes with the superexchange interaction, which is proportional to $\cos(\theta)$. Due to the presence of the $\cos(\theta/2)$ term, the pure antiferromagnetic spin alignment is unstable with respect to the spin canting [87].

Spin canting can account for the scenario describe here, although likely not in the form originally proposed by de Gennes [86]; it would yield a (uniform) canting angle close to 17^0 ($\theta = \cos^{-1}(0.9575)$). However, these data are also consistent with a helimagnetic/spiral magnetic structure forming with an axis parallel to the field direction – the long axis of this single crystal – with a similar disinclination angle. Other possibilities for this effect, particularly the fall in χ_{ac} below 100 K, need to be considered. The inhomogeneous ordering of the type reported in the $La_{1-x}Ca_xMnO_3$ system [88] for $x \leq 0.2$ might initially appear to provide a potential explanation of a moment reduction in this specimen; however, as the insulating character prevalent at these doping levels plays an important role in establishing such order, this explanation seems unlikely in the low temperature metallic phase of the present system. In addition, technical sources do not appear to underlie the fall in χ_{ac} below 100 K as this effect does not correlate with the variation in the coercive field $H_c(T)$, figure 4.6(b), nor χ_{ac} frequency dependent in this regime. The exact origin of this drop is still unclear; it is very unlikely to result from a further structural change as none have been reported in this temperature range by previous studies. A decline in $\chi_{ac}(0,T)$ below 100 K has been noted previously [77], but it was not investigated further.

In summary, the temperature dependent spontaneous magnetization $M_s(T)$ in single crystal $La_{0.73}Ba_{0.27}MnO_3$ can be fitted by a gapped spin wave dispersion relation, which yields a gap $\Delta = 0.45(\pm0.02)$ meV and $D = 65.7(\pm2.5)$ meVÅ^2

between 60 and 140 K (~T_c/2); the spontaneous magnetization below 30 K can be fit using same equation with a larger Δ = 2.35 meV. Different magnitudes of spontaneous magnetization drops have been observed below 60 K, especially, 4% moment reduction in zero-temperature, which is consistent with a spin canting – a long predicted effect in doped double exchange manganites.

$La_{0.73}Ba_{0.27}MnO_3$ is one of the few manganese perovskites exhibiting Heisenberg exponent values. Further investigations, therefore, appear necessary to confirm the presence of 3D Heisenberg exponents in other system with small anisotropy (Ba doping, for example) and to investigate more fully crossover effects in systems with anisotropy (i. e. Sr doping). The moment reduction reported above in the Ba-doped single crystal also suggests that the microscopic spin structure needs to be investigated using, for example, neutron scattering. Indeed, neutron scattering measurements [82] on this system indicates that the acoustic spin-wave stiffness D does not approach zero temperature monotonically.

4.7 The Nature of the Phase Transitions in Single Crystal $La_{0.73}Ca_{0.27}MnO_3$

4.7.1 Overview of the phase transitions in $La_{1-x}Ca_xMnO_3$

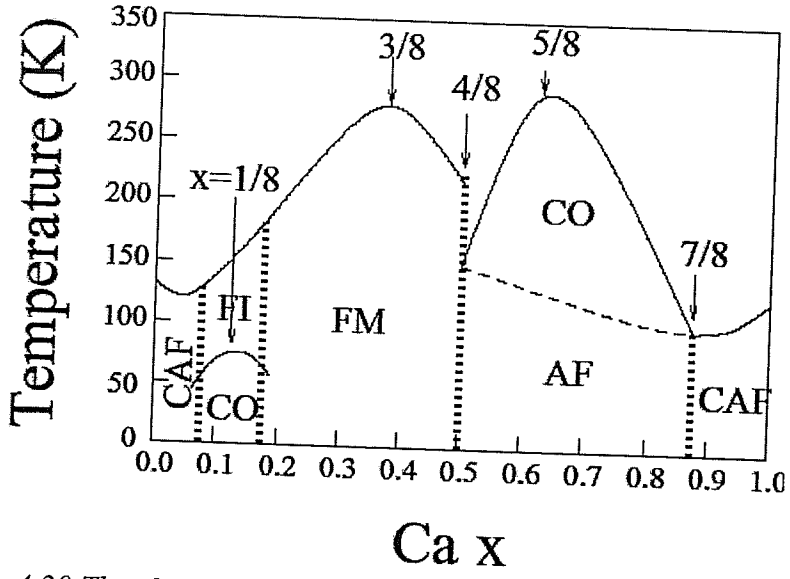

Figure 4.20 The phase diagram for the archetypal system $La_{1-x}Ca_xMnO_3$ [12].

Figure 4.20 is a simplified phase diagram for the archetypal manganite system $La_{1-x}Ca_xMnO_3$ [12]. Most of recent studies have been focused on the optimum doping level $x \approx 0.33$ where there is a strong ferromagnetic coupling and a large magnetoresistance; it is believed that the double exchange mechanism is dominant in this region. At a higher doping level ($x > 0.5$), the system changes from a

paramagnetic insulator to an antiferromagnetic state with decreasing temperature and an intermediate charge ordered state can also appear for doping level $0.50<x<0.85$. Around a narrow range of doping levels near $x \approx 0.5$, both ferromagnetic and antiferromagnetic states can occur; upon cooling, the system first changes from a paramagnetic insulator to a ferromagnetic metal (~220 K), then to an antiferromagnetic state (~150 K). This behaviour is usually attributed to the competition between double exchange and superexchange coupling. Regarding the nature of the phase transition around the optimum doping level, specific heat and thermal expansion studies of polycrystalline samples of $La_{0.65}Ca_{0.35}MnO_3$ showed that the ferromagnetic ordering arises from a thermodynamic first-order transition [89]; magnetization and specific heat data for an $x = 0.33$ sample have also been interpreted as indicating the occurrence of a first-order/discontinuous magnetic phase transition near optimal doping [90], although recently the interpretation of such data has been questioned [91]. Small angle neutron scattering reveals a discontinuous change in the scattering at T_c for wave vectors below $\approx 0.065 Å^{-1}$ on a single crystal $La_{0.7}Ca_{0.3}MnO_3$ sample [83], which suggests that a first-order phase transition persists at this composition; analysis based on Banerjee Plots also showed the existence of a first-order phase transition in $La_{2/3}Ca_{1/3}MnO_3$ sample near the optimal doping [92]. However, such first-order transitions (in the T_c versus x plane) terminate at a tricritical point near $x = 0.4$; this composition was considered to be a boundary separating first- ($x<0.4$) from second-order ($x>0.4$) phase transitions. At

the tricritical point, x=0.4, the modified Arrott plot analysis based on magnetization data suggests a continuous transition with a set of exponents close to those predicted for such a tricritical point (α=0.48, β=0.25, γ=1.03, δ=5.0) [90]. Below optimal composition, a volume contraction (ΔV=0.13%) occurring in the vicinity of a paramagnetic to a ferromagnetic transition at $x = 0.25$ suggests that this transition retains first-order characteristics [9]; at the lower composition of x = 0.2, magnetization studies on single crystals using Banerjee plots show the ferromagnetic to paramagnetic transition is second-order in nature and can be characterized by Heisenberg exponents [93]. The present studies focus on the compositional region between the lower composition, x=0.2, mentioned above and the optimum doping level x=0.33; its purpose was to investigate the nature of the phase transition close to the localized to itinerant transport transition (a ferromagnetic insulator to ferromagnetic metal transition), i.e. x=0.27.

The sample used was a 0.12 g single crystal (provided by Y. Mukovskii and D. Shulyatev of Moscow State Steel and Alloys Institute) with approximate dimensions ($10 \times 1.4 \times 1.4\ mm^3$) grown using the floating-zone technique [94], displaying a mosaicity of less than 1°. Measurements of the dc magnetization and the ac susceptibility were carried out simultaneously in a Quantum Design Model 6000 PPMS magnetometer/susceptometer using the measurement procedure described in Chapter 3.

4.7.2 Evidence suggesting a first-order phase transition

Figure 4.21(a) presents the temperature dependence of the zero-field ac susceptibility, $\chi(0,T)$, measured on both warming and cooling at 2.4 kHz in a 30 mOe driving field. It can be seen directly from figure 4.21(a) that there is no discernible hysteresis (even measured at a very slow temperature sweep rate of 0.1K/s), which is usually a signature of a first-order phase transition. From this figure, an ordering temperature $T_c \approx 232$K was estimated by finding the temperature corresponding to the minimum slope of this plot, i.e. $d\chi/dT|_{MIN}$. Figure 4.21(b) shows the temperature dependence of the coercive field, H_c, between 5 K and 250 K estimated from complete field-dependent magnetization curves. No coercive field can be distinguished above T_c and nowhere does the coercive field exceed 10 Oe; this confirms the high quality of this sample. A high quality single crystal sample without grain boundaries provides an ideal platform to investigate the order of phase transitions. Figure 4.22(a) shows magnetization isotherms measured in the increasing field mode in the vicinity of the ordering temperature. The first feature that should be noticed is the "S" shape of curves for temperature above 237 K, which differ dramatically from the conventional isotherms associated with a pure second-order phase transition. Magnetization isotherms with such features are usually associated with a metamagnetic phase transition. Similar results have been reported in different systems, including polycrystalline $x = 0.33$ perovskite manganites specimens [90],

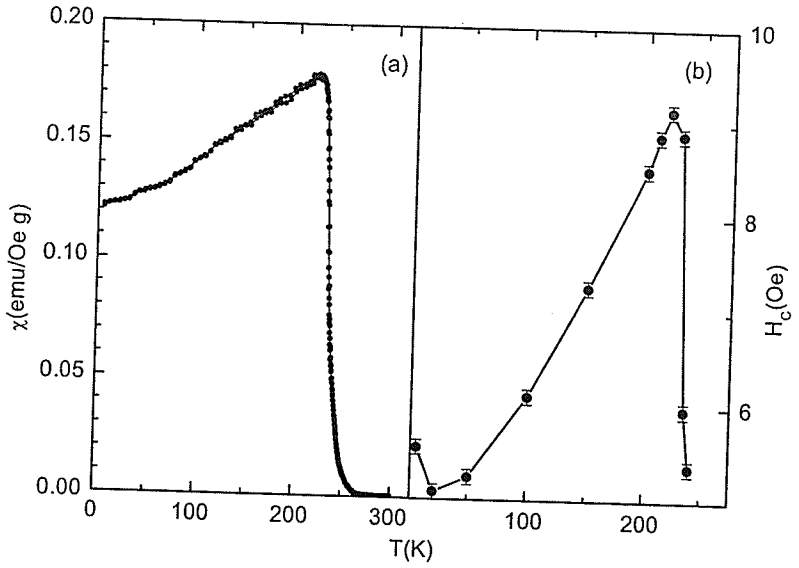

Figure 4.21 (a) The zero-field susceptibility measured on warming and cooling processes. (b) The temperature dependence of the coercive field, H_c.

intermetallic compounds (such as Gd_2In [95] and doped $CeFe_2$ [96]) and the ferromagnetic shape memory alloy Ni-Mn-Ga system (will be discussed in chapter 5 in detail)*. The low field structure (<1.5 kOe) evident in this figure originates from technical contributions, such as domain wall motion, domain reorientation/rotation, which lead to the small coercive field, H_c, in figure 4.21(b). Figure 4.22(b) replots the magnetization isotherms in a M/H versus M^2 format; the slope of such plots – the Banerjee criterion – have been widely used to establish the order of such transitions.

* In Gd_2In and doped $CeFe_2$ as well as the Ni-Mn-Ga system, the relevant phase transitions are field-induced order-order phase transitions; by contrast, perovskite manganites display an order to disorder phase transition.

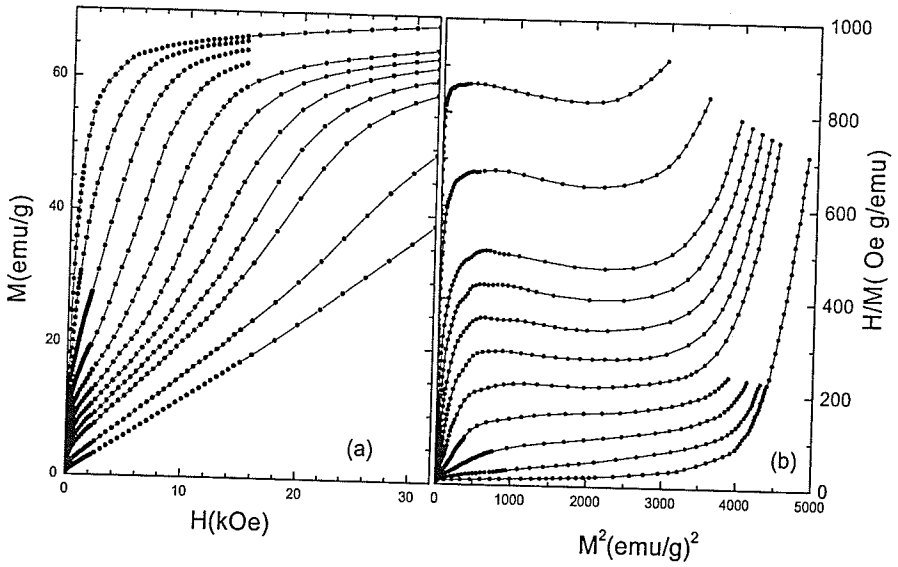

Figure 4.22 (a) Magnetization isotherms measured in an field-increasing mode for temperatures increasing from 234 K(top) to 250K, then 255 K and 260 K (bottom). (b) Magnetization isotherms replotted as H/M versus M^2 based on the data in (a).

A positive initial slope, reflecting a positive coefficient $\alpha_4(T)$ in the Landau expansion, suggests a second-order/continuous phase transition, while a negative slope suggests a first-order/discontinuous phase transition. Although the initial slopes in figure 4.22(b) are positive, clear negative slopes can be found at higher magnetization for temperature above 246 K; this indicates the existence of first-order characteristic in this transition. The thermodynamic basis of this modified criterion can be understood by including an additional term in the expansion of the free energy, as discussed in chapter 2.

Figure 4.23 shows a selection of magnetic isotherms measured in the vicinity of ordering temperature, T_c, in both field increasing and decreasing modes. Accompanying the "S" shaped curves mentioned earlier is a limited amount of hysteresis. Similar to that reported at $x = 0.33$ [90], the actual hysteresis

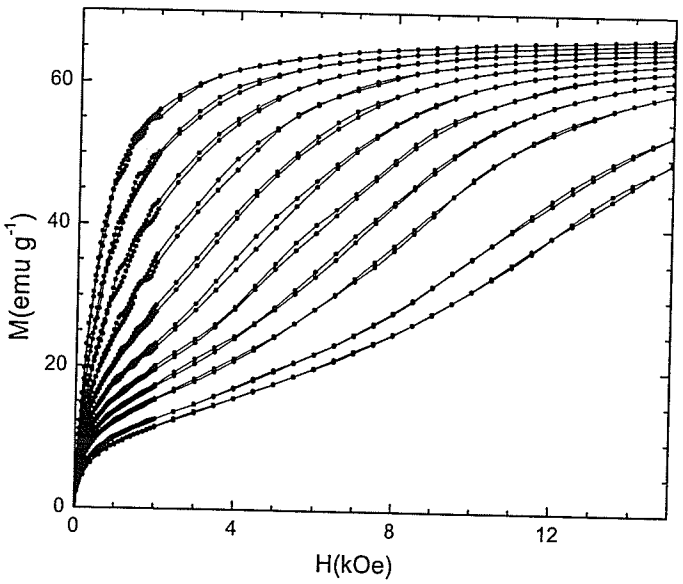

Figure 4.23 A selection of magnetization isotherms measured on both field increasing and field decreasing at temperature from 234 K (top) to 245 K (bottom) in 1 K step.

accompanying this metamagnetic transition is confined to a narrow region of the (H-T) plane, as figure 4.23 confirms. From the data in figure 4.23, the metamagnetic field, H_M, which characterizes the transition field from the ferromagnetic state to a paramagnetic state, can be estimated for different temperatures in a similar manner to that used for the intermetallic compounds mentioned above, namely, the maximum in

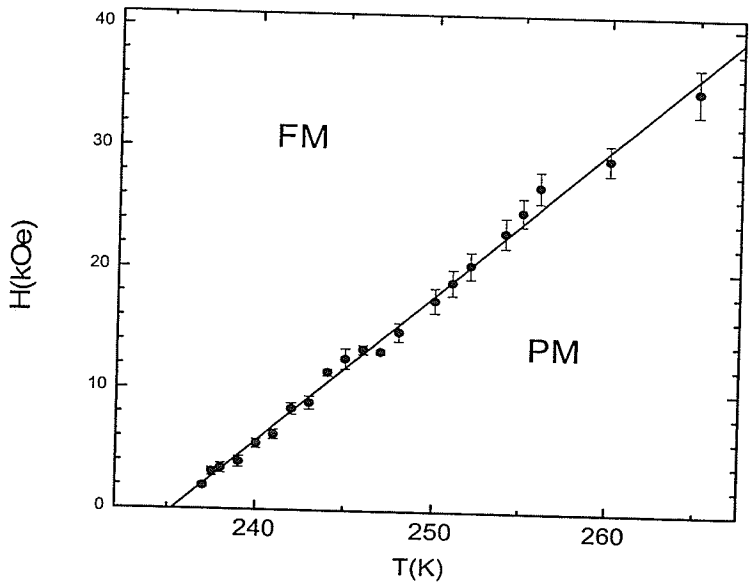

Figure 4.24 The metamagnetic field, H_M, as a function of temperature. The data were taken from figure 4.23 in both increasing fields and decreasing fields. The metamagnetic boundary separates the ferromagnetic region from paramagnetic region in the (H-T) plane.

dM/dH. Metamagnetic fields, H_M, (corrected for demagnetization effects) estimated from both field increasing and field decreasing magnetization isotherms as a function of temperature are presented in figure 4.24. A least square fit to these data yields a slope $dT_c/dH_M \approx 8\times10^{-4}$ K Oe^{-1}; this value is smaller than the value $dT_c/dH_M \approx 1.9\times10^{-3}$ K Oe^{-1} estimated for $x = 0.33$ sample [90]. This difference may be due to the use of a different criterion for identifying the metamagnetic field H_M. Kim et al. [90] estimated H_M by finding the positive curvature d^2M/dH^2, indicative of reentrant ferromagnetism, in the magnetization isotherms. By contrast, the specific heat based

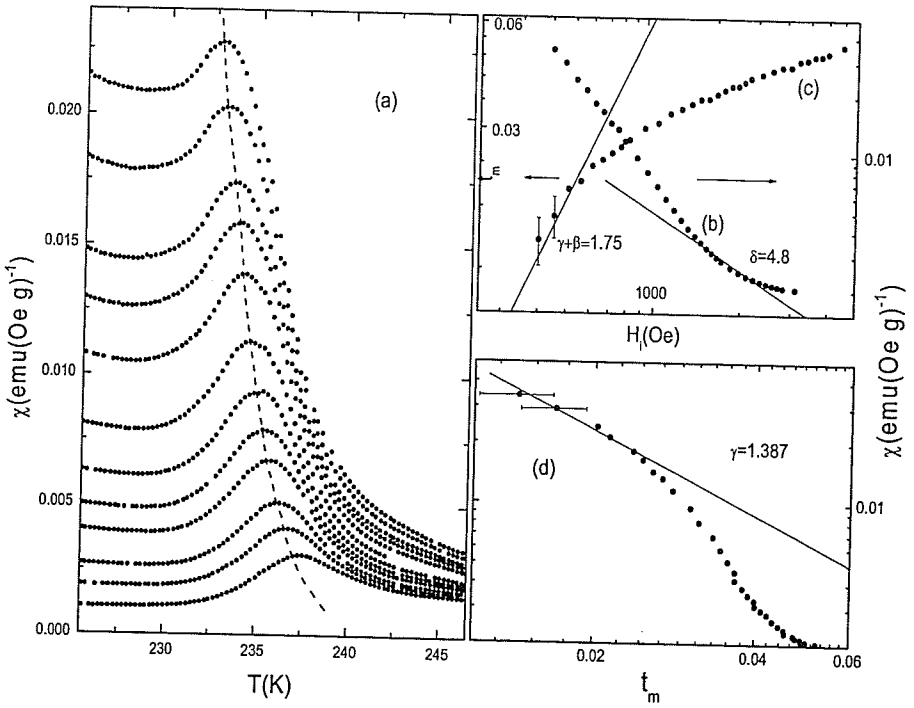

Figure 4.25 (a) The ac susceptibility χ, measured in applied static fields Ha increasing from 600 Oe (top) to 800 Oe in 50 Oe steps, in 100 Oe steps to 1200 Oe, in 200 Oe steps to 1600 Oe, and finally in 2000 Oe (bottom); the crossover-line is shown by the dashed line; double logarithmic plots of (b) the susceptibility maxima χ_m from (a) against internal field H_i, as a test of equation (2.23); (c) the reduced temperature t_m against internal field H_i as a test of equation (2.22) (d) the susceptibility maxima χ_m against reduced peak temperature t_m, as a test of $\chi(h,t_m) \propto t_m^{-\gamma}$. The solid lines drawn using Heisenberg exponents are for comparison.

estimates [97] yields a larger slope. Such field-induced shifts confirm the first-order character of this transition. In essence, the fitted line in figure 4.24 depicts the field-dependent phase boundary, which separates the paramagnetic state from the

ferromagnetic state in the field (H) – temperature (T) plane. The "S" shaped isotherms and associated hysteresis, as well as field-induced shifts in the (H-T) plane, are characteristics indicative of a first-order phase transition.

4.7.3 Evidence suggesting a second-order phase transition

The arguments supporting the simultaneous second-order nature of this transition are established by measuring a series of susceptibility versus temperature curves at various static biasing fields, figure 4.25(a). This series of curves exhibit a set of maxima that move upward in temperature while decreasing in amplitude as the superimposed static biasing field increases (these maxima could only be resolved for applied fields 400 Oe $\leq H_a \leq$ 4000 Oe). As described in chapter 2, maxima that behave in this way are a characteristic signature of a second-order/continuous phase transition. These maxima delineate the position of the crossover line in the (H-T) plane, above which the response is thermally dominated and below this line the response is field dominated; this crossover line ends at $H = 0$ in an end line point - the Curie/critical temperature T_c. The corresponding zero field susceptibility curve is reported in figure 4.21(a).

As discussed previously, with a pure second-order/continuous phase transition, the critical peaks in figure 4.25(a) are predicted to obey a series of asymptotic power-laws, and a set of exponents can be extracted from these power-laws. Specifically,

the peak susceptibility, χ_m, and the reduced peak temperature, t_m, should exhibit power law relationships with the internal field, H_i,, as summarized in equations (2.17), (2.21) – (2.23). Figure 4.25(b) plots the reduced peak temperature, t_m, against internal field, H_i, on a double-logarithmic scale, as a test of equation (2.22). Clearly, for the "crossover exponents" $(\gamma + \beta) > 0$, with increases in the internal field, H_i, the reduced temperature, t_m, increases; hence, the peak temperature, T_M, also increases, as confirmed in figure 4.25(a). Although data points here follow this trend, a straight line fit is clearly inappropriate. Figure 4.25(d) shows the reduced temperature, t_m, versus peak susceptibility, χ_m, curves on a log-log scale, namely, $\chi(h,t_m) \propto t_m^{-\gamma}$, which describes the singular behaviour of the susceptibility. Obviously, no power-law relationship can be found here either. Figure 4.25(c) is plotted as a test of equation (2.23), from which the equation of state exponent δ can be determined. An obvious curvature can be seen from figure 4.25(c); fitting between fields of 300 Oe-2000 Oe yields a very large δ value, whereas at higher internal fields (> 2000 Oe), the effective value of δ will be reduced. This peculiar behaviour is a reflection of the "S" shaped magnetization isotherms observed near the ordering temperature in figure 4.22(a) and figure 4.23. Qualitatively, the magnetization, M, along isotherms near the critical temperature should also show a power-law form, $M \propto H_i^{1/\delta}$, and their S-shaped behaviour through the metamagnetic transition will lead to large (effective) values for δ (on the flattened section of the isotherm), which would subsequently decrease as the field increases. On the basis of the above discussion, none of these power-laws

are satisfied and no critical exponents can be deduced. First, this reflects the continued presence of the metamagnetic transition as $H \rightarrow 0$, although the metamagnetic field, H_M, is difficult to access from magnetization isotherms in low field. Second, the magnetization exponent β and susceptibility exponent γ are usually obtained from the thermal variation of the spontaneous magnetization, M_S, and initial susceptibility, χ_i, which are normally derived from extrapolations to both axes in figure 4.22(b) (the Arrott Plot). The unconventional Arrott Plot in figure 4.22(b) makes such extrapolations difficult, especially in intermediate fields. Unphysical exponents have been extracted from such extrapolations, which confirm the conclusions made for the critical analysis based on susceptibility data.

4.7.4 The coincidence of first- and second-order phase transitions

A striking feature is shown in figure 4.26, where the crossover line from figure 4.25(a) and the metamagnetic boundary from figure 4.24 are plotted in the internal field, H_i, - temperature, T, plane. Carefully examination of this plot reveals that the two sets of data are coincident within experimental uncertainty; namely, close to the localized limit (i.e. $x = 0.27$), the transition simultaneously displays both first-order and second-order characteristics, and these characteristics are coincident. As is evident from figure 4.26, the metamagnetic boundary can be tracked to much higher field (13 kOe in figure 4.23) than the crossover line, since the susceptibility maxima

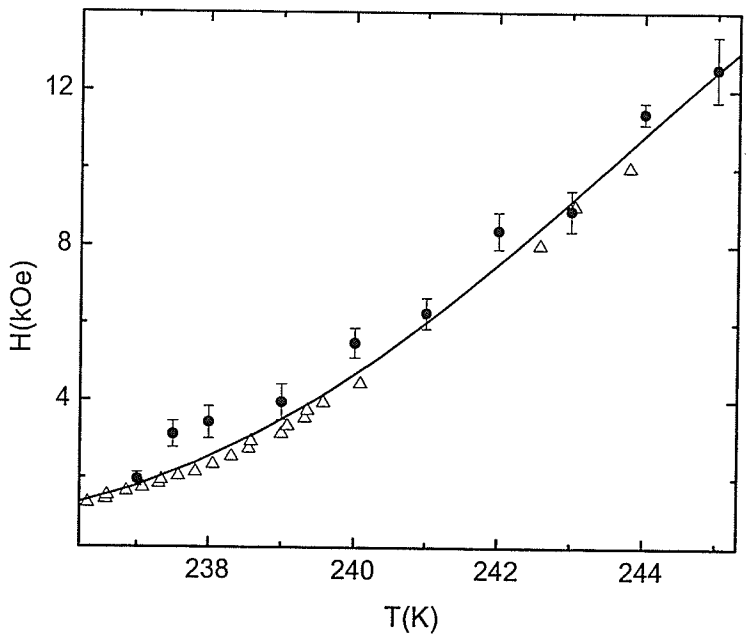

Figure 4.26 The metamagnetic boundary (●) from figure 4.24 and the crossover line (Δ) from figure 4.25 (a) are plotted as a function of temperature.

are suppressed in amplitude and broadened in temperature with increasing field. In contrast, in the low-field limit (below 1.5 kOe), due to technical contributions, estimates of the metamagnetic field, H_M, become extremely difficult. However, following the trend of the data in figure 4.26, it is suggested that there is a continued presence of the metamagnetic boundary as the field approaches to zero, with the lack of power-law relations mentioned above indirectly supporting this assertion.

In summary, from the above data analysis it is concluded that at the composition $x = 0.27$, $La_{0.27}Ca_{0.73}MnO_3$ shows features characteristic of both continuous and

discontinuous transitions, and, within the experimental uncertainty, these two features are essentially coincident in (H_i –T) plane. This behaviour is fundamentally different from crossover effects for sequential second-order to first-order transition as $T \rightarrow T_c$, where the system approaches the ordering temperature, T_c, from below as a second-order phase transition, but this is interrupted by a weakly first-order transition to the paramagnetic state. In this situation the power-laws discussed above would be expected to occur as the transition is approached from higher reduced temperatures. Here these transitions are essentially coincident, as the *lack* of power-laws confirm. These results were the first to identify such simultaneous characteristics, although a recent report by Rivadulla et al. [98] shows some similarities. The latter studies show that the magnetic phase transition is suppressed close to the localized limit (i.e. $x \approx 0.2$ or $x \approx 0.5$), and no critical exponents can be extracted near these compositions. According to Rivadulla et al. the phase transition close to these compositions is not a true magnetic phase transition, but only a change in the relative volume fraction of the fluctuations that compete to develop below a certain temperature T_f (a crossover temperature, T_f , has been defined instead of T_c for these compositions). The proximity to the doping-induced metal-insulator transition which breaks up the electronic/magnetic homogeneity of the system can partially explain their results. The dual characteristics reported in the present studies may also attribute to this behaviour.

Obviously, the complex behaviour of this system near optimal doping is still unclear. The unusual dual characteristics seen in the magnetic critical response at $x = 0.27$ may extend to other compositions. Indeed, work on a single crystal with $x = 0.2$ is planned for the immediate future. The dual first and second order features first seen at $x = 0.27$ led to suggestion that this system might display an enhanced entropy change near T_c. This, however, was difficult to prove conclusively, but it did lead to the observations of the expected enhancement in the Ni-Mn-Ga system, discussed later in this thesis.

4.8 The Magnetic Properties of $(La_{1-x}Nd_x)_{0.67}Pb_{0.33}MnO_3$

4.8.1 Sample preparation

Samples of $(La_{1-x}Nd_x)_{0.67}Pb_{0.33}MnO_3$, with nominal composition, x = 0, 0.2, 0.4, 0.6, 0.8, 1.0, were prepared using standard solid state reaction techniques from high quality starting materials La_2O_3, Nd_2O_3, PbO and MnO_2. The procedure followed was: the samples were first preheated in air at 850 ^0C for 24 hours, then the products were ground, granulated and pressed into disks. These were subsequently sintered at 1100 ^0C for 48 hours in flowing air and then finally annealed at 950 ^0C for 48 hours and at 650 ^0C for 24 hours in flowing air. Room temperature x - ray diffraction data using Cu Kα radiation confirm that all samples are single phase. Specifically, $La_{0.67}Pb_{0.33}MnO_3$, one of the end members of this series of samples (x = 0), possesses a near cubic structure exhibiting a slight rhombohedral distortion with a = 3.8927Å and $\alpha = 90.30^0$; while the structure changes to an orthorhombic symmetry with a space group *Pnma* near x = 1, in agreement with literature reports [99-101]. The corresponding tolerance factor, t, evaluated using equation (4.2), decreases from 0.9915 to 0.9688 with increasing composition, x. Field dependent magnetization curves at various temperatures, M(H,T), and ac susceptibility measurements, $\chi(H,T)$, at 2.4 kHz and 30 mOe rms driving field, in both zero field and various static fields up to 80 kOe were carried out in a Quantum Design PPMS Model 6000

magnetometer on samples of approximate dimensions (7.0 X 1.5 X 0.5) mm^3. All fields are applied parallel to the longest specimen dimension.

4.8.2 General features

i) The zero – field susceptibility

Figure 4.27 shows the temperature dependent zero-field susceptibility, $\chi(0,T)$, (measured on warming following zero-field cooling) for all 6 samples. All of these curves display similar features, specifically, a magnetic phase transition from a high temperature paramagnetic state to a lower temperature ferromagnetic state. From the zero-field susceptibility curves, preliminary estimates for the magnetic ordering temperature, T_c, can be obtained by finding the minimum slope of such curves, i.e. $d\chi(0,T)/dT\big|_{Min}$. Generally speaking, these temperatures show good overall agreement with previous ordering temperature estimates for this system [52, 100-102], including single crystal samples [101, 102]; this indicates the high quality of the present samples. With increasing Nd doping level, the ordering temperature moves towards lower temperature; in particular, for the 6 samples here, the La-rich end member- $La_{0.67}Pb_{0.33}MnO_3$ – possesses the highest ordering temperature, T_c = 340.5 K, while $Nd_{0.67}Pb_{0.33}MnO_3$ (x = 1) has the lowest, T_c = 158.8 K. The magnetic response of these two end members will be first discussed in detail below. Compared

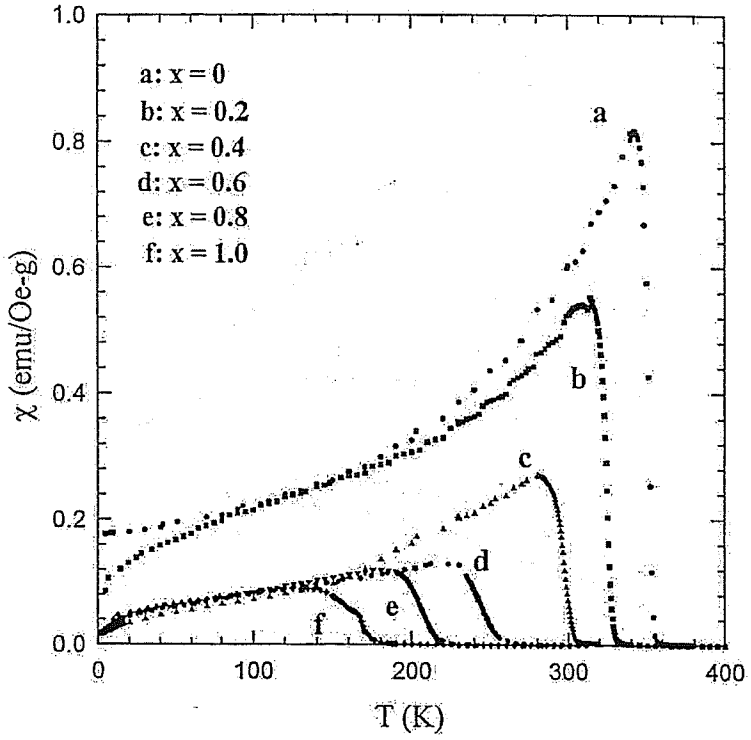

Figure 4.27 The zero-field ac susceptibility curves for all six samples measured on warming.

with numerous previous studies of the magnetic and magnetoresistive behaviour, those in [101] included only investigations on $La_{0.4}Nd_{0.3}Pb_{0.3}MnO_3$ and $La_{0.3}Nd_{0.4}Pb_{0.3}MnO_3$. By contrast, the present studies were performed on more comprehensive Nd substitutions.

ii) Low temperature magnetic moments

Magnetization isotherms at 4.2 K for all samples are shown in figure 4.28; a careful check of the high-field slope of such curves reveal similar features to those reported in [101] , namely, only $La_{0.67}Pb_{0.33}MnO_3$ (x = 0) achieves saturation just above a field of 20 kOe. The lack of saturation of all other samples can be followed up to 80 kOe. From these low temperature magnetization isotherms, the spontaneous magnetization $M_s(H=0,T=4.2K)$ and the saturation magnetization, $M_{sat}(H \to \infty, T = 4.2K)$, can be estimated. The former are found by extrapolating the high-field data (fields between 60 kOe and 80 kOe) to zero field (H=0); the latter are obtained by plotting the magnetization M versus 1/H. The magnetic moment, μ, per formula unit can be calculated using

$$\mu = MW / N_a \qquad (4.17)$$

with either the spontaneous magnetization or the saturation magnetization substituted for M; W is the molecular weight and N_a is Avogadro's number. Table 4.2 summarizes the spontaneous magnetization, Ms, the saturation magnetization, M_{sat}, and the value deduced for the magnetic moment per formula unit from M_s and M_{sat}. These experimental moments will be compared with the theoretical moments based on a full alignment spin-only assumption. It should be mentioned that two values of the Nd moment – 1.2 μ_B [103] and 1.5 μ_B [101]- have been used in various calculations. With increasing Nd substitution, the magnetic moment per formula unit also increases and all such moments for $0.2 \leq x \leq 1$ are significantly higher than a

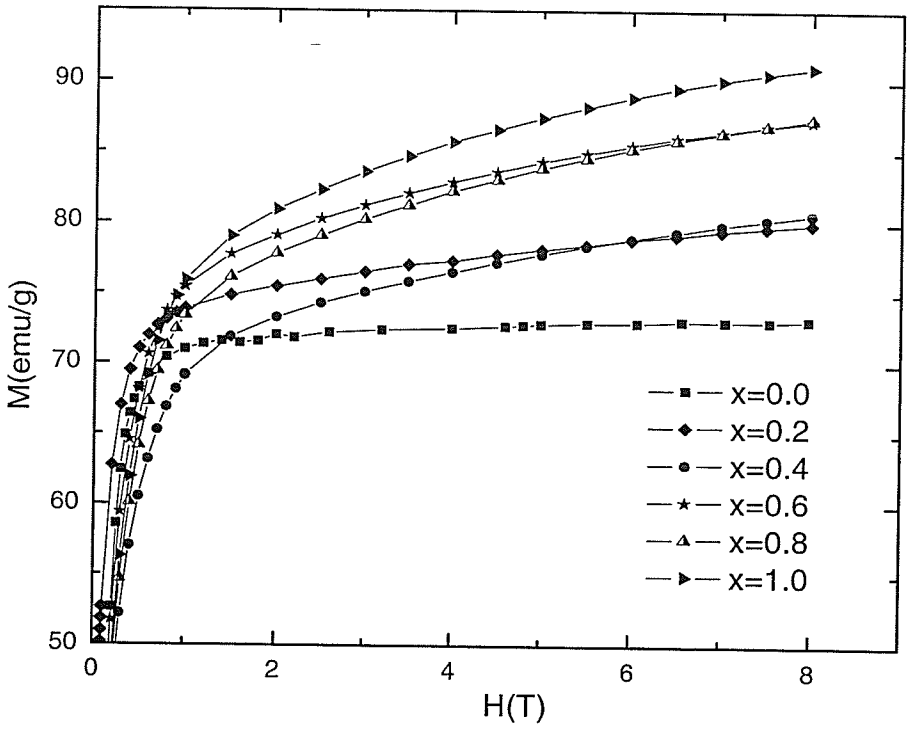

Figure 4.28 Magnetization isotherms at 4.2 K for all six samples.

spin-only value arising from collinear arrangement of Mn spins ($\mu = 0.67\ \mu_B$). This suggests that the Nd moment also contributes to the total moment of the system. However, the moments calculated from the spontaneous magnetization, Ms, are considerably lower than the spin-only value from a collinear arrangements of the Nd and Mn spins, as reported previously [101, 102]. This indicates that the Nd moment is not fully (ferromagnetically) aligned in the absence of a magnetic field. By

contrast, the saturation magnetic moment yields values much closer to the prediction of the total spin-only (Nd+Mn) moments.

Composition (x)	0	0.2	0.4	0.6	0.8	1.0
M_s (eum/g)	72.45	75.54	73.87	80.71	79.66	83.30
M_s (μ_B)	3.43	3.58	3.51	3.86	3.82	4.00
M_{Sat} (emu/g)	74.23	83.57	86.15	92.56	94.09	97.26
M_{Sat} (μ_B)	3.52	3.97	4.10	4.42	4.50	4.67
Mn (spin only)	3.67	3.67	3.67	3.67	3.67	3.67
Mn+Nd (~1.5μ_B)	3.67	3.87	4.07	4.27	4.47	4.67
Mn+Nd (~1.2μ_B)	3.67	3.83	3.99	4.15	4.29	4.47

Table 4.2 The upper panel: The values of the experimental spontaneous magnetization (M_s) and the deduced moment per formula unit, the experimental saturated magnetization (M_{Sat}) and the corresponding deduced moment; The lower panel: the maximum spin-only moments of Mn ions alone and for parallel alignment of Mn and Nd spins for all six samples. Note that the (Mn+Nd) moments are evaluated based on two different values of the moments of Nd.

4.8.3 The critical behaviour of $(La_{1-x}Nd_x)_{0.67}Pb_{0.33}MnO_3$

i) x = 0 and x =1

Figure 4.29 reproduces the ac susceptibility as a function of temperature, $\chi(H,T)$, at different static biasing fields for $Nd_{0.67}Pb_{0.33}MnO_3$ (x = 1). The effects of static biasing field from 1100 Oe to 3000 Oe superimposed on the ac driving field (0.03 Oe

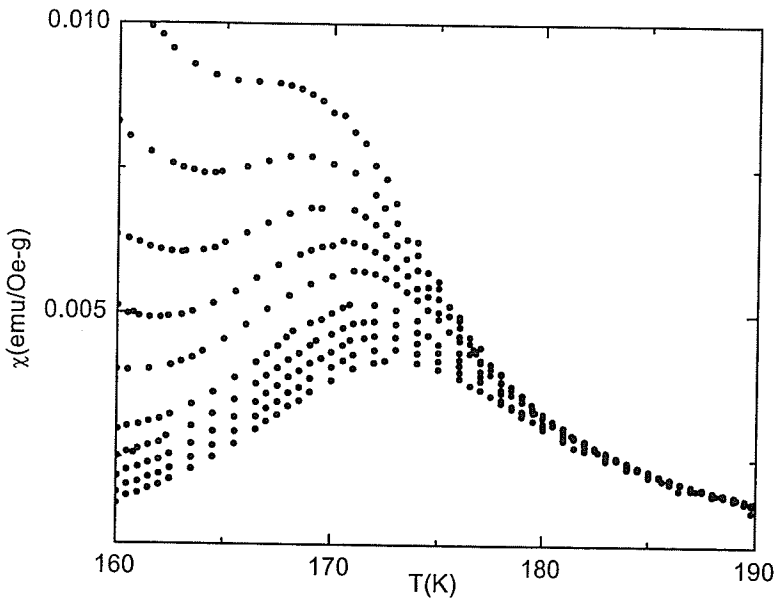

Figure 4.29 The temperature dependent ac susceptibility data at different static biasing fields of 1100 Oe (top) to 1900 Oe in 200 Oe steps and 2200 Oe to 3000 Oe (bottom) in 2000 Oe steps for $Nd_{0.67}Pb_{0.33}MnO_3$ (x = 1) sample.

at 2400 Hz) can be seen from this plot. Specifically, a large static biasing field suppresses the principle maximum, evident in the zero-field susceptibility curves (figure 4.27), and critical (secondary) maxima emerge; the latter decrease in amplitude and move upward in temperature with the increasing static field. As discussed in chapter 2, such secondary maxima are an important characteristic of a continuous /second-order phase transition. The locus of a secondary maximum delineates the crossover line, as discussed earlier. From these critical peaks a set of critical exponents (which are generally model-dependence) can be extracted based on various power-law relations (2.17), (2.21) – (2.23). A careful examination of figure

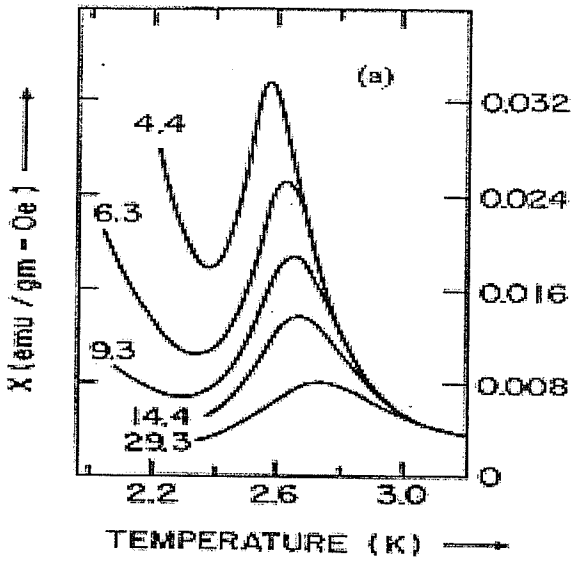

Figure 4.30 The field- and temperature-dependent ac susceptibility for Pd–1 at.% Mn plotted against temperature, with values of the corresponding static biasing fields marked against the appropriate curve

4.29 indicates that in lower static fields (<1400 Oe), these critical peaks are obscured by the technical/ non-critical components in the response, (i.e. components not saturated in low fields). Such technical contributions, if not effectively eliminated, will complicate the analysis of the true asymptotic behaviour (i.e. $h \to 0$ and $t \to 0$ [104]), thus raising uncertainties about the associated universality class.

In the present study, a new technique has been used in an attempt to eliminate such non-critical contributions in low static fields. This involves fitting the temperature dependent ac susceptibility curves, specifically in lower static fields, to a peak-finding non-linear function, such as a Gaussian or a Lorentzian function. In

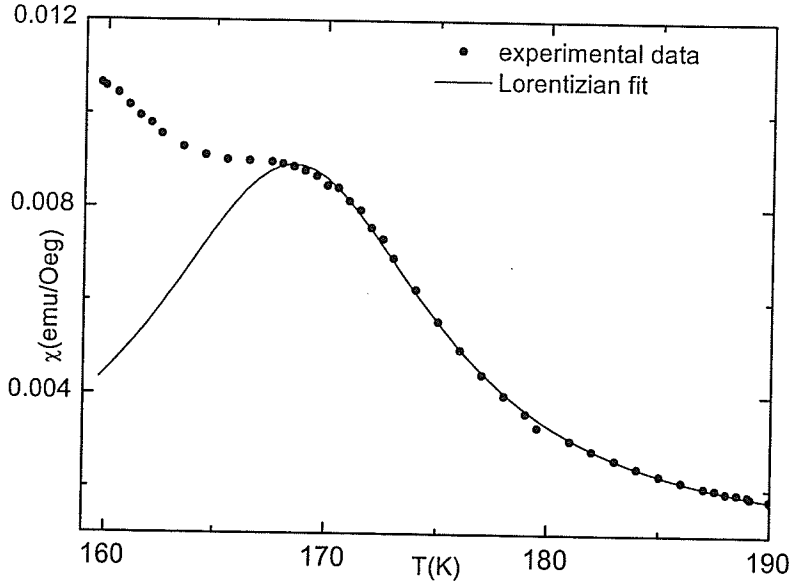

Figure 4.31 Dotted line: the temperature dependent ac susceptibility data at a static biasing field of 1100 Oe; Solid line: Lorentizan fit to the high temperature part in order to find the peak temperature.

practice, the low fields ac susceptibility data in this system have been fitted to hundred of peak-finding functions; Lorentzian fitting consistently yields the best result. Numerical simulation [105] indicates that the ac susceptibility should continue decreasing with decreasing temperature below the peak. Thus the upturn, evident in the low-temperature regime in figure 4.29, represents non-critical/ regular contributions. In fact, such monotonically decreasing features are displayed in several alloy systems, PdMn and PdFe for example. Figure 4.30 shows the field and temperature-dependent ac susceptibility for Pd-1 at.% Mn plotted against

temperature; values of the corresponding static biasing fields are marked against the appropriate curve [31]. In this system, the critical maxima were first resolved at fields as low as 4 Oe – more than two orders of magnitude lower than in the present sample – $Nd_{0.67}Pb_{0.33}MnO_3$. Indeed, in Pd-1.4% Fe [106] critical peaks emerge in applied fields below 1 Oe. The results of a peak locating procedure using a Lorentizian function on the present sample is shown in figure 4.31 for a static field of 1100 Oe, the data taken from figure 4.29. Since technical contributions become increasingly important at or below T_c, fits are initiated from the high temperature side of the peak, and the number of points fitted is increased until χ^2 is minimized*. The peak temperature, T_m, and the corresponding amplitude, χ_m, are then taken directly from this final fit.

The resulting critical peak temperatures, T_m, are plotted in figure 4.32(a) as a function of $H_i^{0.57}$ (H_i is the internal field); this plot serves as a test of equation (2.21), using 3D Heisenberg exponents values of $(\gamma+\beta)^{-1} = 0.57$. From this figure a more accurate estimate of the Curie temperature is obtained by fitting the data points and extrapolating to the zero internal field, yielding $T_c = 157.9 \pm 0.5$ K. Figure 4.32(b) plots the reduced temperature, $t_m = (T-T_c)/T_c$, against the internal field, H_i, on a double logarithmic scale, thus testing equation (2.22); a least square fit yields critical exponents $\gamma+\beta = 1.75 \pm 0.10$. Excellent self-consistency is found by comparing this

*χ^2 is the sum of the squares of the deviations of the theoretical curve(s) from the experimental points for a range of independent variables

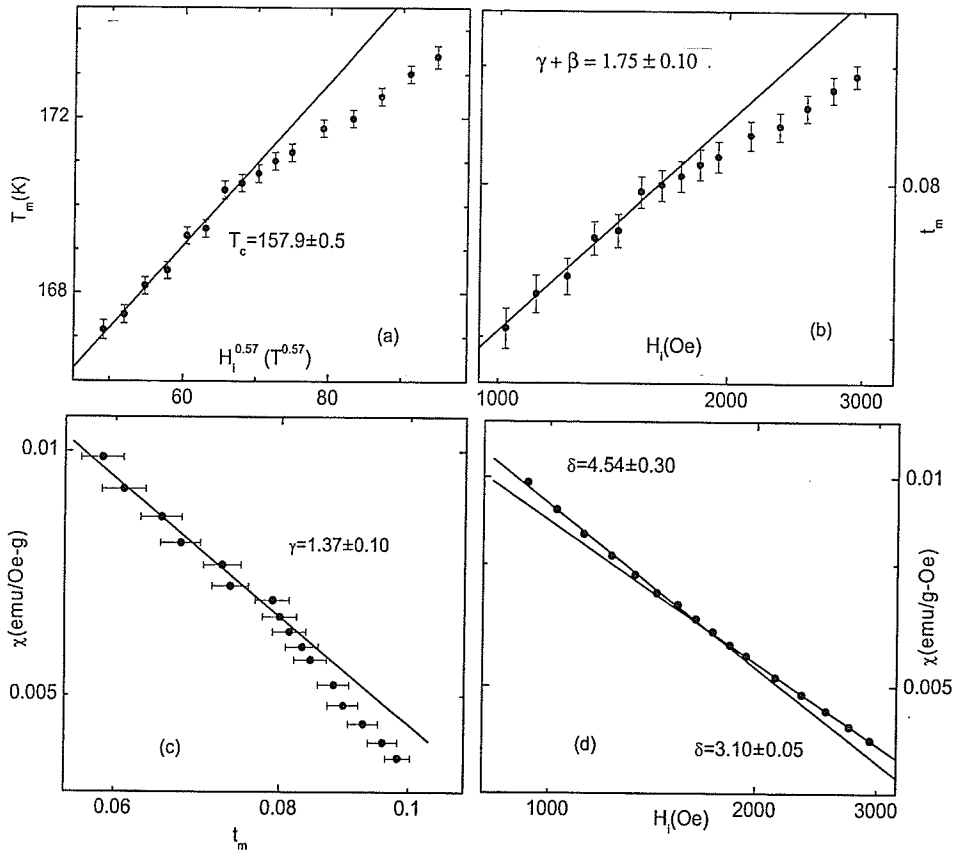

Figure 4.32 (a) The peak temperatures, T_m, plotted against $H_i^{0.57}$, the extrapolation of the low fields points to the zero internal field yield the Curie temperature; (b) the reduced temperature t_m against internal field H_i as a test of equation (2.23); (c) the susceptibility, χ_m, against reduced peak temperature, tm, as a test of equation (2.17); (d) the susceptibility maxima, χ_m, plotted against internal field H_i as a test of equation (2.23).

value with the exponents used in figure 4.32(a). Figure 4.32(c) shows the peak susceptibility, χ_m, plotted against the reduced peak temperature, t_m, on a log-log scale,

testing the power-law relationship, $\chi(h, t_m) \propto t_m^{-\gamma}$ (equation 2.17), describing the singular susceptibility. A least-square fit to the data in figure 4.32(c) yields a susceptibility exponent $\gamma = 1.37 \pm 0.10$ for $t_m < 0.08$. The equation of state exponent δ is estimated from a double-logarithmic plot of the peak susceptibility, χ_m, against the internal field, H_i, i.e. a test of the power law $\chi(h, t_m) \propto h^{1-\delta^{-1}}$. Fitting the low field points ($H_i < 1800$ Oe) yields $\delta = 4.54 \pm 0.30$, a value close to the predicted δ value from the 3D Heisenberg model ($\delta = 4.83$). For internal fields larger than 2 kOe, the δ value deviates towards the mean field value, $\delta = 3$. A similar crossover effect from 3D Heisenberg to mean field values of the exponent δ has been observed previously in the x = 0 member of this series; there it was attributed to the presence of "disorder". In the present context, this arises from a distribution of exchange coupling strengths (Mn^{3+} - Mn^{4+} double exchange, Mn^{3+} - Mn^{3+} superexchange, etc.), with model calculations confirming this trend [52]. In this same sample – $La_{0.67}Pb_{0.33}MnO_3$ – a set of exponents values- $\gamma = 1.39 \pm 0.06$, $\beta = 0.41 \pm 0.02$, $\delta = 4.20 \pm 0.15$ – have been extracted [52], using the same approach described above. These values are not consistent with the exponent values predicted by the 3D Heisenberg model; however, because of the presence of disorder, asymptotic 3D Heisenberg exponents cannot be excluded; the universality class for this system thus cannot be definitively identified. By contrast, critical analysis based on the temperature dependent ac susceptibility data on $Nd_{0.67}Pb_{0.33}MnO_3$ yields a set of low

field critical exponents - $\gamma = 1.37 \pm 0.10$, β = 0.380 ± 0.10, δ = 4.54 ± 0.30. These results are consistent with the critical exponents ($\gamma = 1.329 \pm 0.003$, β = 0.374 ± 0.006, δ = 4.54 ± 0.10) reported by Sahana et al. [107] in a single crystal of slightly lower composition using a more conventional analysis based on magnetization data. Both sets of results thus suggest that the 3D Heisenberg universality class governs the phase transition in $Nd_{0.67}Pb_{0.33}MnO_3$.

ii) x = 0.2, 0.4, 0.6 and 0.8

At intermediate compositions, disorder plays an increasingly important role. In addition to the disorder in the two end members mentioned above, at intermediate doping there is additional site disorder. At lower Nd substitution levels, x = 0.2 in particular, the influence of disorder is marked, and it significantly complicates the extraction of critical exponents from ac susceptibility data. Under these circumstances, the implementation of a Lorentz profile fitting procedure is particularly necessary to access low field data, i.e. data most relevant for assessing the asymptotic behaviour ($h \rightarrow 0, t \rightarrow 0$). In the following discussion, Lorentzian profile fitting has been widely implemented.

Figure 4.33(a) presents ac susceptibility data at different biasing fields for the x = 0.8 sample, along with critical analysis (figure 4.33(b)-(d)) based on equations (4.17), (4.21)-(4.23), yielding the Curie temperature, T_c = 203.1 ± 0.3 K, and critical

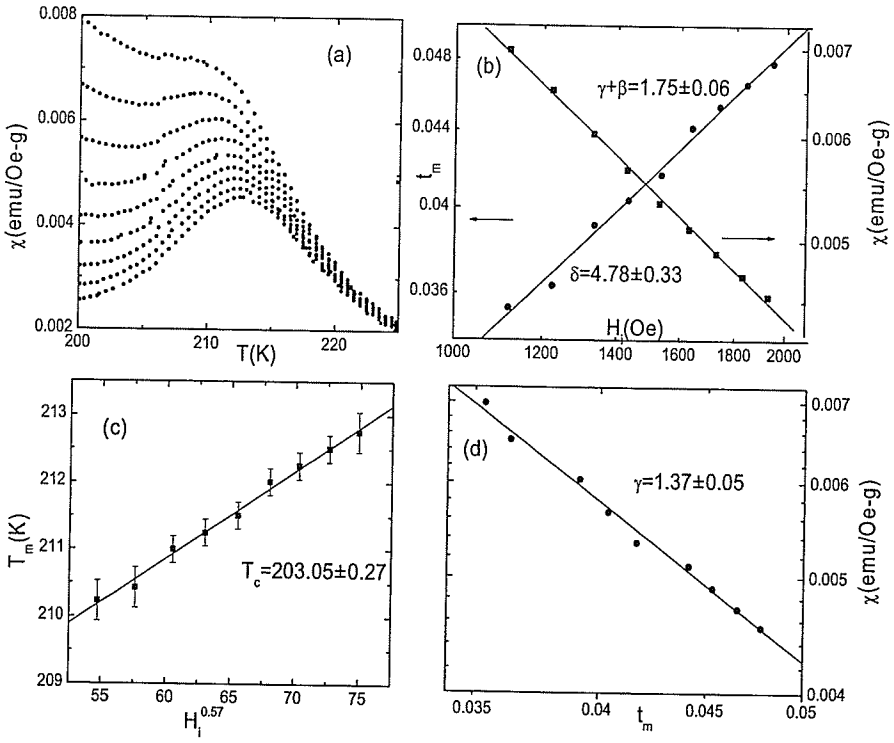

Figure 4.33 (a) Temperature variation of ac susceptibility at different static biasing fields of 1200 Oe to 2000 Oe in 100 Oe steps for x = 0.8 sample; (b) the internal field (H_i) versus peak susceptibility (right vertical axis); the reduced temperature (t_m) versus the internal field (H_i) (left vertical axis); (c) the reduced peak temperature plotted against $H_i^{0.57}$; (d) the peak susceptibility versus the reduced peak temperature

exponents, $\gamma = 1.37 \pm 0.05$, $\beta = 0.38 \pm 0.06$, $\delta = 4.78 \pm 0.33$. These values are again very close to those for the universality class of the 3D Heisenberg ferromagnet with short-range interactions. A similar critical analysis for the x = 0.4 sample is summarized in figure 4.34, from which $T_c = 295.8 \pm 0.3$ K, $\gamma = 1.14 \pm 0.05$, $\beta = 0.58 \pm 0.08$, $\delta = 3.03 \pm 0.19$ have been obtained. Clearly, the order parameter critical

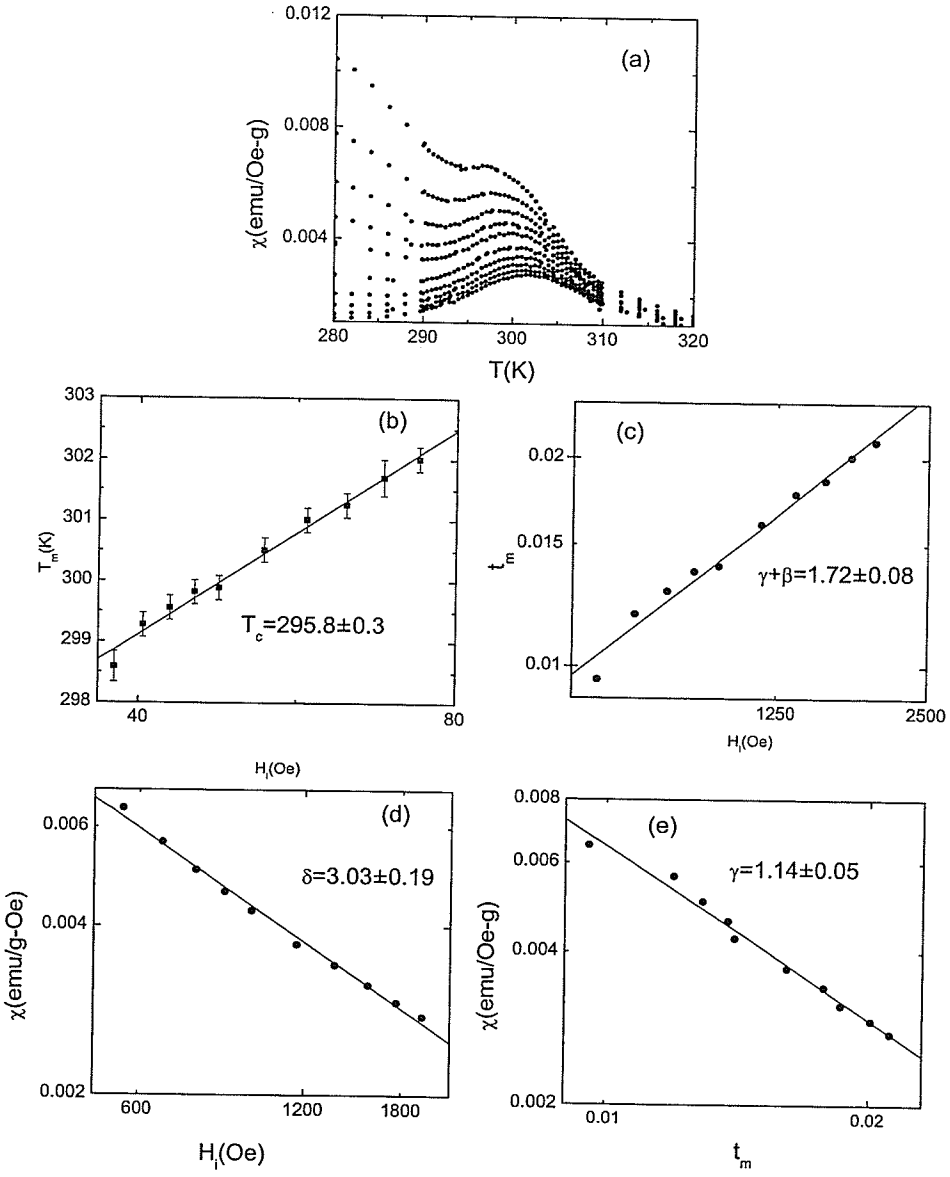

Figure 4.34 (a) The temperature dependent ac susceptibility in static fields of 600 Oe to 1000 Oe in 100 Oe steps, 1200 Oe to 2000 Oe in 200 Oe steps for the x = 0.4 sample; (b)-(e): plots extracting critical exponents for this sample.

Exponents	$\gamma+\beta$	δ	γ	Memo
Theoretical	1.75	4.8	1.386	3D Heisenberg
Theoretical	1.50	3.0	1.0	MFT
0.0	1.80 ± 0.06	4.20 ± 0.15	1.39 ± 0.06	3D Heisenberg?
0.2	1.46 ± 0.03	2.86 ± 0.08	0.95 ± 0.05	MFT
0.4	1.72 ± 0.08	3.03 ± 0.19	1.14 ± 0.05	Intermediate
0.6	1.79 ± 0.05	12.5 ± 4.69	1.59 ± 0.18	Intermediate
0.8	1.75 ± 0.06	4.78 ± 0.33	1.37 ± 0.05	3D Heisenberg
1.0	1.75 ± 0.10	4.54 ± 0.30	1.37 ± 0.10	3D Heisenberg

Table 4.3 Summary of critical exponents and critical exponent values; model prediction and measured values for all samples.

exponent, β, is much larger than any model prediction. The δ value, obtained in a manner which is independent of the choice for T_c, is close to the mean field theory prediction for this equation of state exponent. The susceptibility exponent, γ, falls between the predicted value from 3D Heisenberg and mean field theory. At very low Nd substitution levels (x = 0.2), similar critical analysis, based initially on 3D Heisenberg exponents, iterates towards a set of exponents which are much closer to the mean field exponent values. In order to carry out a self-consistent analysis, mean field exponent values were, therefore, used throughout for this sample. The major difference between these two fitting schemes is shown in figures 4.35(b) and (c), where the peak temperatures found from the temperature dependent ac susceptibility data (figure 4.35(a)) are plotted against the $H_i^{0.67}$ ($H_i^{1/\gamma+\beta}$ with $\gamma = 1$, $\beta = 0.5$) instead

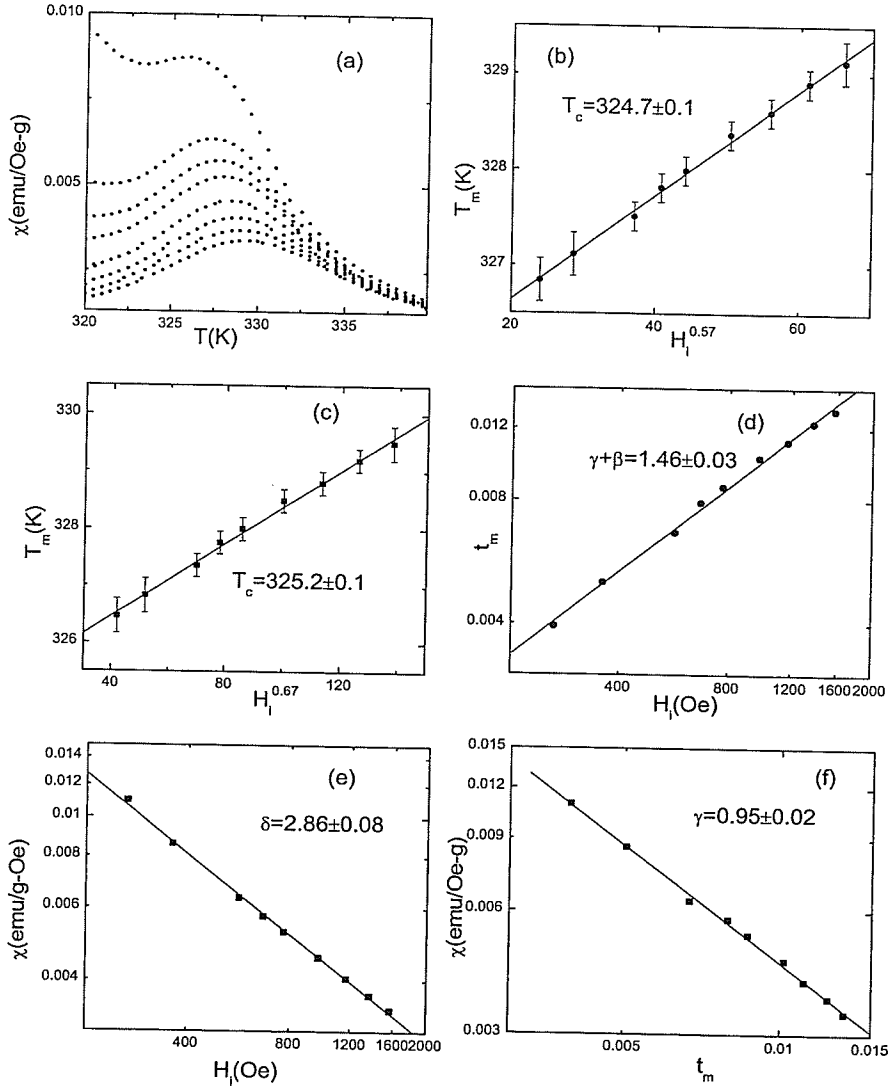

Figure 4.35 (a) The temperature dependent ac susceptibility at static biasing fields of 400 Oe (top), 600, 700, 800, 1000, 1200, 1400 and 1600 Oe (bottom) for the x = 0.2 sample; (b) The peak temperature found from (a) plotted against $H_i^{0.57}$ (using Heisenberg exponents); (c) The peak temperature (T_m) plotted against $H_i^{0.67}$ (using Mean field exponents); (d)-(f): plots to obtain the critical exponents based on T_c from (c).

of $H_i^{0.57}$ ($H_i^{1/\gamma+\beta}$ with $\gamma = 1.387$, $\beta = 0.365$). The plot with mean field exponents yields a slightly higher Curie temperature, $T_c = 325.2 \pm 0.1$ K. Obviously, the value of the Curie temperature will affect reduced temperature values, and correspondingly the values of γ and β. Based on this estimate for the Curie temperature, critical analysis in figure 4.35(d)-(f) yields $\gamma = 0.95 \pm 0.05$, $\beta = 0.51 \pm 0.03$, $\delta = 2.86 \pm 0.08$. Apart from the value for δ, which is marginally lower than the prediction of mean field exponents, the values of γ and β are consistent with the mean field prediction. Table 4.3 summarizes all the critical exponents for this series of samples and the two model predictions mentioned throughout the above discussion. Overall, the 3D Heisenberg critical exponent values found in the end member, $Nd_{0.67}Pb_{0.33}MnO_3$ (x = 1), appear to extend to the lower composition x = 0.8 sample as well. Unfortunately, the critical peaks for the x = 0.6 sample are very difficult to resolve, even fitting to a Lorentizian peak-finding function. Available peak temperature, T_m, and peak susceptibility, χ_m, obtained from the high biasing fields yield some unrealistic exponents, as table 4.3 shown. The mean field exponents found for the x = 0.2 sample may not necessarily indicate that the intrinsic spin interactions are long range since the disorder plays a very significant role in such samples; 3D Heisenberg exponents cannot be excluded since the true asymptotic behaviour is difficult to access.

As stated previously, disorder in this system plays a significant role in controlling the magnetic and transport properties and it is enhanced at intermediate doping level

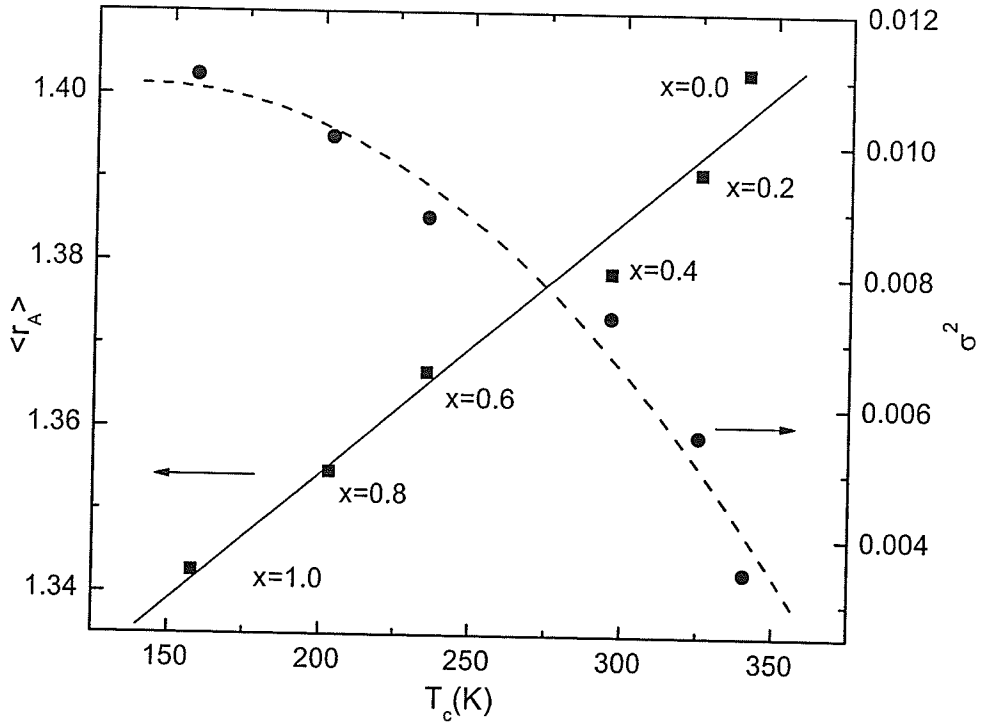

Figure 4.36 The average A site radius (<r_a>) versus T_c (left vertical axis); the solid line is a least-square fit to the data; the variance (σ^2) versus T_c (right vertical axis); the dotted line is a guide to the eyes.

by the further introduction of site disorder. Disorder is often described by the average A site radius <r_A> and its variance σ^2, which is the variance of the ionic radii r_i about <r_A>; it is defined [108] as $\sigma^2 = \sum y_i r_i^2 - \langle r_A \rangle^2$, where y_i represents for the fractional occupancies of the two or more constituents at the A site ($\sum y_i = 1$). Values for both <r_A> and σ^2 quoted in the following discussion are calculated based on the ionic radii provided by Shannon [49] for 12-fold coordination for the A sites

and 6-fold coordination for the B sites (i.e. taking r (La^{3+}) = 1.36Å, r(Nd^{3+})= 1.27 Å, r(Pb^{2+})= 1.49 Å, r(Mn^{3+}) = 0.645 Å, r(Mn^{4+}) = 0.53 Å and r(O^{2-}) = 1.40 Å). Previous studies on single crystal $La_{0.7-y}Nd_yPb_{0.3}MnO_3$ samples show that the average cation radius ($\langle r_A \rangle$) and cation size disorder (σ^2) have a marked influence on the magnetic properties due to the presence of significantly different cations (La and Nd) at the rare-earth site [102]. In figure 4.36, the Curie temperature (T_c), obtained from the critical analysis is plotted as a function of $\langle r_A \rangle$ and σ^2 for this series of samples. With increasing $\langle r_A \rangle$, the Curie temperature (T_c) increases almost linearly from 157.9 K (for x = 0) to 340.5 K (for x=1). Previous studies [52, 102] on the La-based manganites suggest that Pb-substituted samples exhibit one of the higher T_c's near optimal doping. In the present work, T_c = 340. 5 K was obtained in the x = 1 sample, close to that (T_c = 346 K) quoted more recently for a single crystal sample [102]. A least-square fit to the data in figure 4.36 yields $dT_c/d\langle r_A \rangle = 3254 \pm 257\,K/Å$. Clearly, since Nd possesses a smaller radius than La, the introduction of Nd in this system dramatically changes the average A site radius, $\langle r_A \rangle$, and lowers the Curie temperature, T_c. Decreasing $\langle r_A \rangle$ values causing decreases in T_c has been reported in $La_{0.7-x}Y_xCa_{0.3}MnO_3$ and $La_{0.7-y}Pr_yCa_{0.3}MnO_3$ which have fixed carrier concentration [109]. As far as the variance, σ^2, is concerned, T_c is inversely proportional to the variance, σ^2, as shown in figure 4.36 (right vertical axis). The variance (σ^2) influences both the magnetic and transport behaviour. Larger σ^2 values imply a higher degree of disorder, which significantly increases the

resistivity at lower temperature where site disorder enhances the localization of charge carriers. These latter studies will be detailed in the next subsection.

4.8.4 Conclusions

Detailed studies of the magnetic properties of $(La_{1-x}Nd_x)_{0.67}Pb_{0.33}MnO_3$ samples indicate that these samples are ferromagnets across the entire doping range. Critical analysis based on temperature dependent ac susceptibility data suggests that 3D Heisenberg exponents govern the phase transition in $Nd_{0.67}Pb_{0.33}MnO_3$ ($x = 1$) and the high Nd doping level samples ($x = 0.8$). The existence of disorder in the system complicates the extraction of critical exponents, particular at $x = 0.6$. In the $x = 0.2$ sample, a set of exponents close to the mean field prediction have been obtained. Preliminary studies reveal that the variation of the average cation radius $\langle r_A \rangle$ and the variance, σ^2, of these radii have significant impact on the magnetic properties of this series of samples.

4.9 Transport Behaviour in $(La_{1-x}Nd_x)_{0.67}Pb_{0.33}MnO_3$

4.9.1 General behaviour

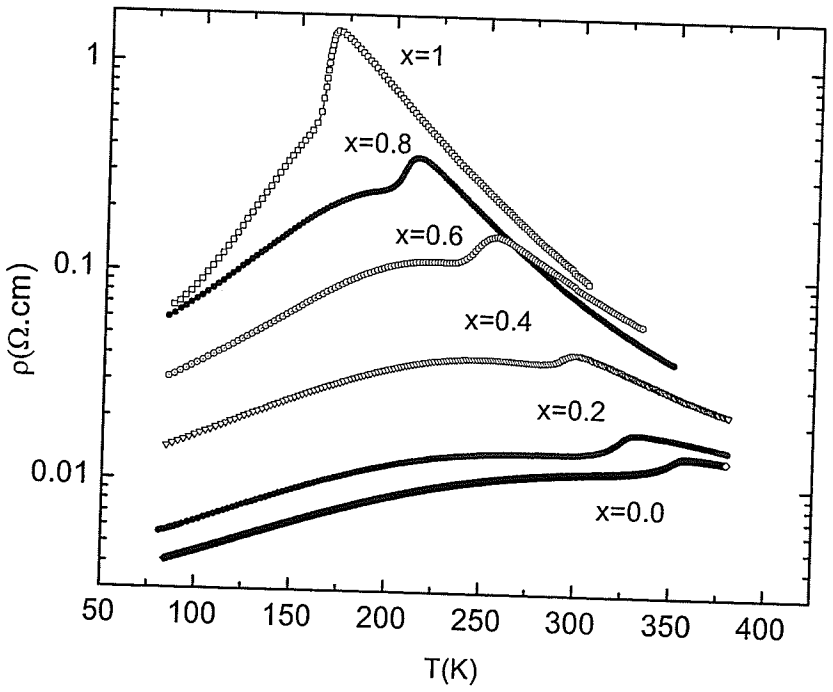

Figure 4.37 The temperature dependent resistivity data for all samples.

Figure 4.37 shows the resistivity as a function of temperature for this series of samples plotted on a semi-logarithmic scale. All samples exhibit a systematic transition from a metallic-like behaviour to a semiconductor-like behaviour with

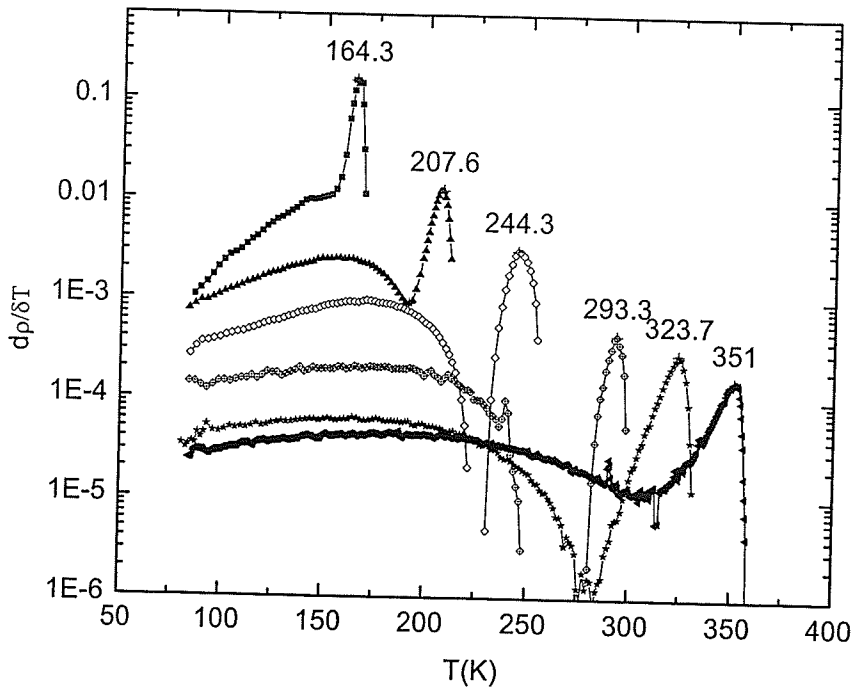

Figure 4.38 dρ/dT found from the data in figure 4.37 plotted against temperature for all 6 samples. The numerical values indicate the metal-insulator transition temperatures.

increasing temperature; this is quite similar to the transport measurement results reported in reference [109] for $La_{0.7-x}Pr_xCa_{0.3}MnO_3$ samples. Although the carrier concentration (Mn^{3+}/Mn^{4+}) is fixed, the magnitude of the peak resistivity monotonically increases with Nd content, which suggests that the magnetic Nd^{3+} ions provide an additional contribution to resistivity, likely due to enhanced magnetic scattering. From figure 4.37, the metal-insulator transition temperature, T_{MI}, can be obtained by finding the maxima of dρ/dT; figure 4.38 displays estimates for dρ/dT

found from the data in figure 4.37, while the metal-insulator transition temperature, T_{MI}, obtained from figure 4.38, are tabulated in table 4.4.

The magnetoresistance - an important parameter in the characterization of the CMR materials – is evaluated by comparing the temperature dependent resistivity data between zero-field and a specific applied magnetic field. Figure 4.39 shows typical resistivity curves for the x = 1 sample at zero field, 8 kOe and 16 kOe, respectively. Obviously, the application of a magnetic field strongly depresses the peak resistivity, and it also drives the peak resistivity towards a slightly higher

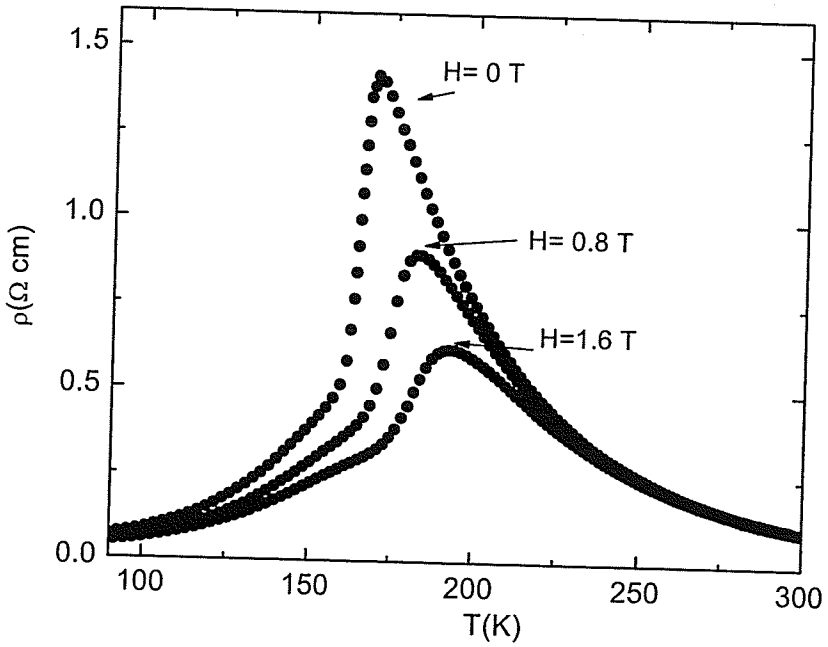

Figure 4.39 The resistivity as a function of temperature for $Nd_{0.67}Pb_{0.33}MnO_3$ at zero field (top), 8 kOe and 16 kOe .

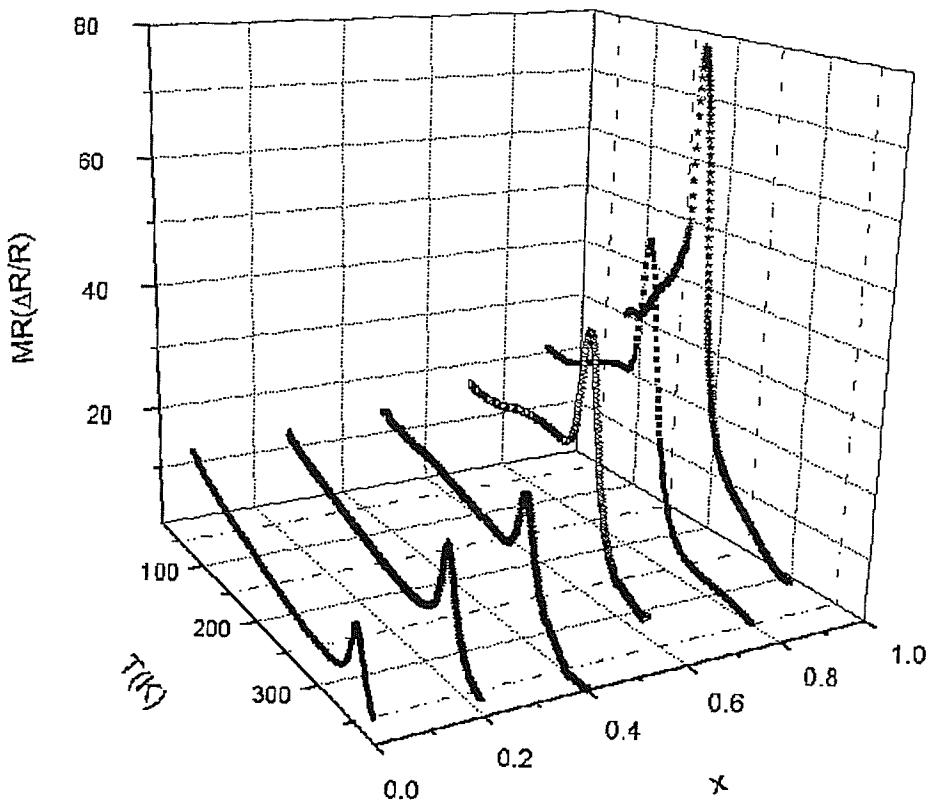

Figure 4.40 The thermal variation of magnetoresistance for samples with different doping levels.

temperature, which are the defining features described in the review chapter on CMR effects. Quantitatively, the magnetoresistance can be characterized using the equation

$$MR = \frac{\rho(H=0) - \rho(H=1.6T)}{\rho(H=0)} \times 100\% \qquad (4.18)$$

The magnetoresistance, estimated using this equation, is shown as a function of temperature for all samples in figure 4.40. The magnitude of the magnetoresistance decreases monotonically with both decreases in the Nd doping level and increasing

values of T_c (T_{MI}); the latter confirms a previous assertion about the doped manganites, i.e., the magnetoresistance near T_c is inversely proportional to T_c itself [110]. In particular, one of the end members of this series (x = 0), $La_{0.7}Pb_{0.3}MnO_3$, has the highest T_c and lowest magnetoresistance; by contrast, $La_{0.7}Nd_{0.33}MnO_3$

x	0.0	0.2	0.4	0.6	0.8	1.0
T_c (K)	340.5±0.3	325.2±0.1	295.8±0.3	235 ± 5	203.1±0.3	157.9±0.5
T_{MI}(K)	351.0±0.2	323.7±0.1	293.3±0.1	244.3±0.3	207.6±0.3	164.3±0.3
T_p(K)	355.0±0.2	328.0±0.3	298.5±0.1	253.0±0.4	212.0±0.2	163.5±0.1
ζ (Å)	N/A	7.687	3.326	2.405	1.859	1.833
$\langle r_A \rangle$	1.4029	1.39084	1.37878	1.36672	1.35466	1.3426
σ^2	0.00347	0.00556	0.00737	0.00888	0.0101	0.01103

Table 4.4 A summary of the values of the Nd doping level (x), the corresponding Curie temperature from the critical analysis (T_c), the metal-insulator transition temperature (T_{MI}), the temperature corresponding to the maximum magnetoresistance (T_p), the correlating length (ζ), the average A site radius ($<r_A>$) and the variance (σ^2).

possesses the lowest T_c and the highest magnetoresistance. The peak temperature, T_p, corresponding to the maximum magnetoresistance is found from figure 4.40 and recorded in table 4.4 for comparative purposes. Clearly from this table, the Curie temperatures, T_c, which are obtained from the critical analysis, are generally close to the metal – insulator transition temperatures, T_{MI}; such metal-insulator transitions

which essentially coincide with the ferromagnetic transition have been reported in manganites thin films, while the transport studies in such films show distinctive effects of small polaron transport [111]. Nevertheless, the concurrence of the magnetic phase transition and metal-insulator transition in this system suggests that the nature of the metal-insulator transition is magnetically driven. By contrast, the maxima in the magnetoresistance occur at a slightly higher temperature, T_p, as in most other systems.

4.9.2 Transport behaviour in the high temperature regime

i) x=0 and x=1

The transport mechanisms in doped manganites have been intensely studied, especially in high temperature regime of systems which undergo a metal-insulator phase transition. As reviewed previously, the high temperature transport behaviour can be described by either a pure temperature-activated (Arrhenius law) behaviour, a polaron model or a variable range hopping (VRH) model. [112] A brief introduction to these models will be given before the associated fitting processes are introduced.

1. Pure temperature-activated model (Arrhenius law)

The Arrhenius law has an exponential format, viz.

$$\rho = \rho_{\infty} \exp\left[\frac{E_g}{2kT}\right] \tag{4.19}$$

and is most often used to describe the activated behaviour in semiconductors arising from a band gap or a mobility edge. Obviously, the Arrhenius law is a phenomenological law containing two temperature-independent parameters - the activation energy, E_g, and the pre-exponential factor, ρ_{∞}. In fact, this law is only valid in those limited cases where the mobility or the carrier density has weak temperature dependence.

2. Polaronic model

Nearest-neighbour hopping of small polarons leads to a mobility with a thermally activated form. Depending on the speed of the charge-carrier and the frequency of the lattice vibrations, there are two limiting cases of the polaronic model. In the adiabatic regime the charge-carriers move faster than the lattice vibrations, and this leads to a resistivity of the form [111]

$$\rho = \frac{4\pi kT}{3ne^2a^2\omega_0} \exp\left(\frac{\left(E_p/2 - t\right)}{k_B T}\right) \tag{4.20}$$

where E_p is the polaron formation energy, n is the carrier density, t is the electronic transfer integral [113], ω_0 is an associated optical-phonon frequency, a is the hopping distance and e is the electron charge. In the non-adiabatic regime, the charge-carriers

move slowly compared to the lattice vibration, and the resistivity in this case can be expressed as: [111]

$$\rho = \frac{2\hbar k_B^{3/2}}{3ne^2a^2t^2}\left(\frac{2k_B}{\pi}\right)^{1/2} T^{3/2} \exp\left(\frac{E_p}{2k_B T}\right) \tag{4.21}$$

3. Variable range hopping model (VRH)

VRH was originally proposed by Mott [114] and describes the hopping transport in a system where the carriers are localized by random potential fluctuations and the

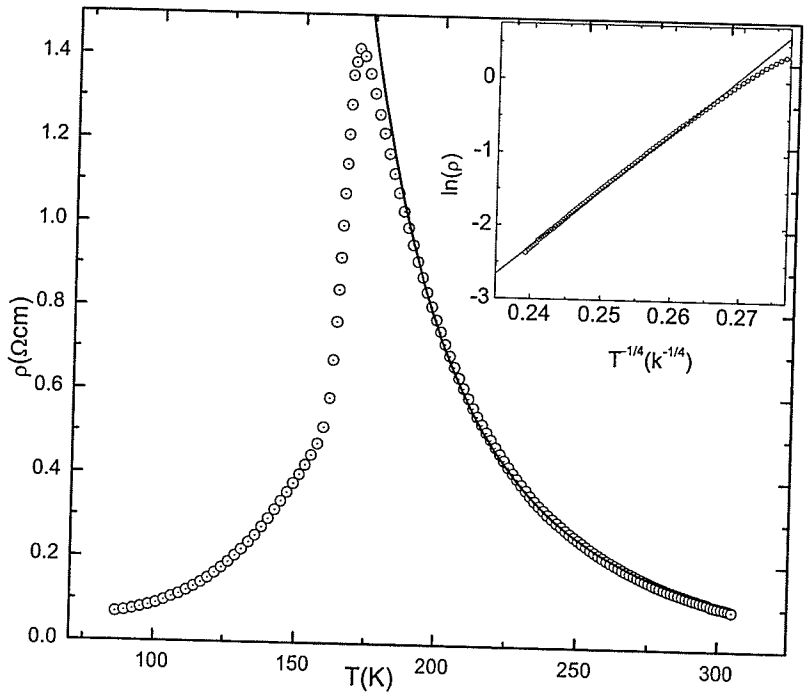

Figure 4.41 A VRH model fit for the high temperature regime of $Nd_{0.67}Pb_{0.33}MnO_3$; the inset: the high temperature resistivity replotted as $ln(\rho)$ versus $T^{-1/4}$.

preferred hopping is between sites lying within a certain range of energies. VRH leads to the following expression for the resistivity

$$\rho = \rho_{\infty} \exp\left(\frac{T_0}{T}\right)^{1/4} \tag{4.22}$$

where ρ_{∞} is a prefactor, which depends on the phonon density for this phonon-assisted conductivity, while T_0 is related to the localization length, ξ, and the density of states, N(E), via [115]

$$k_B T_0 = \frac{18}{N(E)\xi^3} \tag{4.23}$$

One of the end members of this series of samples, $Nd_{0.67}Pb_{0.33}MnO_3$, was first investigated here by fitting the temperature dependent resistivity data with the various model expressions mentioned above. The main body of figure 4.41 shows a fit to the VRH model for this sample. It should be mentioned that all plots, based on the four models mentioned, yield fits of roughly comparable quality over the same temperature range (see figure 4.42 for the detailed plots); however, a careful examination of the standard deviations (SD) indicates that the VRH model gives the best fit overall. However, the VRH model cannot be used throughout the entire high temperature regime; it deviates from the data below 183 K, about 15 K above the metal – insulator transition temperature. The inset in figure 4.41 replots these data in a $\ln(\rho)$ versus $T^{-1/4}$ format, this being a more "practical" way to test the applicability of the VRH model without losing accuracy [116]. From this fit, the prefactor, ρ_{∞},

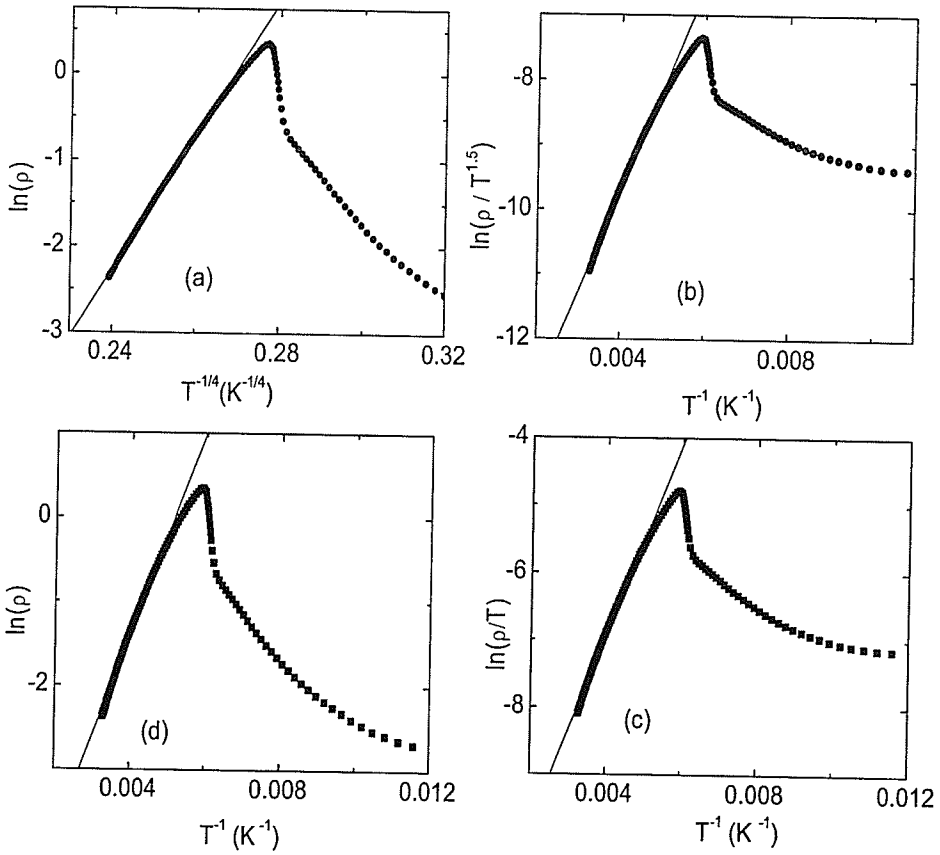

Figure 4.42 The high-temperature fit of resistivity data using (a) VRH model, (b) non-adiabatic polaronic model, (c) pure temperature-activated model and (d) adiabatic polaronic model for x = 1 sample. The corresponding standard deviations (SD) are (a) 0.01982, (b) 0.05699, (c) 0.06385, (d) 0.05108.

and the parameter, T_0, can also be calculated; furthermore the localization length, ξ, can be deduced based on equation (4.23). Prior to this, however, the electronic density of states (DOS), N(E), must be obtained. As discussed by various authors [50, 112], the value of N(E) is a crucial factor in order to get a realistic localization

length, ξ. For the present work, a reduced effective DOS derived by Viret et al. [112], $N(E) = 9\times10^{26}$ $m^{-3}eV^{-1}$, was adopted. Using this estimate, equation (4.23) yields a localization length $\xi = 1.84$ Å for the sample $Nd_{0.67}Pb_{0.33}MnO_3$ (x = 1). This value falls between the corresponding correlated length derived using the same method and N(E) for $(La_{0.7}Sr_{0.3})MnO_3$ and $(Pr_{0.7}Pb_{0.3})MnO_3$ respectively [117]. For the other end member, $La_{0.67}Pb_{0.33}MnO_3$, as the metal-insulator transition temperature is much higher, there is not sufficient high-temperature data available to perform a reliable fit.

As discussed previously, the VRH model was originally developed to deal with transport phenomena in doped semiconductors where the thermal energy is not sufficient to allow direct electron hopping to nearest neighbours. The most likely scenario in this case is that the electrons hop further to a location which has a smaller potential difference. Thus VRH is usually found in disordered systems, where conduction proceeds by hopping between randomly located sites with a distribution of allowed electronic energy levels. As far as the doped manganites are concerned, VRH conductivity behaviour is found predominately in bulk ceramics, $La_{1-x}Ca_xMnO_3$ ($0\leq x\leq0.15$) [116], optimally doped Ca manganites, $La_{0.7}Ca_{0.3}MnO_3$ [50, 117], and polycrystalline LCMO and LBMO film samples; however, in film samples this behaviour was attributed to extrinsic sources arising from nonstoichiometric regions or tunnelling processes across grain boundaries [111]. For $Nd_{0.67}Pb_{0.33}MnO_3$, in particular, the spin-spin disorder that has been observed contributes significantly to the VRH type hopping process found there. Nevertheless, the VRH model is only

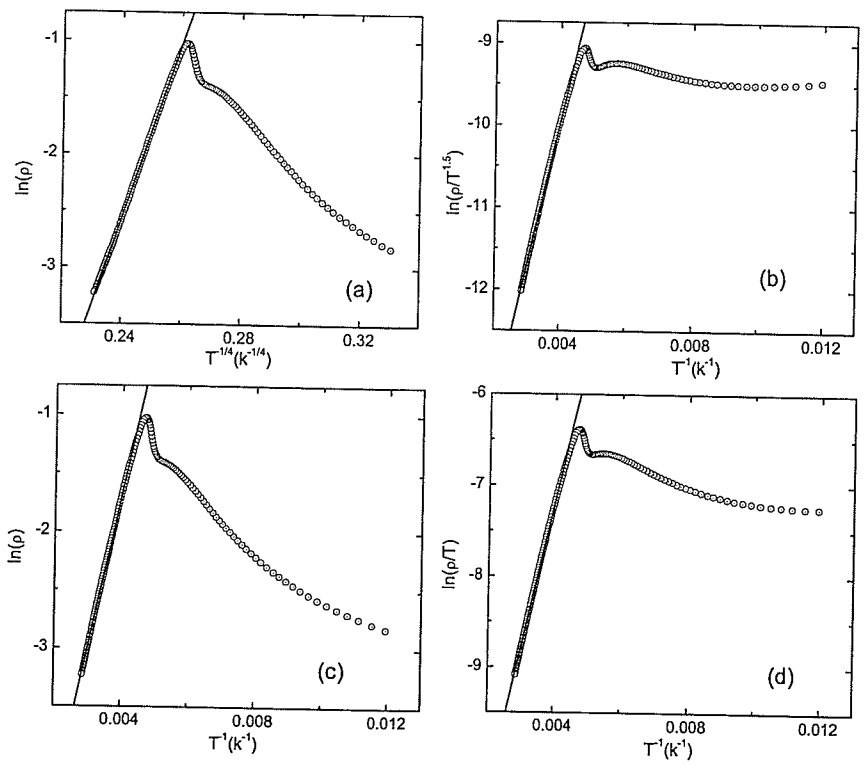

Figure 4.43 The high-temperature fit of resistivity data using (a) VRH model, (b) non-adiabatic polaronic model, (c) pure temperature-activated model and (d) adiabatic polaronic model.

applicable in a limited temperature range; hence the existence of other transport mechanisms cannot be excluded. In particular, when the temperature approaches the metal-insulator transition temperature, there is an obvious deviation from the VRH model predictions, which may arise from nearest-neighbour hopping contributions. At the intermediate doping level, the disorder in this system is enhanced by the appearance of site disorder, in addition to the spin disorder dominant in the end

members. From this point of view, a better VRH fit is expected in the intermediate doping samples than in the end members.

ii) **x = 0.2, 0.4, 0.6 and 0.8**

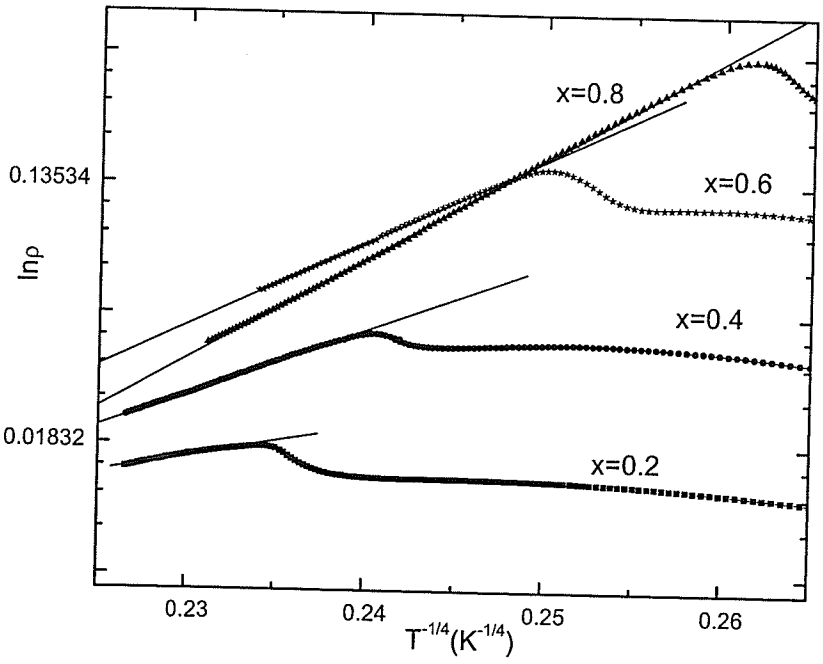

Figure 4.44 Resistivity data for samples x=0.8, 0.6, 0.4, 0.2 to test the VRH model.

Figure 4.43 shows fits using the four different models mentioned above for $(La_{0.2}Nd_{0.8})_{0.67}Pb_{0.33}MnO_3$ (x=0.8). An inspection of these fits, especially in the region immediately above the metal-insulator transition temperature, shows that this sample can be fitted remarkably well by the VRH model in comparison with other

models. Compared with fits for the end member (x=1.0) in figure 4.41, the temperature range fitted for this sample extended over a much wider temperature range, from 350 K down to the metal-insulator transition temperature, T_{MI}. The slope of the linear fit in figure 4.43(a) yields a localization length ξ = 1.86 Å. The same fitting procedure has been applied to all other samples with intermediate doping levels (x =0.6, 0.4, 0.2) and the VRH model consistently gives a better description of the high temperature transport behaviour; these graphs are not reproduced here, as they resemble figures 4.43(a)-(d) closely. Figure 4.44 summarizes the VRH model fits in a ln(ρ) versus $T^{-1/4}$ format for samples with x = 0.2, 0.4, 0.6, 0.8. The localization length, ζ, deduced from such fits, is summarized in table 4.4 for all samples. Generally speaking, with increasing Nd doping level in this system, the localization length, ζ, decreases. The close adherence to VRH behaviour in these intermediate doping level samples suggests that the high disorder present in them, namely, the contributions of spin and site disorder, provides a near-random distribution in electronic on-site energies [118].

4.9.3 The role of disorder in $(La_{1-x}Nd_x)_{0.67}Pb_{0.33}MnO_3$

As discussed previously, with the introduction of Nd into $La_{0.67}Pb_{0.33}MnO_3$, the disorder arising from size mismatch in this system plays a significant role in controlling the magnetic and transport properties. The size mismatch is characterized

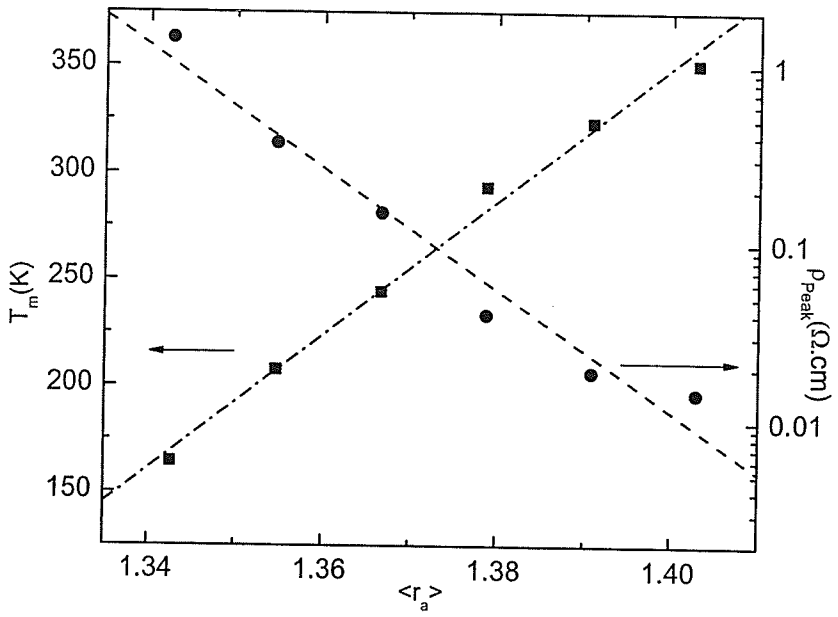

Figure 4.45 The average A site radius plotted against the metal- insulator transition temperature, T_{MI} (left vertical axis) and peak resistivity (semi-log scale, right vertical axis).

typically by the average A site radius, $\langle r_A \rangle$ and its variance, σ^2. Table 4.4 lists the average A site radius, $\langle r_A \rangle$, and variance, σ^2, evaluated using the above ionic radii for all specimens. Clearly, the average A site radius, $\langle r_A \rangle$, decreases monotonically with increasing Nd substitution, mainly because Nd^{3+} ions possess a smaller radius than La^{3+} ions; by contrast, the variance σ^2 increases with increased Nd substitution.

The metal-insulator transition temperature, T_{MI}, found from figure 4.38 as well as the peak resistivity, ρ_{peak}, is replotted as a function of A-site average radius $\langle r_A \rangle$ in figure 4.45. As is clearly evident from this figure, both the metal-insulator transition

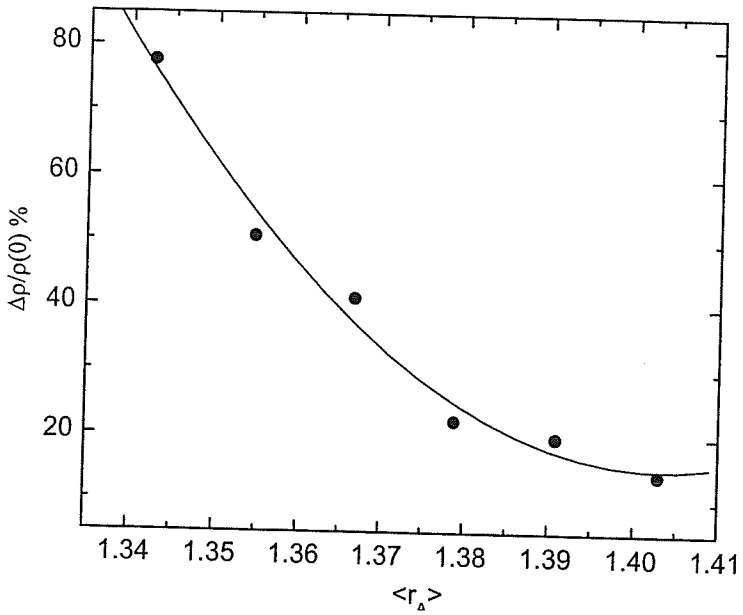

Figure 4.46 The maximum magnetoresistance versus average A site radius for all samples. The solid line is a guide for the eye.

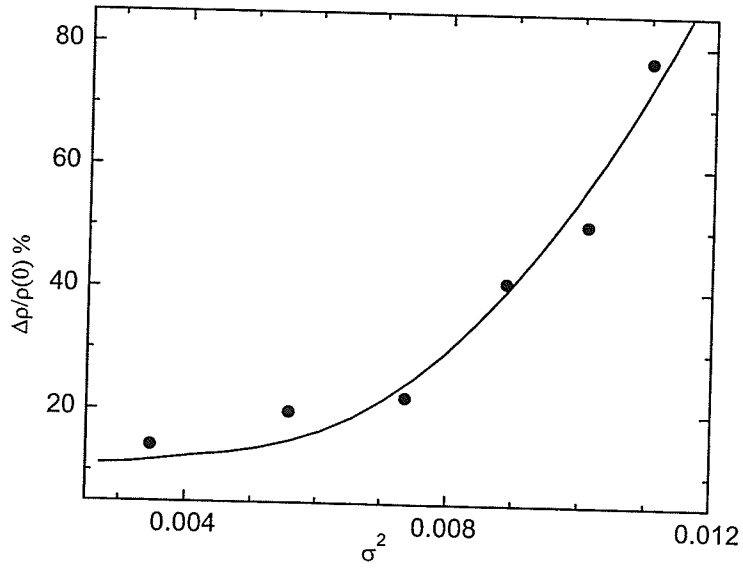

Figure 4.47 The maximum magnetoresistance versus variance for all samples. The solid line is a guide for the eye.

temperature, T_{MI}, and the peak resistivity, ρ_{peak}, are very sensitive to the average A-site radius, $\langle r_A \rangle$. Specifically, the metal-insulator transition temperature, T_{MI}, increases with increasing $\langle r_A \rangle$, which is consistent with that from other rare-earth element substitutions [10]. This suggests that the principal effect of increasing $\langle r_A \rangle$ is to increase the Mn-O-Mn band angle, thereby enhancing the matrix element, b, which describes electron hopping between Mn sites [109]. By contrast, the increase of $\langle r_A \rangle$ strongly depresses the peak resistivity ρ_{peak}. In particular, the relationship between T_{MI} and $\langle r_A \rangle$ is linear and a least-squares fit of the data points in figure 4.45 yields a slope of $dT_M / d\langle r_A \rangle = 3152 \pm 140 \mathrm{K/\AA}$. By contrast, the peak resistivity decreases exponentially with increasing $\langle r_A \rangle$.

The relationship between the maximum magnetoresistance $(\Delta R/R)_{Max}$ (found from figure 4.40) and $\langle r_A \rangle$ has also been explored. The maximum magnetoresistance $(\Delta R/R)_{Max}$ is inversely proportional to the average A site radius, $\langle r_A \rangle$, which is presented in figure 4.46. The focus here, however, is to investigate the relationship between the A site variance, σ^2, and the maximum magnetoresistance, $(\Delta R/R)_{Max}$, specifically, to reveal the impact of disorder on the magnetoresistance. This is accomplished in figure 4.47, where the maximum magnetoresistance is plotted against the variance, σ^2. Clearly, a larger variance, σ^2, that is, more disorder, favours the appearance of a larger magnetoresistance. Previous studies on various different A-site combinations suggested that the disorder at the A-sites does <u>not</u> favour the appearance of higher magnetoresistance. For example, $Pr_{0.7}Ca_{0.3}MnO_3$, where both

A-site ions have the same radius $\langle r_A \rangle$, so $\sigma^2 = 0$, has a higher MR than $La_{0.6}Y_{0.1}Ca_{0.3}MnO_3$ where the variance is about 0.0022. The measurement presented here provides an interesting counter example.

4.9.4 A preliminary study of the low temperature behaviour of $Nd_{0.67}Pb_{0.33}MnO_3$

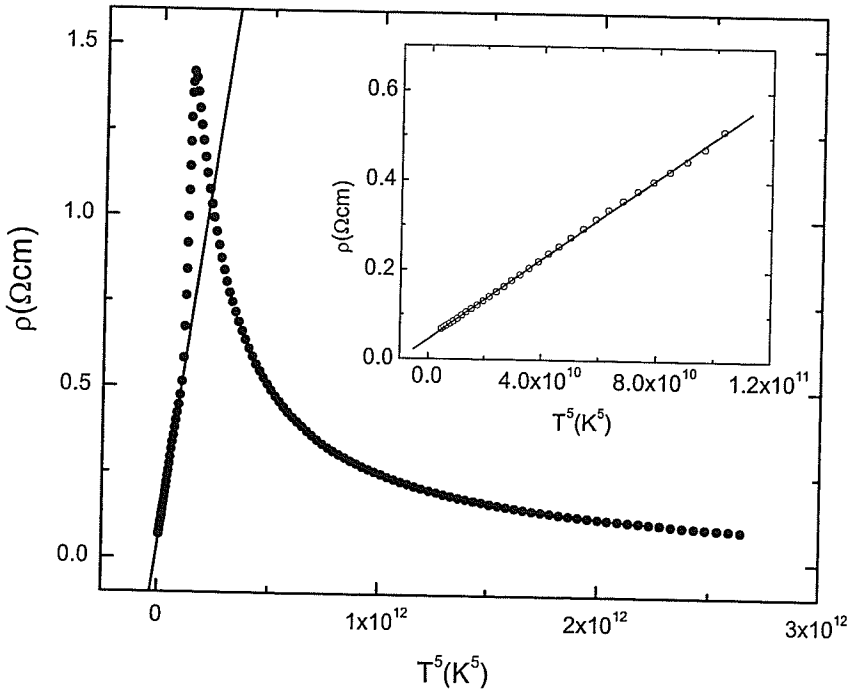

Figure 4.48 A fit to test the applicability of a T^5 dependence for $Nd_{0.67}Pb_{0.33}MnO_3$; the inset examines the low temperature regime.

The low temperature behaviour of the doped manganites usually follows the so-called Matthiessen's rule, i.e.

$$\rho(T) - \rho_0 = \rho_1 T^p \qquad (4.24)$$

where ρ_0 is the residual resistivity arising from scattering from impurities and defects; obviously, the inherent cation disorder in this system will lead to a larger ρ_0. The parameter p, describing the intrinsic scattering mechanism in the system, can be obtained by fitting the low temperature resistivity data. Previous studies in various systems suggest the parameter p in equation (4.24) can vary from 2 to 5 [2], which reflects different dominant scattering mechanisms, i.e. electron-electron, electron-magnon, electron-phonon. The low temperature resistivity data of the sample $Nd_{0.67}Pb_{0.33}MnO_3$ (x = 1) have been fitted using different p values. The best fit is shown in figure 4.48; a T^5 dependence in the inset of figure 4.48 suggests that the contribution from lattice scattering of charge carries, namely, the electron-phonon interaction, governs the transport behaviour in the low temperature regime for this sample. Similar studies have been applied to all other samples; however, none of them can be simply fitted to equation (4.24) by varying the p value. A more complicated fitting scheme with additional terms in equation (4.24) might be tried in order to reveal the scattering mechanism in the low temperature transport data, although this is a more complex procedure.

4.9.5 Conclusions

The specific feature accompanying Nd doping was an enhanced magnetoresistance accompanying an increased A-site variance. It would be interesting to investigate whether this relationship would be correlated with particular properties of the rare-earth element used in the substitution since the behaviour reported here appears to be an exception, rather than the rule.

In summary, studies of the transport behaviour of a series of $(La_{1-x}Nd_x)_{0.67}Pb_{0.33}MnO_3$ samples show a systematically behaviour in the metal-insulator transition; the transition temperatures keep decreasing with increases of the Nd doping level (x). Further analysis suggests a form of variable range hopping conduction predominates in the high temperature regime; in particular, the VRH model describes the intermediate doping level samples remarkably well. This may result from the disorder arising from both spin and site contributions in this doping regime, which produces the necessary distribution of allowed electronic energy levels.

Chapter 5

The Magnetocaloric Effect (MCE) in the Shape Memory Alloy Ni-Mn-Ga System

5.1 An Introduction to the Magnetocaloric Effect (MCE)

The Magnetocaloric Effect (MCE) is the entropy / adiabatic temperature change accompanying the application of an external magnetic field to magnetic materials. It was first discovered by Warburg [14] in 1881 and is an intrinsic property of all magnetic materials. When subjected to an external magnetic field, due to the coupling between the magnetic lattice and the field, the spins order and the magnetic entropy is lowered; with removal of the field, the spins become randomly orientated and the entropy increases, and this is accompanied by an adiabatic temperature decrease. The magnitude of the MCE is usually characterized by either the adiabatic temperature change, ΔT_{ad}, or the maximum magnetic entropy change, ΔS_m. The magnitude of the MCE strongly depends on the magnetic state of a sample. A disordered system (a paramagnetic system for example) usually displays a small entropy change. The entropy change can however be large for a material which

undergoes an order-disorder or an order-order phase transition. A very large entropy change, the so called Giant Magnetocaloric Effect (GMCE), was first found in the series $Gd_5(Si_xGe_{1-x})_4$ ($0 \leq x \leq 0.5$) [119], which show a entropy change at least twice large as that of pure Gd near room temperature, and 2-10 times larger than the best magnetocaloric materials with a conventional MCE. The discovery the GMCE became a strong driving force for room temperature refrigeration research. The following subsections begin with a review of the applications of the MCE in disordered systems (paramagnets) to achieve ultra-low temperature, then a summary of the GMCE materials studied in near room temperature is given and finally a simple description of a room temperature magnetic refrigerator is provided.

5.2 The Thermodynamic Theory of the MCE

The Gibbs free energy/thermodynamic potential, F, is defined as

$$F = E - TS \tag{5.1}$$

where the enthalpy E in a magnetic system is given by

$$E = U - HM \tag{5.2}$$

S is the total entropy. For a strongly correlated magnetic system, for instance manganites or the ferromagnetic shape memory alloy Ni-Mn-Ga system, this total entropy S can be separated into three components, viz.

$$S(T,H,p) = S_l(T,H,p) + S_e(T,H,p) + S_m(T,H,p) \tag{5.3}$$

where $S_l(T,H,p)$ is the entropy from lattice vibrations or distortions, $S_e(T,H,p)$ is the entropy from electrons, and $S_m(T,H,p)$ is the entropy from magnetic moments themselves. All three components depend on temperature, T, magnetic field, H, and pressure, p, however the magnetic entropy $S_m(T,H,p)$ shows a much strong field dependence than the other two.

From equations (5.1) and (5.2), the free energy F can be rewritten as

$$F = U - TS - HM \tag{5.3}$$

Combining with $dU = TdS + HdM$, yields

$$dF = -MdH - SdT \tag{5.4}$$

Equation (5.4) enables some important relationships to be deduced. First, the magnetization is

$$M = -\left(\frac{\partial F}{\partial H}\right)_T \tag{5.5}$$

$$\text{And } \left(\frac{\partial M}{\partial T}\right)_H = \left(\frac{\partial S}{\partial H}\right)_T \tag{5.6}$$

Equation (5.5) together with

$$\left(\frac{\partial T}{\partial M}\right)_S = \left(\frac{\partial H}{\partial S}\right)_T \tag{5.7}$$

$$\left(\frac{\partial T}{\partial H}\right)_S = -\left(\frac{\partial M}{\partial S}\right)_H \tag{5.8}$$

$$\left(\frac{\partial H}{\partial T}\right)_M = -\left(\frac{\partial S}{\partial M}\right)_T \tag{5.9}$$

are known as the Maxwell relations.

From eqn (5.6), the isothermal magnetic entropy change resulting from a field change can be evaluated from the integral

$$\Delta S_m(T,H) = S_m(T,H) - S_m(T,0) = \int_{H_i}^{H_f} \left(\frac{\partial M}{\partial T}\right)_H dH \qquad (5.10)$$

It is immediately evident that a larger rate of change of the magnetization with respect to the temperature, T, at a constant field, H, results in a larger isothermal magnetic entropy change. Using this relation, the isothermal magnetic entropy change can be evaluated directly from the experimentally measured magnetization isotherms.

The entropy S is also a function of temperature T and field H, so

$$TdS = T\left(\frac{\partial S}{\partial T}\right)_H dT + T\left(\frac{\partial S}{\partial H}\right)_T dH \qquad (5.11)$$

Considering the specific heat at constant field

$$C_H = \left(\frac{\partial E}{\partial T}\right)_H = T\left(\frac{\partial S}{\partial T}\right)_H \qquad (5.12)$$

and the Maxwell relation (5.7), then

$$TdS = C_H dT + T\left(\frac{\partial M}{\partial T}\right)_H dH \qquad (5.13)$$

For an adiabatic process with a zero entropy change

$$dT = -\frac{T}{C_H}\left(\frac{\partial M}{\partial T}\right)_H dH \qquad (5.13)$$

and for a finite process,

$$\Delta T = -\frac{T}{C_H}\left(\frac{\partial M}{\partial T}\right)_H \Delta H = -\frac{T}{C_H}\Delta S(T, \Delta H) \tag{5.15}$$

This is the theoretical basis for adiabatic demagnetization. For paramagnetic material, $(dM/dT)_H$ is usually negative, so decreasing the field will cool the materials. An important application of this relation is in the production of the extremely low temperature, as described later.

The integral form of equation (5.14) provides the adiabatic temperature change:

$$\Delta T_{ad} = -\int_{H_1}^{H_2} \frac{T}{C_H}\left(\frac{\partial M}{\partial T}\right)_H dH \tag{5.16}$$

Obviously, the adiabatic temperature change is also proportional to the rate of change of magnetization with respect to temperature, and is inversely proportional to the specific heat at constant field. In practice, both the isothermal magnetic entropy change (5.10) and the adiabatic temperature change (5.16) are used to characterize the behaviour of the MCE.

5.3 MCE in Paramagnets

Since the discovery of the MCE in 1881, much effort has been made to apply the effect. The most important application is magnetic refrigeration. Generally speaking,

magnetic refrigeration studies focus on two temperature ranges - ultralow temperature and (near) room temperature

The first successful application of MCE was adiabatic demagnetization, which used MCE to achieve extremely low temperature. Following Debye and Gianque's proposal in 1926, Giauque and Mardougall [15] made use of the low-temperature magnetocaloric properties of paramagnetic $Gd_2(SO_4)_3.8H_2O$ to achieve a temperature below 1K; specifically, they reached 0.53 K, 0.34 K and 0.25 K starting at 3.4 K, 2.0K and 1.5 K respectively. Following this pioneering work, other paramagnetic salts were used [120, 121]. Because of the low thermal conductivity and high lattice heat capacity of these salts as refrigerants, more recently, alloys such as $PrNi_5$ were studied and utilized in nuclear magnetic demagnetization experiments [122]. The thermodynamic background for adiabatic demagnetization will be introduced in a subsequent section.

To achieve extremely low temperatures using adiabatic demagnetization represents the principle use of the MCE in paramagnets. Other MCE studies, from low to room temperature, often involve the study of phase transitions - 1st order or 2nd order or both, since phase transitions around a critical temperature usually lead to a large $\left|(\partial M/\partial T)_H\right|$ which contributes to a large entropy change. However, unlike the use of the MCE at extremely low temperatures (which can provide a platform for studies near absolute zero) or the (near) room temperature range (which has potential application in magnetic refrigeration), low (10-80K) and intermediate temperature

(80-250K) range MCE studies have drawn less attention over the past several decades. Most recent research activities have been focused on the (near) room temperature MCE, especially for GMCE.

5.4 Room Temperature GMCE Materials and Magnetic Refrigeration

5.4.1 GMCE studies near room temperature

From the theoretical discussion of the MCE, a large $\left|(\partial M/\partial T)_H\right|$ is a key factor in achieving a larger entropy change. An ideal first-order phase transition, as discussed in chapter 2, should have an infinite $\left|(\partial M/\partial T)_H\right|$, which in turn should lead to an extremely large entropy change. This identifies a direction for seeking new materials with a larger MCE. The first such attempt was in the FeRh system [123] which undergoes a first-order phase transition from an antiferromagnetic to a ferromagnetic state, showing a giant MCE with an adiabatic temperature change of about 13K under a 2 T field. Unfortunately, the MCE in the FeRh system is irreversible and appears only once, rendering it impractical for application in continuous magnetic refrigeration. A breakthrough in MCE studies near room temperature was provided with the discovery a Giant MCE in the $Gd_5(Si_xGe_{1-x})_4$ system [16, 119]. In this

system, with $0 \leq x \leq 0.5$, the MCE is twice as large as the entropy change in pure Gd. Moreover, the temperature corresponding to the largest entropy change can be tuned between 20 and 336 K by varying the Si to Ge ratio in this compound; unlike the FeRh system, the GMCE in $Gd_5(Si_xGe_{1-x})_4$ is reversible. Further studies on $Gd_5Ge_2Si_2$ showed that the hysteretic loss (which makes magnetic refrigeration less efficient) can be reduced (more than 90%) by the addition of a small amount of iron. At the same time, the magnetic entropy peak moves from 275K to 305K and the width increases [124]. All these properties make $Gd_5(Si_xGe_{1-x})_4$ a promising candidate for magnetic refrigeration. The mechanism underlying the different magnetic behaviour in these two systems is still unclear; however Gschneidner et al. [125] stated that the difference probably arises from the different nature of the first-order phase transition. In the FeRh system, it is an order-order phase transition; in the $Gd_5(Si_xGe_{1-x})_4$ system, it's an order-disorder transition coincident with a structural phase change.

Subsequently, considerable effort has been devoted to investigate other systems which undergo a first-order phase transition, and among the dozen or so such systems, three draw particular attention. They are $MnAs_{1-x}Sb_x$, $MnFeP_{1-x}As_x$ and Ni-Mn-Ga, which will be reviewed separately.

Polycrystalline samples of $MnFeP_{1-x}As_x$ with $0.25 \leq x \leq 0.65$ were first studied by Tegus et al [17]. This system exhibits a field-induced phase transition; at low field, there is a sharp phase transition from ferromagnet to paramagnet accompanied by a

large entropy change. An entropy change of about 20 J/kg.K near x = 0.45 for a field change of 2 T and a change of 33 J/kg K for x = 0.35 under 50 kOe were found. It is worth mentioning that this system shows a larger refrigerant capacity (the refrigerant capacity measures how much heat can be transferred between the hot and cold reservoirs in one single ideal refrigeration cycle) than Gd-Ge-Si or pure Gd. This favours its use as a refrigerant. The origin of the GMCE is also unclear, as in the Gd-Ge-Si system. A preliminary study showed that the $MnFeP_{1-x}As_x$ system is an itinerant-electron system with a strong electron correlation. By contrast, Gd-Ge-Si is a localized-moment system with an indirect RKKY exchange interaction.

Additionally, $MnAs_{1-x}Sb_x$ [126], was studied with the intent to reduce thermal hysteresis of the MnAs system, which also showed a giant MCE [127]. Calculations based on the magnetization isotherms in this system with $0 \leq x \leq 0.4$ indicated a large entropy change of 25-30 J/kg K in a 50 kOe field. The largest entropy change appears at the Curie temperature with a field-induced paramagnetic to ferromagnetic phase change. Importantly, this peak temperature can be tuned between 230K and 315K without significant reduction of the MCE, and no hysteresis was observed for compositions above 0.05. Although the large MCE in this system originates from a field induced metamagnetic phase transition, just as the $MnFeP_{1-x}As_x$ system, the magnetic behaviour is quite different from that of an itinerant-electron metamagnetic system. The mechanism underlying the MCE is also different. A large

magnetovolume coupling in this system is a possible origin of the abnormal magnetization curves, and consequently, the giant MCE [128].

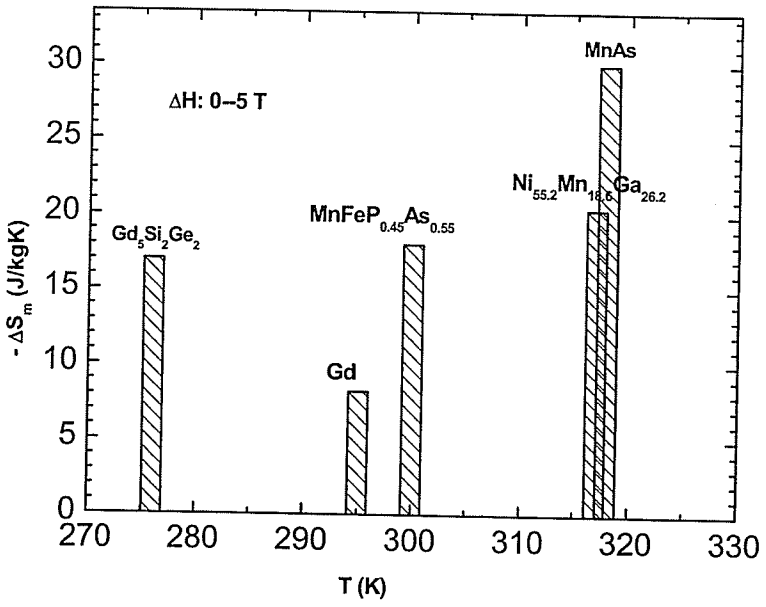

Figure 5.1 Summary of the maximum magnetic entropy change observed in several systems showing a GMCE with the corresponding peak operational temperature.

In 2001, Hu et al. [129] reported a large entropy change in the Heusler alloy Ni-Mn-Ga system. The entropy calculation for a single crystal alloy $Ni_{52.6}Mn_{23.1}Ga_{24.3}$ sample gave a large change of 18 J/kgK at 50 kOe near the martensitic structural transition temperature of 300 K. The parent Heusler alloy, Ni_2MnGa, has a first-order magnetic transition accompanying a cubic to tetragonal structural phase change at lower temperature T_m = 200 K, and a second – order paramagnetic to ferromagnetic

phase transition at T_c=376 K; it thus provides a natural platform to study the relationship between the MCE and the order of the phase transition. Detailed studies presented below on this system show that the entropy change can be further enhanced by the coincidence of the first-order transition with the second-order phase transition through compositional tuning. An entropy change as large as 20.4 J/kg K at 317K in a field of 50 kOe was reported in this system by Zhou et al. [130]. The relationship between the maximum entropy change and the peak operational temperature for the different systems mentioned above is summarized in figure 5.1.

5.4.2 Applications of GMCE- Magnetic Refrigeration

Magnetic refrigeration is a method of refrigeration based on the MCE. Figure 5.2 is schematic diagram for a magnetic refrigeration cycle. Similar to the Carnot cycle, it has four steps, namely magnetizing, heat absorption by the MCE material, demagnetizing and finally heat flow from a hotter to a colder sink. As early as 1976, Brown [131] proposed a prototype for a room temperature magnetic refrigerator. However, after the discovery of the giant MCE in many systems, magnetic refrigeration studies were giving a significant boost. In 1997, a joint report from two groups (Ames Laboratory and the Astronautics Corporation of American) demonstrated that magnetic refrigeration is a viable technology for (near) room

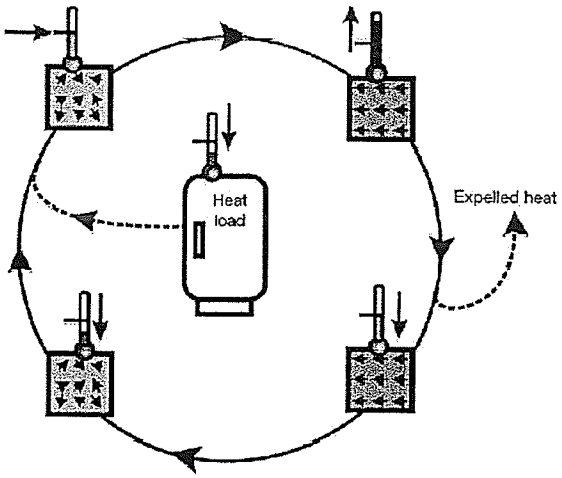

Figure 5.2 Schematic representation of a magnetic-refrigeration cycle in which heat is transported from the heat load to its surroundings. Initially randomly distributed magnetic moments are aligned by a magnetic field, resulting in heating of the material. This heat is removed from the material to its surroundings by a heat – transfer medium. On removing the field, the magnetic moments randomize, which leads to cooling of the magnetic material to below the ambient temperature [124].

temperature applications, including large scale building air conditioning, refrigerator and supermarket chillers. In 1997, Zimm et al. [132] successfully designed a proof-of-principle AMR (active magnetic regenerator). Figure 5.3 is schematic drawing of this proof-of-principle magnetic refrigerator. The system uses two beds containing a spherically shaped powder of Gadolinium which is quickly moved in and out of a magnet by a pneumatic drive. The beds are heated quickly when they are magnetized and cooled quickly when they are demagnetized. The heat transfer fluid (water here) is alternatively heated and cooled as it passes the beds. The transfer fluid then flows through the exchanger to complete the cycle. With a 50 kOe field (provided by a

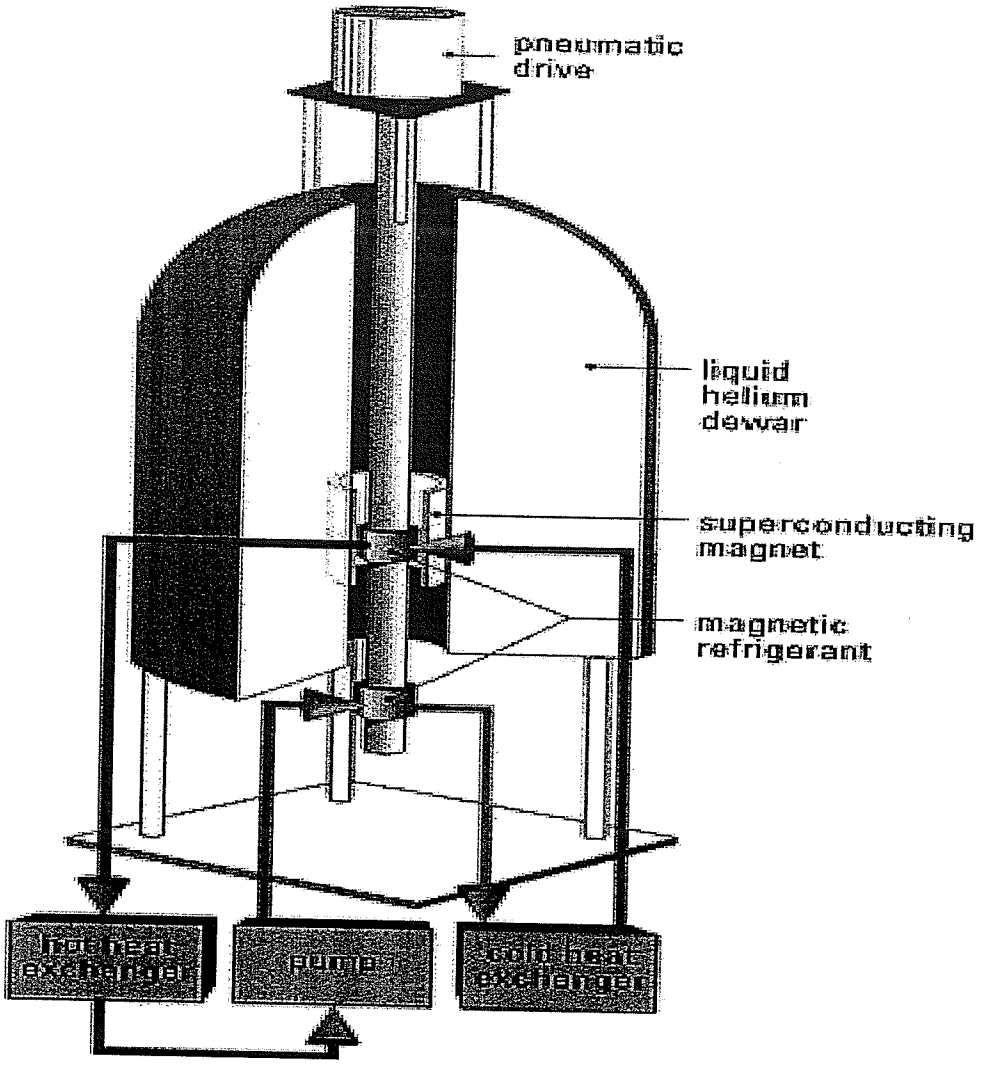

Figure 5.3 A schematic sketch of the proof-of-principle magnetic refrigerator [132]

superconductor magnet), this system gives a cooling power of 600 watts and a temperature span of 38K, a coefficient of performance (COP)* near 15 and an

* Coefficient of performance of a refrigerator is defined as the ratio of heat extracted from the cold environment to the work done on the system, in the case here by the magnetic field.

efficiency of approximately 60% of the Carnot efficiency. However, the use of a superconducting magnet limits its applicability. In 2001, the Astronautics Corporation of America fabricated the first room temperature refrigerator which used permanent magnets instead of superconducting magnets, making it feasible for use on a commercial scale.

Obviously, the major difference between magnetic and conventional refrigerators is the lack of a compressor. In the conventional gas compression refrigerator, the compressor is the most expensive and inefficient part, which is replaced by two beds of MCE material in the magnetic refrigerator. In addition, the transfer fluid is water or a water based mix, instead of a traditional refrigerant. The driving motor which moves the beds in and out of the magnetic field and the pump which circulates the transfer fluid are low-cost commercial products. Compared with conventional gas compression refrigerators, magnetic refrigerators have a higher efficiency and would conserve energy. With the use of water as a transfer fluid, it's also an environmentally friendly technique, eliminating ozone depleting chemical, green house gases (Hydrochlorofluorocarbon and Hydrofluorocarbons) and hazardous chemicals (NH_3).

5.5 The Measurement of the Magnetocaloric Effect

5.5.1 Direct measurement

There are two principle ways to evaluate the MCE in bulk magnetic materials. The MCE can be measured directly or calculated indirectly based on magnetization isotherms or the specific heat data.

Direct measurement techniques basically involve the measurement of the sample's temperature. In order to ensure adiabatic conditions, a rapid movement of the sample in and out of a magnet is required; alternatively, this can be realized by rapidly charging and discharging the magnet with a stationary sample. Since conventional electromagnets can only provide a field between 0-20 kOe, for a high field measurement, a superconducting magnet is usually employed. Direct MCE measurements up to 40 T have been reported. In this technique, the adiabatic temperature is given by:

$$\Delta T_{ad} = T_H - T_0 \tag{5.17}$$

where T_H is the sample's temperature in a field and T_0 is the temperature in zero field. ΔT_{ad} is the adiabatic temperature change in a given field. Many factors limit the accuracy of this technique; these include contact between the sample and temperature sensors, the thermometry, the isolation between the sample and the ambient atmosphere and the ability of the compensation circuitry to eliminate the effect of the changing magnetic field on the temperature sensors. In particular, the thermal isolation of the sample plays a significant role in the large entropy change samples.

Considering all these factors, direct measurement can result in an error between 5-10% as noted in recent reviews [133].

5.5.2 Indirect measurement from magnetization isotherms

The indirect approach usually involves the measurement of either the magnetization or specific heat. From equation (5.10), we can evaluate the entropy change becomes

$$\Delta S_m(T,H) = S_m(T,H) - S_m(T,0) = \int_{H_i}^{H_f} \left(\frac{\partial M}{\partial T}\right)_H dH \qquad (5.18)$$

In actual calculations, the exact differentials dM, dT, dH are replaced by finite but small changes $\Delta M, \Delta T, \Delta H$; this treatment will, of course, introduce an error. The accuracy of this method also depends on the accuracy of the magnetization and the temperature measurements, as well as the field stability. There are a series of steps then can be adopted to aid in the latter; these include warming above the ordering temperature prior to measurement, a slow sweep rate during the measurement, etc. Nevertheless, typical errors range from 3-10% when using magnetization isotherms to evaluate the entropy change [133]. This approach was questioned by Giguere et al. [134], because in some cases (for example, an ideal first-order phase transition) the entropy change around the transition temperature is not a continuous (differentiable) function; thus the Maxwell relations are not valid and calculations based on them are

no longer reliable. Instead, the direct adiabatic temperature measurement should be used or approaches based on the Clausius-Clapeyron equation which relates the magnetization jump at the transition and the shift of the critical point with magnetic field. Although arguments about this method remain, it is still a popular and straightforward way to estimate the magnetic isothermal entropy change in many cases.

5.5.3 Indirect measurement from specific heat data

From equation (5.12),

$$dS = \frac{C(T)_{H,P}}{T} dT \tag{5.19}$$

Here $C(T)$ is the specific heat at constant pressure and fixed magnetic field. S is the entropy as a function of temperature. Suppose a measurement of the specific heat is made between temperatures T_1 and T_2 ($T_2 > T_1$) and with two fixed fields H_1 and H_2 where $H_2 > H_1$; from the above equation, for any temperature falling between T_1 and T_2, the entropy change at temperature T between the two different fields is:

$$\Delta S_m(T,H) = S_m(T,H) - S_m(T,0) = \int_{T_1 \to 0}^{T} \frac{C_{H1}}{T} dT - \int_{T_1 \to 0}^{T} \frac{C_{H2}}{T} dT \tag{5.20}$$

In practice, it is usual to choose T_1 as close to zero temperature (0 K) as possible and usually the lower field is set to zero, so the above equation can be simplified to:

$$\Delta S_m(T,H) = S_m(T,H) - S_m(T,0) = \int_0^T \frac{C_H(H \neq 0) - C_H(H = 0)}{T} dT \qquad (5.21)$$

Clearly the entropy change depends strongly on the difference of the specific heat at two fixed fields. This equation is derived on the assumption that the specific heat is a continuous function of the temperature; namely, the system must undergo a continuous phase transition and all changes in the magnetic system are assumed to be equilibrium or quasistatic processes. However, some authors [135] assume that the validity of this equation can be extended to systems which undergo a first – order / discontinuous phase transition, because, in systems with a discontinuous entropy change, the magnitude of the magnetocaloric effect is mainly influenced by the difference in the entropies of the low and high magnetic field phases. The accuracy of this method depends on the accuracy of the temperature dependence of the specific heat data. If it is assumed that the accuracy of the specific heat is field independent, the relative error in the magnetic entropy change will be reduced when the field interval ΔH is increased.

5.6 Properties of the Heusler Alloy Ni_2MnGa

Ferromagnetic shape memory alloys (FSMA) are a class of new materials which combine properties of ferromagnetism and a thermoelastic martensitic transformation in the ferromagnetic state. Various FSMA systems, e.g. Fe-Pd [136], Fe-Pt, Co-Ni-Al [137], Co-Ni-Ga [138], and Ni-Mn-Ga, are amongst those that have been investigated to date. The latter, the Ni-Mn-Ga system, has attracted considerable attention due to the large field induced strains occurring at low field [139]. Ni_2MnGa, the parent compound of this system, possesses a high temperature cubic phase with a Heusler structure, which changes to a lower symmetry tetragonal structure with $c/a \approx 0.95$ around $T_m \sim 200K$. In practice, the martensitic transformation temperature, T_m, can be controlled by changing the chemical composition of the alloy. Besides the possible application of this "smart" material as an actuation device [140], this system also provides an excellent platform to investigate various aspects of phase transitions and microstructural formation because both magnetic and structural phase transitions can be realized in a single system. However, the present studies will focus on the magnetic properties of the Ni-Mn-Ga system, in particular, the giant magnetocaloric effect (GMCE).

As reviewed in the previous chapter, several systems which display a first-order phase transition also exhibit a giant magnetocaloric effect (GMCE); such systems include the Gd-based compound $Gd_5Si_2Ge_2$, $MnFeP_{1-x}As_x$ and $MnAs_{1-x}Sb_x$. The origin of the large entropy change in these systems can be traced to the substantially different contributions to the entropy in the magnetically ordered and disordered

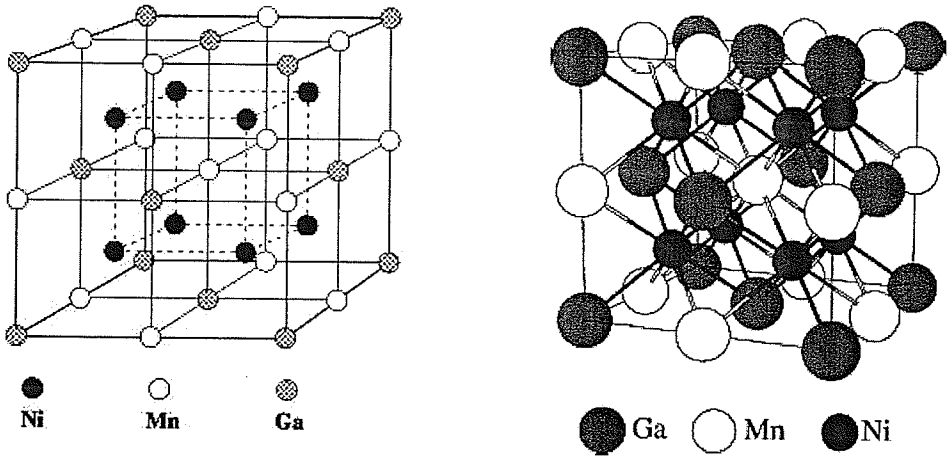

Figure 5.4 A simple sketch of the crystal structure of the ferromagnetic shape memory alloy Ni_2MnGa.

regimes which are separated by this first-order phase transition. There also exist a number of systems which display sequential phase transitions on cooling; the Ni-Mn-Ga system is one of them.

Figure 5.4 shows the structure of the ferromagnetic shape memory alloy Ni_2MnGa. The parent compound Ni_2MnGa is a ferromagnetic Heusler alloy with $L2_1$ structure* in the ground state [140]. Ni ions reside on the corner sites of the body-centered-cubic structure, while Mn and Ga ions alternately occupy body-center sites. Figure 5.5 is a schematic sketch of the zero field susceptibility versus temperature on warming and cooling for Ni_2MnGa. On warming, this Heusler alloy undergoes a first-order phase transition from a tetragonal martensite to cubic austenite structure at

* $L2_1$ is *Strukturbericht* Designation for Heusler structure. L type specifies the structure of alloys

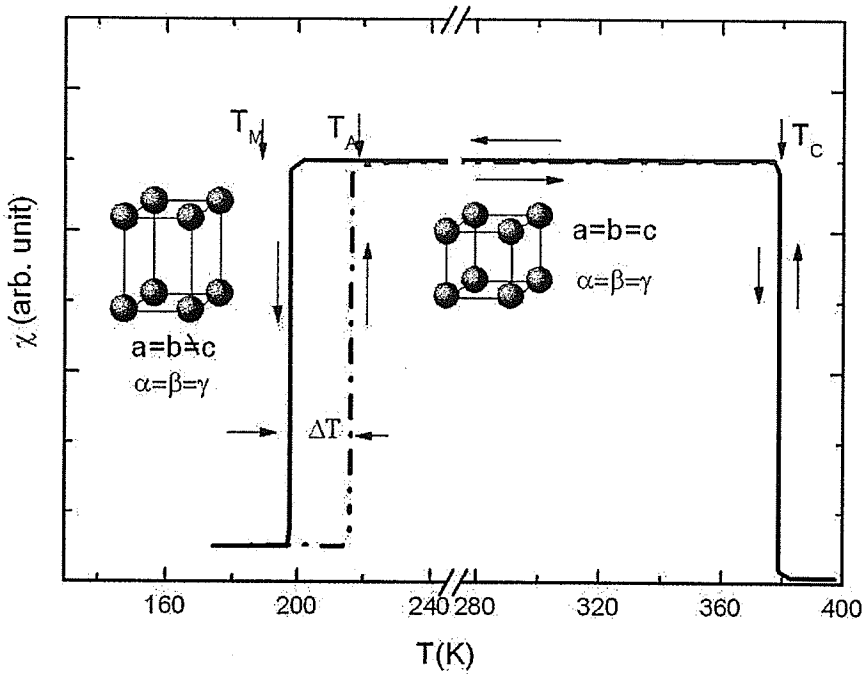

Figure 5.5 A schematic sketch of the zero field susceptibility measured on warming and cooling. Actual data can be found in the following sections.

$T_m \sim 200$ K; this structural transition is fundamentally different from the transition in other shape memory alloy systems, because the transition is accompanied by a simultaneously magnetic phase transition and an abrupt change in the magnetization. At the transition temperature, T_m, a large entropy change is anticipated, since the structural and magnetic phase transitions occur simultaneously. At higher temperature, as figure 5.5 shows, the system undergoes a second-order ferromagnetic to paramagnetic phase transition, which is characterized by a Curie temperature, T_c. Obviously, this system possesses two kinds of magnetic phase transitions: a first-

order ferromagnetic to ferromagnetic (order-order) transition and a second-order ferromagnetic to paramagnetic (order-disorder) transition, with a structural phase transition accompanying the first-order magnetic phase transition. It provides an ideal system to investigate the relationship between magnetic phase transitions and the magnetic entropy change. In addition, by varying the compositions of the system, it is possible to engineer the simultaneous occurrence of the first-order structural martensitic transformation and the continuous magnetic transition [141]. While previous experience suggests that the dominant entropy change accompanies the first-order phase change, it appeared possible that if these transitions could be merged – or at least brought into close proximity – an enhancement of the separate entropy changes – and hence the MCE – could be accomplished. Thus, the Ni-Mn-Ga system appears to be an ideal system to search for promising new magnetic refrigerants.

5.7 Sample Preparation and Measurement Techniques

A series of samples were prepared by arc melting in an argon arc furnace; 99.95% pure Ni, 99.99% pure Ga and spectroscopic grade Mn were used as starting materials. Each specimen was inverted and remelted several times to ensure better homogeneity. In order to further improve the stoichiometric homogeneity, a heat treatment for 220 hours at 850^0C in an argon atmosphere was performed. Finally, the

samples were quenched into iced water. Quenching is an important step to obtain the highest degree of chemical order but increases the brittleness of samples. The actual composition of each sample was determined by electron microprobe analysis (Cameca SX 100). As expected, the Mn content was usually 1-2% lower than the nominal composition, which was compensated for by a slight adjustment to the starting materials. Powder X-ray diffraction using Cu Kα radiation was employed to determine the room temperature (RT) crystal structures, which are summarized in Table 5.1. The related magnetic measurements, carried out on samples cut from the original quenched ingots, used the Quantum Design PPMS 6000 magnetometer described in Chapter 3. These measurements included a number of magnetization (M) versus applied field (H_a) isotherms at a range of fixed temperatures and some temperature dependent ac susceptibility ($\chi(H,T)$) measurements (at 2.4 kHz in an ac driving field of 30 mOe rms applied along the longest axis of typically (6×1×1) mm^3 samples) in fixed dc biasing fields (applied parallel to the ac field). For magnetization isotherm measurements, the sample was usually heated above T_c to achieve a demagnetized state prior to zero-field cooling to a set temperature; a half an hour waiting time was then used in order to reach better thermal equilibrium before the start of the measurement. During the measurement, a sufficiently slow field sweep rate and 5 scan averaging were employed to enhance accuracy at every measurement point. A similar measurement procedure was applied to the temperature dependent ac susceptibility measurement.

5.8 The Relationship Between Sequential Magnetic Phase Transitions and MCE in the Ni-Mn-Ga System

5.8.1 General overview

Table 5.1 summarizes the physical data from all samples with different values of T_m and T_c. Basically, T_m covers a temperature range between 272 K and 338 K while T_c covers a temperature range between 308 K and 368 K. As far as structure is concerned, for sample 2 ($Ni_{50.9}Mn_{24.7}Ga_{24.4}$), T_m is below room temperature and it displays the expected cubic structure at room temperature (300 K). By contrast, all other samples, (sample 1 ($Ni_{57.2}Mn_{15.9}Ga_{27.0}$), sample 3 ($Ni_{51.6}Mn_{24.7}Ga_{23.8}$), sample 4 ($Ni_{52.9}Mn_{22.4}Ga_{24.7}$), sample 5 ($Ni_{52.7}Mn_{23.9}Ga_{23.4}$) and sample 6 ($Ni_{55.2}Mn_{18.6}Ga_{26.2}$)) are tetragonal at room temperature. In particular, for sample 6 (the focus of the discussion in this section), X-ray diffraction confirmed that it was a single phase tetragonal structure with room temperature unit cell dimensions a = b = 5.980 Å and c = 5.835 Å, in general agreement with previous reports at similar composition [142].

The general magnetic behaviour of all samples is summarised in figure 5.6, which shows the temperature dependence of the zero-field ac susceptibility (measured at 2.4 kHz in an ac driving field of 30 mOe rms). This figure illustrates that progressing from samples 2 to 5, there are two distinct phase transitions and the

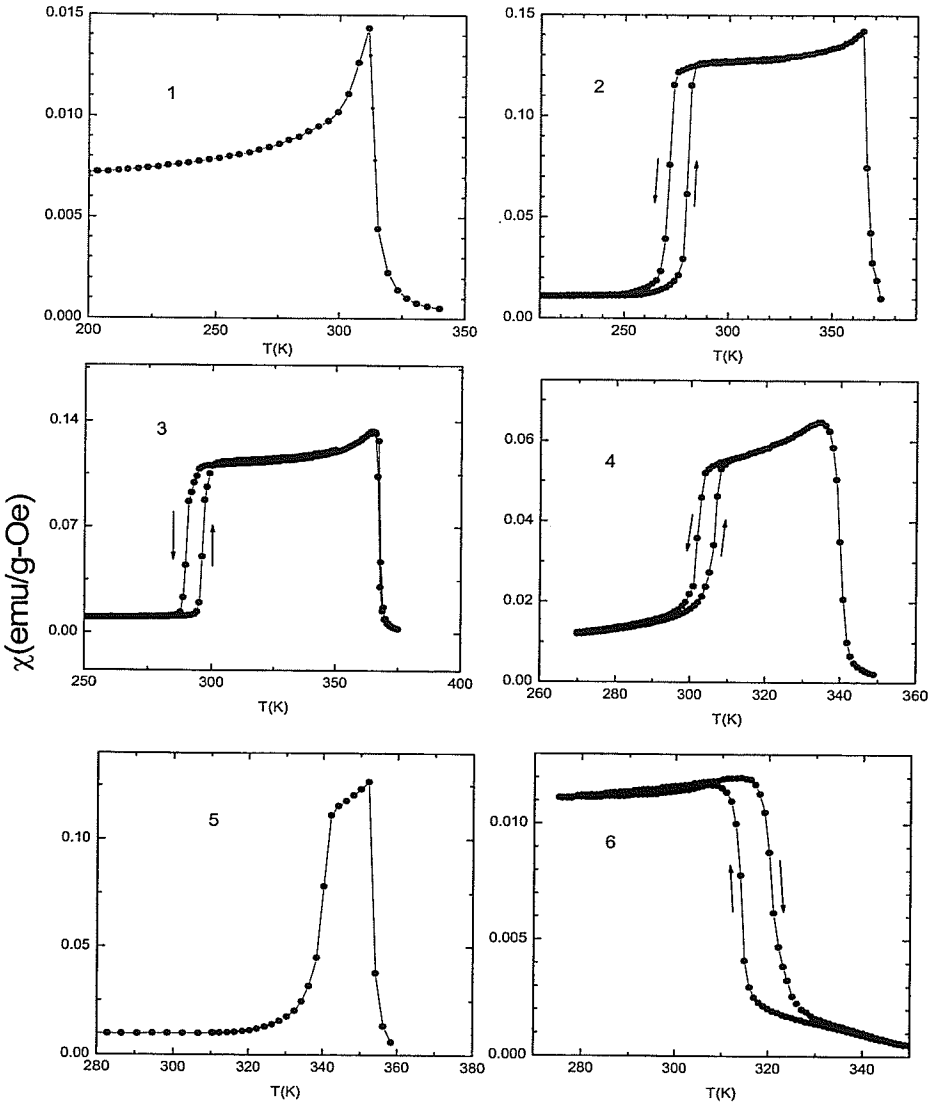

Figure 5.6 Zero-field ac susceptibility for all samples; the numerical values inside figures refer to the order in Table 5.1

Sample	Composition	RT Structure	Lattice Param.(Å)	T_M(K)	T_C(K)	ΔT(K)	ΔS_M(J kg^{-1} K^{-1})	e/a
1	$Ni_{57.2}Mn_{15.9}Ga_{27.0}$	Tetragonal	a=b=5.944 c=5.842	–	308	–	-2.0 (at 310 K)	7.64
2	$Ni_{50.9}Mn_{24.7}Ga_{24.4}$	Cubic	a=b=c=5.831	272	365	93	-3.5 (at 274K)	7.55
3	$Ni_{51.6}Mn_{24.7}Ga_{23.8}$	Tetragonal	a=b=5.838 c=5.800	296	368	72	-7.0 (at290K)	7.60
4	$Ni_{52.9}Mn_{22.4}Ga_{24.7}$	Tetragonal	a=b=6.011 c=5.808	305	340	35	-8.6 (at 304 K)	7.60
5	$Ni_{52.7}Mn_{23.9}Ga_{23.4}$	Tetragonal	a=b=5.988 c=5.849	338	354	16	-15.6 (at 337 K)	7.65
6	$Ni_{55.2}Mn_{18.6}Ga_{26.2}$	Tetragonal	a=b=5.980 c=5.835	315	315	0	-20.4 (at 317 K)	7.61

Table 5.1 Summaries of compositions, room temperature structure, lattice parameters, fist-order transitions temperatures, Curie temperatures, temperature differences, maximum entropy changes and the average number of valence electrons per atom for all samples.

first-order transition temperature (T_m) increases while the second-order transition temperature (T_c) decreases. By contrast, sample 1 shows a pure second-order phase transition without any hysteresis within experimental uncertainty (this point will be confirmed later through the test of various power laws). However, sample 6 also displays but a single transition at T_m (T_c) = 320 K. Here note the presence of a thermal hysteresis of some 7 K on subsequently cooling this sample, as shown in figure 5.6. Such hysteresis is a signature that the first-order nature of the transition persists.

In the following paragraphs, three samples – sample 1, sample 4 and sample 6 – will be analyzed in detail in order to identify the characteristics that are important to this discussion. Through magnetization isotherms, temperature dependent ac susceptibility measurements and the associated critical analysis, it will be confirmed that sample 1 ($Ni_{57.2}Mn_{15.9}Ga_{27.0}$) displays a pure second-order phase transition; sample 4 ($Ni_{57.2}Mn_{15.9}Ga_{27.0}$) displays the sequential phase transitions mentioned above, i.e. a continuous paramagnetic to ferromagnetic phase change at T_c and a first-order/discontinuous magnetic transition accompanying a martensitic transformation at a lower temperature T_m; sample 6 ($Ni_{55.2}Mn_{18.6}Ga_{26.2}$) displays a magnetic phase transition with both first- and second-order characters. The present discussion, however, will focus on investigating, in detail, the nature of the magnetic phase transitions that occur in these specimens (i.e. at T_m and/or T_c) and correlate the characteristics of such transitions with the associated magnetocaloric effect (MCE).

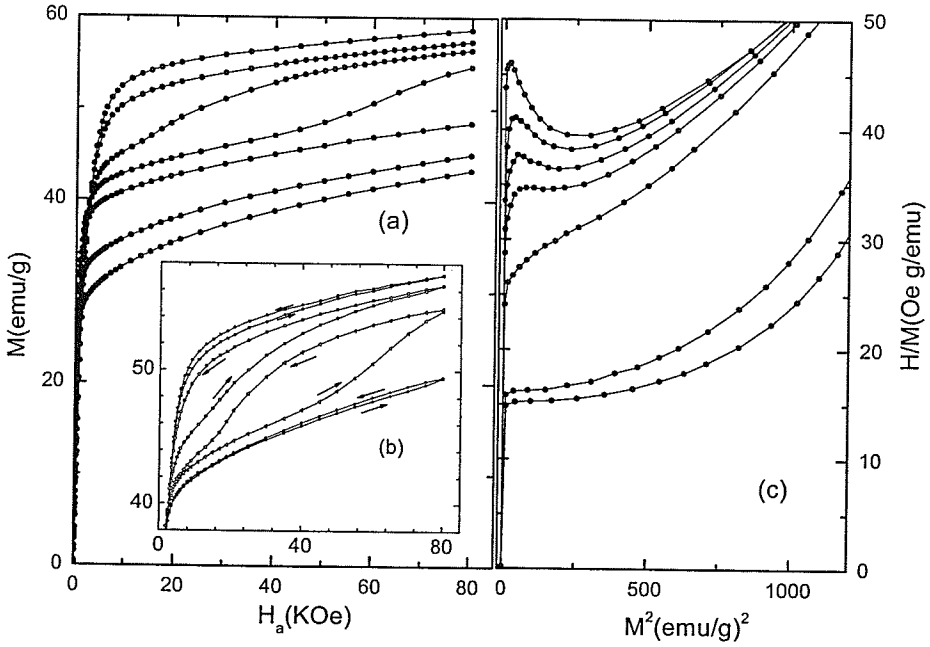

Figure 5.7Magnetisation isotherms: (a) sample 4 at 298 K (top), 302 K, 304 K, 306 K, 310 K, 320K and 325 K (bottom); (b) complete isotherms (field increasing and decreasing) for sample 4 at temperatures of 302K (top), 304 K, 306 K and 308 K (bottom); (c) M^2 versus H/M plot (Arrott plots) for sample 4 at temperatures of 290 K (top), 294, 298, 300, 302, 304 and 306 K (bottom).

5.8.2 Analysis for $Ni_{52.9}Mn_{22.4}Ga_{24.7}$ (sample 4) with sequential magnetic phase transitions

Clear hysteresis centered near $T_m \approx 305$ K is observed for sample 4 as shown in figure 5.6 and this feature provides direct evidence for the presence of a first-order

phase transition. Another feature which is generally associated with a first-order transition is an "S" shaped magnetization isotherm, i.e. a discontinuous jump in the ideal case, which is broadened in real systems, due likely to disorder resulting principally from departures from stoichiometry [90]. A carefully examination of the field dependent magnetization data for sample 4 confirms this, as demonstrated in figure 5.7. Figure 5.7 (a) presents isotherms in the field-increasing mode only for sample 4. Here an "S"-shaped feature characteristic of a first-order (field-induced) metamagnetic transition can clearly be identified near $T_m \approx 305$ K. Such a criterion has been successfully applied in Chapter 4 to identify the first-order nature of the transition in a single crystal $La_{0.73}Ca_{0.27}MnO_3$ sample, as well as other systems displaying magnetocaloric characteristics (i.e. $Gd_5(Si_2Ge_2)$ [119], $Gd_5(Si_xGe_{1-x})_4$ [143, 144] and $DyMn_2Ge_2$ [145] amongst others). From figure 5.7(a), the metamagnetic field, H_M, which is the transition field from a paramagnetic to a ferromagnetic state, can be estimated by finding the maximum in dM/dH; this method has been widely used to identify the metamagnetic field in the doped manganites and other intermetallic compounds, as described in previous chapter. Figure 5.7(b) presents complete magnetization isotherms in both field-increasing and field-decreasing modes; once again, obvious field dependent hysteresis can be found around $T_m \approx$ 305 K. An Arrott plot for sample 4 is shown in figure 5.7(c), where magnetization isotherms are replotted in an M^2 versus H/M format; a careful examination of this plot reveals negative slopes at intermediate magnetic fields, although the initial

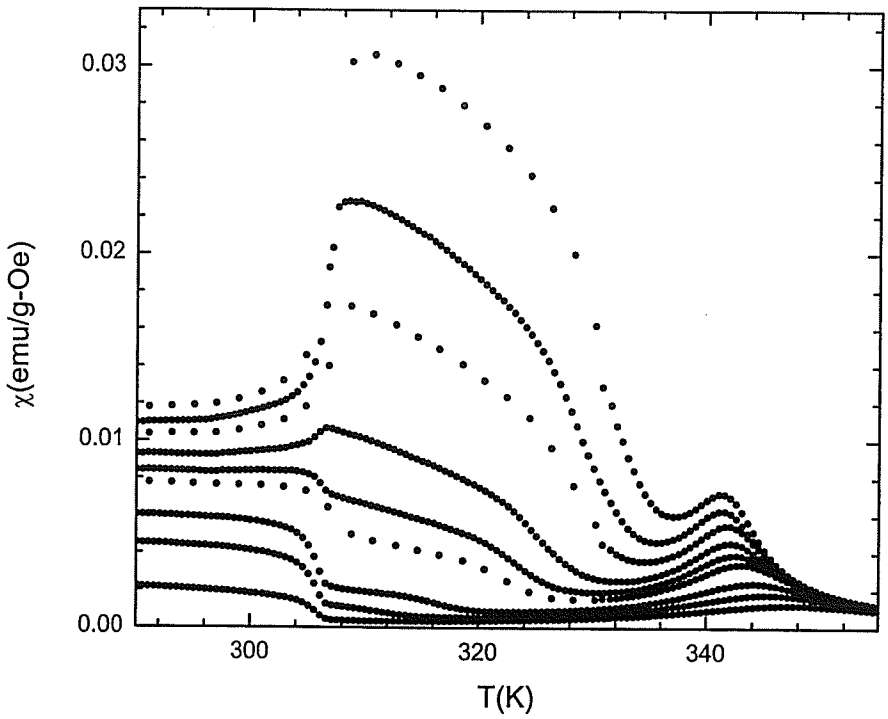

Figure 5.8 Ac susceptibility data for sample 4 measured on warming (following zero-field cooling) in static fields of 400 Oe (top), 500 Oe, 600 Oe, 800 Oe, 1000 Oe, 1200 Oe, 3000 Oe and 5000 Oe (bottom).

slopes are positive. The negative slopes here, indicating the existence of a first-order phase transition, can be understood on the basis of the Landau expansion, as discussed in chapter 2. Zero-field susceptibility and magnetization isotherm data in figure 5.7, for sample 4, suggest the transition around $T_m \approx 305$ K is a first-order/discontinuous phase transition. This point is further confirmed in figure 5.8, where temperature dependent ac susceptibility curves (plots of $\chi(H_a,T)$ vs T for fixed static biasing fields, H_a) are plotted for temperatures between 285 K and 350 K in

static superimposed fields between 400 Oe and 5 kOe. A clear anomaly corresponding to $T_m \approx 305$ K can be seen in this figure. Near this temperature the susceptibility displays an abrupt change, $\Delta\chi$, which shows a strong field dependence. With increasing static biasing field, the temperature dependence of the susceptibility changes from positive ($d\chi/dT>0$) to negative ($d\chi/dT<0$). In the intermediate field range between 900 Oe to 1000 Oe, no steep step is seen. It should be noticed that all these changes happen in a narrow temperature range of 304-308 K. The relationship between this lower martensitic transition and the magnetocaloric effect will be examined by establishing the metamagnetic boundary (the first-order phase boundary delineated in an $H_M(T)$ vs T plot) later.

The feature which should however to be emphasized in figure 5.8 is not the lower transition around $T_m \approx 305$ K, but the series of peaks near 340 K. These peaks move upward in temperature and decrease in amplitude as the static superimposed biasing field H_a is increased. Maxima that behave in this way are an unequivocal signature of a second-order/continuous magnetic phase transition, as discussed earlier. While the generic field and temperature dependent behaviour of this peak structure can be understood using arguments of a general nature [146] based on the fluctuation/dissipation theorem – the maxima (near $T_c \sim 340$ K in figure 5.8) delineate the locus of a crossover line in the (H-T) plane separating a lower temperature region of field-dominated response from a higher temperature, thermally dominated regime – the detailed behaviour of this crossover line is model dependent.

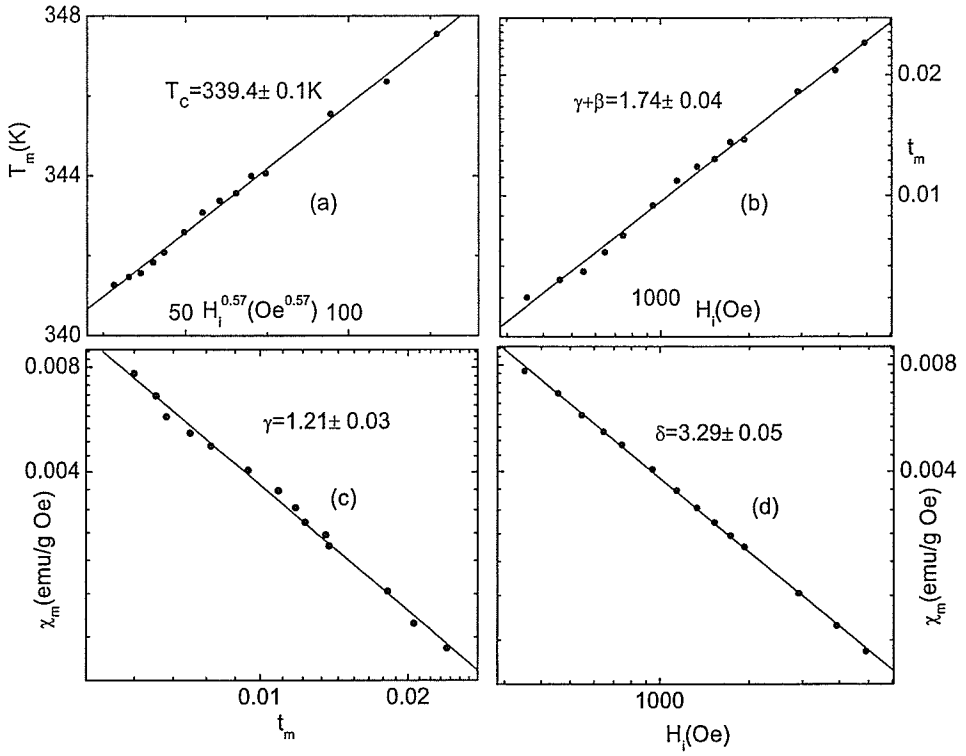

Figure 5.9 (a) Estimate of T_c from the critical peak temperatures in various internal fields in the form of a t_m vs $H_i^{0.57}$. (b) Cross-over (exponent) plot of the reduced peak temperatures vs internal fields. (c) The peak susceptibility plotted against the reduced temperature t_m. (d) The peak susceptibility plotted against the internal field. (b), (c) and (d) are all on a double logarithmic scale.

This can be demonstrated by examining various power-law relationships predicted to occur in the vicinity of a conventional second-order transition by the static scaling law, as described in Chapter 2. From equation (2.21), the plot of the peak temperature T_m against $H_i^{1/(\gamma+\beta)}$ should be linear, and its intercept gives the Curie temperature, T_c. By choosing 3D Heisenberg model values of $\gamma+\beta=1.75$,

T_c=339.4±0.1 is obtained as shown in figure 5.9(a). Figure 5.9(b) confirms again both these exponents and T_c estimates; the reduced peak temperatures, t_m, are plotted against the internal field, H_i, on a double logarithmic scale with Heisenberg model exponents and the straight line from the least-square fit confirms the power law prediction. The exponent γ can be found by plotting the amplitude of the susceptibility maxima χ_m against the reduced peak temperatures t_m on a double logarithmic scale, as figure 5.9(c) shows; these data yield $\gamma = 1.21\pm0.03$. The exponent δ is found from a least-square fit of the data in figure 5.9(d), where the amplitudes of the peak susceptibility, χ_m, are plotted against the internal field, H_i; here $\delta = 3.29\pm0.05$, which is close to the mean field theory prediction of $\delta = 3$. Overall, these critical exponents estimated from figure 5.9 lie in between mean field (γ=1, β=0.5, δ=3) and 3D Heisenberg model values (γ=1.387, β=0.365, δ=4.8). The crossover line, Figure 5.9(a) and (b), yields values close to the Heisenberg prediction ($\gamma+\beta$=1.75), the susceptibility exponent $\gamma = 1.21$ is intermediate between these two models, while the equation of state exponent, $\delta = 3$, is closer to the mean field model than the Heisenberg model result. While the presence of disorder induced by (deliberate) departures from stoichiometry complicates the critical analysis – particularly as far as the emergence of critical peaks at low field are concerned, the deviation from the 3D Heisenberg model values is likely due to magnetic anisotropy present in the sample [61]. The magnetic anisotropy plays an important role in the

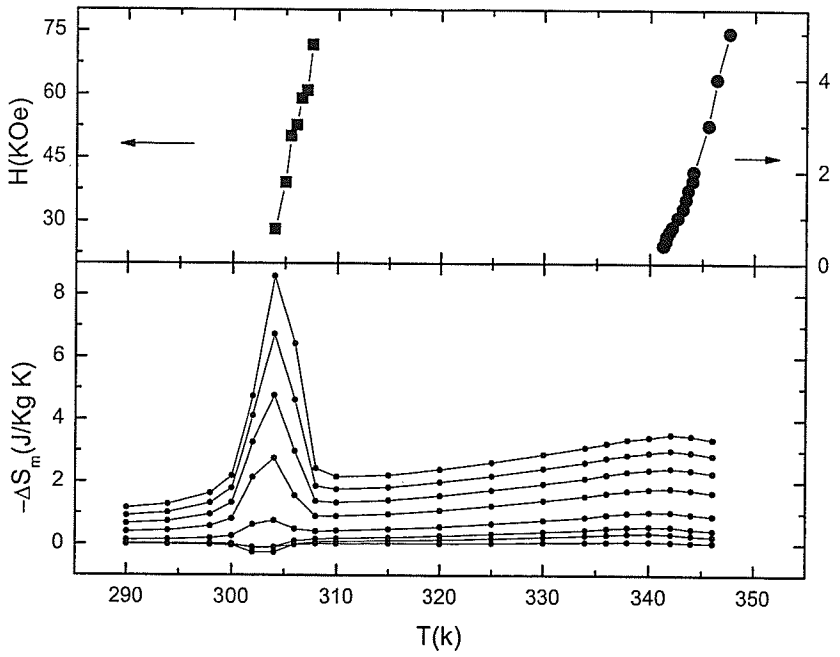

Figure 5.10 Upper panel: the metamagnetic boundary ($H_M(T)$ vs T, squares) and the crossover line (T_P vs H, circles); Lower panel: the magnetic entropy change ΔS_M plotted against temperature at fields of 1000 Oe (bottom), 3000 Oe, 5000 Oe, 10000 Oe to 50000 Oe (top) in 10000 Oe steps.

Ni-Mn-Ga system. In essence, the magnetic shape memory effect in the system is driven by the magnetic anisotropy energy, which differentiates this system from the temperature-driven conventional shape memory alloys. The magnetic anisotropy energy in the parent compound Ni_2MnGa has been investigated both experimentally and theoretically [147].

The behaviour of $H_M(T)$ as a function of temperature near T_m is presented in the upper panel of figure 5.10. As might be anticipated from figures 5.7(a) and (b), the metamagnetic boundary is a very steep function of temperature in this sample; the data points shown were deduced from field increasing sweeps (due to the hysteresis noted previously, $H_M(T)$ estimates from field decreasing sweeps will be lower, but nevertheless extrapolate to the same T_m). The lower panel of figure 5.10 reproduces the entropy change, ΔS_M, associated with both the first- and second- order phase transitions as estimated from the Maxwell relations using equation (5.18)

$$\Delta S_m(T,H) = S_m(T,H) - S_m(T,0) = \int_0^H \left(\frac{\partial M}{\partial T}\right)_H dH$$

Figure 5.10 demonstrates conclusively the close correspondence between the entropy change $\Delta S_M(T,H)$ associated with the magnetocaloric effect and the corresponding phase "boundaries" as represented quantitatively by the metamagnetic boundary ($H_M(T)$ vs T) and the crossover line (H vs T_P) characterizing the first- and second-order transitions respectively. This figure also illustrates that the dominant entropy change occurs in the vicinity of the first-order transition (a combined magnetic and structural transition resulting in a significant increase in moment, as can be seen from figure 5.7(a) and (b)). Moreover, the magnetic entropy change corresponding to the second-order phase transition possesses a much wider peak than that appearing around the first-order phase transition; this suggests an effective characteristic of the first-order phase transition is to confine the MCE in a narrow

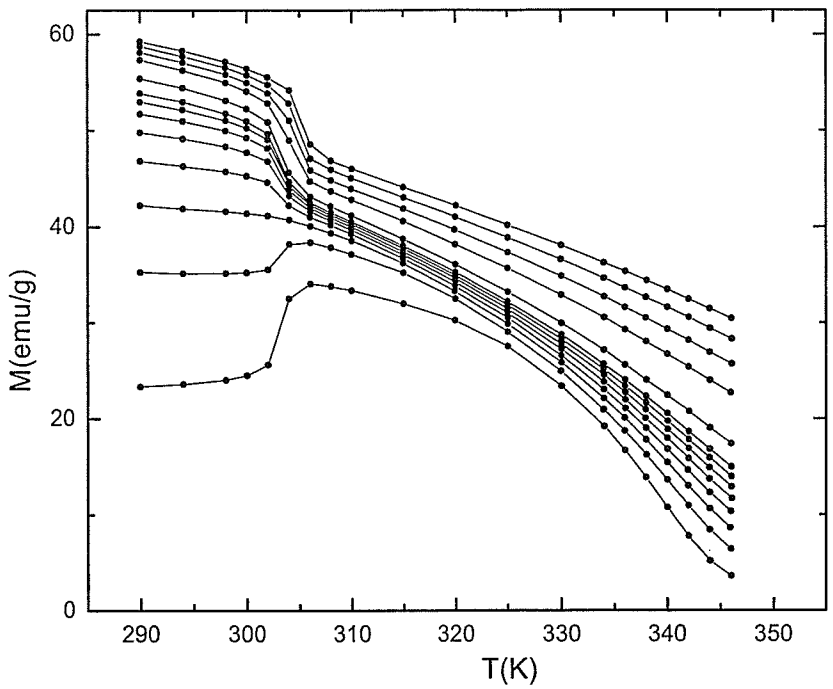

Figure 5.11 Magnetization as a function of temperature for sample 4 at fields of 50 kOe (top) to 10 kOe in 10 kOe steps, then 8 kOe to 1 kOe (bottom) in 1 kOe steps.

temperature range. A careful examination of the lower panel of figure 5.10 reveals that the magnetic entropy change maxima, centered near 305 K and 340 K respectively, strongly depend on field; with increasing of field, the magnetic entropy change ΔS_M increases monotonically for both. In lower fields (H < 5000 Oe), the maximum entropy change corresponding to the first-order phase transition becomes positive, while the magnetic entropy change, ΔS_M, appearing near the second-order phase transition remains negative over the whole field range. This difference in the

behaviour can be understood on the basis of the magnetization temperature coefficient, namely, dM/dT. Figure 5.11 reproduces temperature dependent magnetization curves for sample 4 at fields between 1 kOe and 50 kOe. The magnetization has a much steeper temperature dependence near the first-order phase transition than around the emerging second-order phase transition. Most importantly, dM/dT around the first-order phase transition has a crossover from negative to positive at a field of 3000 Oe, which leads to the entropy change crossover appearing in the lower panel of figure 5.10. By contrast, dM/dT remains negative around the second-order phase transition, but with a lower magnitude.

5.8.3 Analysis for $Ni_{55.2}Mn_{18.6}Ga_{26.2}$ (Sample 6) with merged first- and second-order phase transitions

Figure 5.12(a) reproduces magnetization isotherms for increasing field at various (fixed) temperatures for sample 6 ($Ni_{55.2}Mn_{18.6}Ga_{26.2}$) in the vicinity of its ferromagnetic ordering temperature. The data in figure 5.12(a) confirm that the sample is ferromagnetic and easy to saturate below T_c (T_m); in particular the "S"-shape of magnetisation curves in the temperature interval 317-324 K is clear, a feature generally characterizing a metamagnetic first order transition. Figure 5.12(b) shows complete isotherms (field increasing and decreasing) for sample 6 at various fixed temperatures. A clear field dependent hysteresis is observed, which is also a

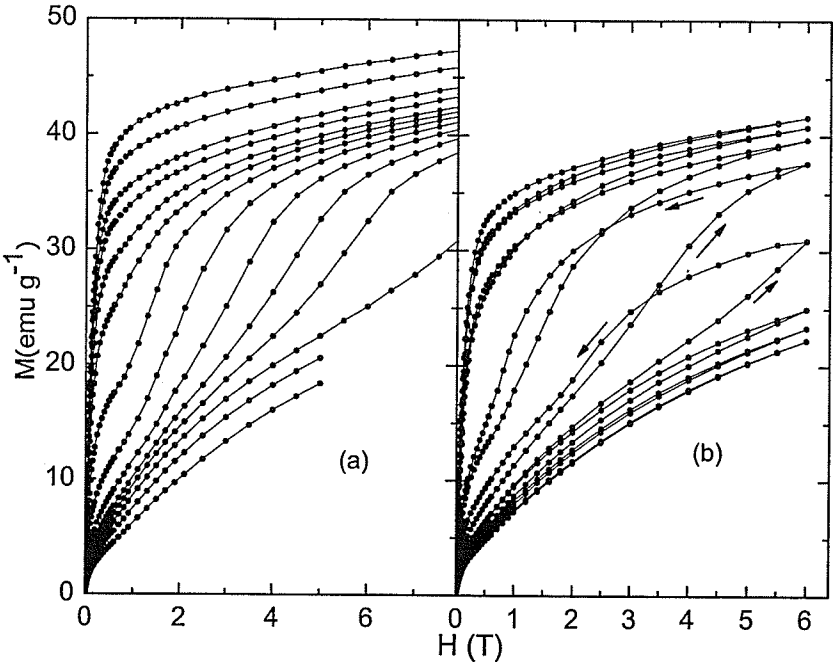

Figure 5.12 (a) The magnetization dependence of sample 6 on applied magnetic field measured at various temperatures: from top to bottom 300, 305, 310, and 312 K, then 314 to 320 K in steps of 1 K; (b) complete isotherms (field increasing and decreasing) for sample 6 at various temperatures: from top to bottom 312 to 326 K in steps of 2 K.

characteristic of a field-induced metamagnetic transition.

Figure 5.13 reproduces the susceptibility as a function of temperature at static biasing fields from 8 kOe up to 35 kOe for sample 6. Isokaps of the ac susceptibility reveal a series of peaks, the amplitude of which decrease while the temperature of the peaks increase with increasing applied field. From the theoretical discussion in chapter 2, such features are linked to the presence of a second-order/continuous

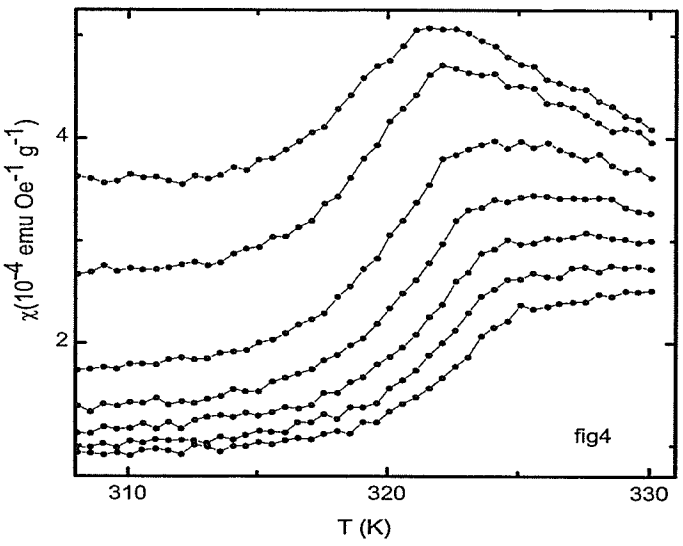

Figure 5.13 The temperature dependence of the ac susceptibility in fixed fields of 0.8, 1.0, 1.5, 2.0, 2.5, 3.0 and 3.5 T (from top to bottom) for sample 6. The behaviour of the peak structure with increasing field is a characteristic of a second-order magnetic phase transition.

magnetic phase transition. As mentioned earlier, the maxima in figure 5.13 delineate the locus of a crossover line in the field (H) and temperature (T) plane, which separates the field-dominated region from the thermally- dominated region. The critical peak behaviour follows a series of power-laws, as discussed in Chapter 2. From these, a set of critical exponents, which usually show model dependence, can be extracted. A comprehensive critical analysis for sample 6 is presented in figure 5.14. Using 3D Heisenberg exponents, T_c=314.5±0.5 K was obtained by extrapolating the high field peak temperatures to zero field as shown in

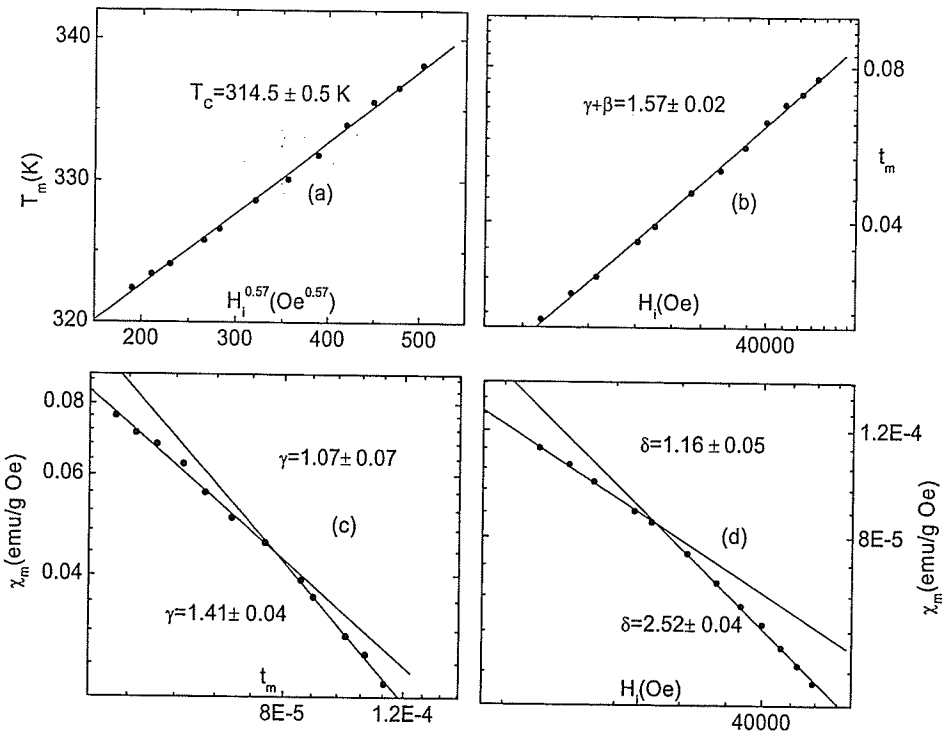

Figure 5.14 The plots show the data fit to find critical exponents values for sample 6.

figure 5.14(a). Figure 5.14(c) shows the peak susceptibility plotted versus the reduced peak temperature. The fit to the low field data points yields $\gamma = 1.07 \pm 0.07$, which is close to mean field theory predictions, while the high field points yield $\gamma = 1.41 \pm 0.04$. The peak susceptibility versus internal field is plotted in figure 5.14(d). Obviously, a clear curvature is apparent and no linear fit can be made to fields in the range between 9 kOe- 55 kOe; fits to low and high field points yield $\delta = 1.16$ and $\delta =$

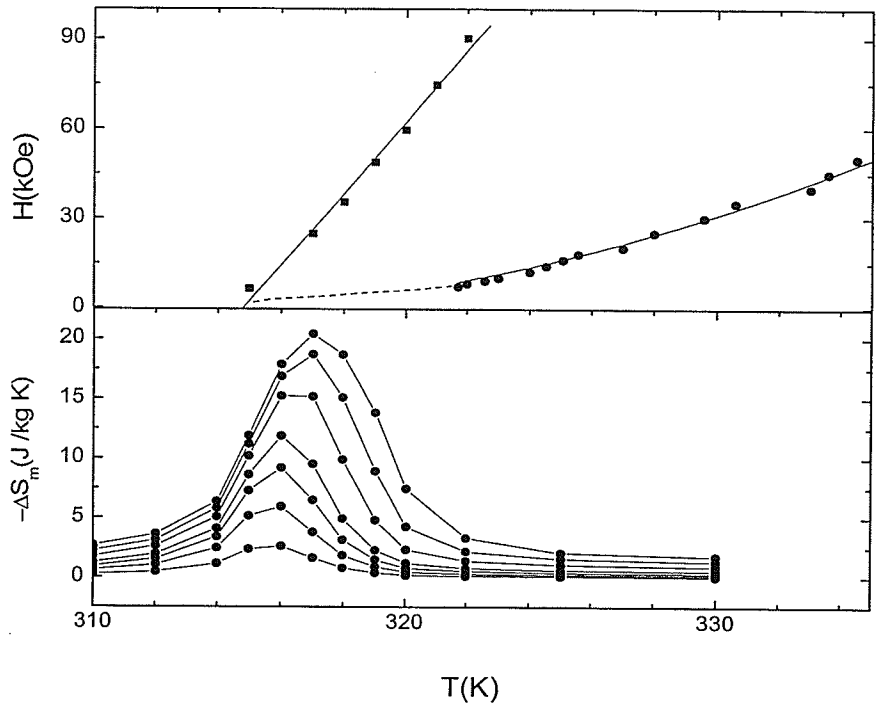

Figure 5.15 Upper panel: the metamagnetic boundary ($H_M(T)$ vs T, squares) and the crossover line (T_m vs H, circles); the dashed portion is an extrapolation of this fit to H = 0. Lower panel: Magnetic entropy change of $Ni_{55.2}Mn_{18.6}Ga_{26.2}$ (sample 6) at fields of 5000 Oe (bottom) to 20000 Oe in 5000 steps, then 30000 to 50000 Oe in 10000 Oe (top) steps.

2.52, respectively. Actually, the curvature in the figure 5.14(d) is likely a consequence of the "S" shaped magnetization isotherms which appear near the Curie temperature (magnetization isotherms near the critical temperature usually assume the power law form $M \propto H_i^{1/\delta}$ and the "S" shaped characteristics are consistent with such variations in the estimates for δ). Clearly, sample 6 possesses some

characteristics of a second-order/continuous phase transition; however, the critical exponents deduced from figure 5.14 are not consistent with any existing single model predictions. Likely, the near coincidence of a first-order and a second-order phase transition makes the asymptotic exponents difficult to access, as in single crystal $La_{0.73}Ca_{0.27}MnO_3$. However, a test of universality class is not the principal focus here and more comprehensive measurements coupled with careful sample preparation – possibly involving the use of single crystal – are needed to establish the universality class definitively. Rather, the focus is to demonstrate that, while the dominant entropy change does occur at the first-order magnetic transition (accompanied here by a structural phase change in this system, from tetragonal to cubic on warming), this entropy change can be further enhanced through the (essential) coincidence of a second-order magnetic transition. This assertion can be demonstrated conclusively by the establishment of the metamagnetic boundary from magnetization isotherms and the crossover line mentioned above.

Figure 5.15 reproduces both the metamagnetic boundary ($H_M(T)$ vs T) and the crossover line (H vs T_P) for sample 6; the latter extrapolates to $T_c \approx 315$ K from a T_P vs $H^{(\gamma+\beta)^{-1}}$ plot with $\gamma+\beta=1.75$ as shown in figure 5.14(a), and this temperature coincides with the origin of the metamagnetic boundary at $T_m \approx 315$ K within experimental uncertainty. A carefully examination the slope of the metamagnetic boundary dH_M/dT give a value ~12 kOe/K, which is less steep than the value found when the two transitions are separated, as in sample 4. This figure demonstrates that,

as a result of compositional tuning, features consistent with both a first-order and a second- order (magnetic) transition appear essentially coincidentally in this sample. The magnetic entropy change associated with these merged magnetic phase transitions is evaluated based on magnetization isotherms in figure 5.12(a) and the resulting ΔS_m for fields between 5 kOe and 50 kOe is presented in the lower panel of figure 5.15. Specifically, the magnetic entropy changes, ΔS_M, evaluated at 15 kOe and 50 kOe are reproduced in figure 5.16, where the corresponding values for pure Gd are included for comparison. It indicates that the corresponding entropy change ΔS_M in a field of 50 kOe reaches a peak value of –20.4 J kg^{-1} K^{-1} near 317 (in a 50 kOe field) just below T_c (T_m); in a lower field of 15 kOe, the peak entropy change is -9.2 J kg^{-1} K^{-1}. Both of these values are substantially larger than those of Gd, as shown in figure 5.16. In particular, the value ΔS_M = –20.4 J kg^{-1} K^{-1} near 317 in a 50 kOe field exceeds the sum of the individual maximum changes occurring with separate first- and second- order transitions. Moreover, it also exceeds the value from an isolated first-order transition in samples displaying sequential first- and second-order transitions. This value is among the largest entropy change obtained in this system, including a single crystal sample. The entropy change, ΔS_M, evaluated in a similar way for all samples is listed in Table 5.1. Immediately evident from this table is the fact that there is a clear correspondence between the magnitude of entropy change, ΔS_M, and the temperature difference, ΔT, between the first-order and second-order phase transitions ($\Delta T = T_c - T_m$). With a decrease of the temperature difference ΔT,

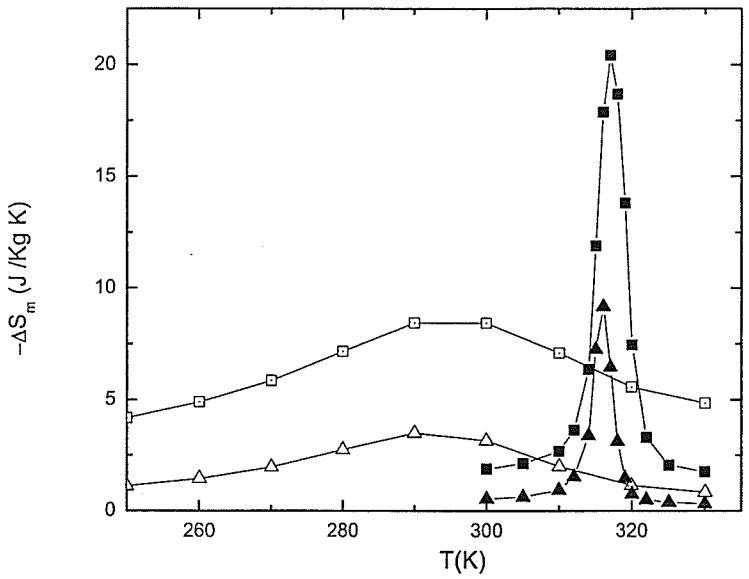

Figure 5.16 Magnetic entropy change of $Ni_{55.2}Mn_{18.6}Ga_{26.2}$ (sample 6) and Gd with temperatures at fields of 15 kOe (triangles) and 50 kOe (circles), calculated from the magnetization data. The solid squares and triangles are for $Ni_{55.2}Mn_{18.6}Ga_{26.2}$ and the open squares and triangles are for Gd.

the peak value of the magnetic entropy change keeps increasing. When T_m and T_c merge (i.e. $\Delta T = T_c - T_m \rightarrow 0$), as in sample 6, the entropy change, ΔS_M, reaches the maximum value for the group of samples studied. However, the dominant entropy change still arises from the first-order/ metamagnetic structural transition, as is evident from table 5.1; this entropy change can be further enhanced by a coincidence with a second-order/ continuous phase transition achieved through careful compositional tuning. $T_m \rightarrow T_c$ ($\Delta T \rightarrow 0$) provides a clear criterion for enhancing the magnetocaloric effect in the Ni-Mn-Ga system.

Evidence supporting this assertion is provided by an analysis of the behaviour of sample 1 given below, which possesses a pure second-order phase transition.

5.8.4 Analysis for $Ni_{57.2}Mn_{15.9}Ga_{27.0}$ (sample 1) with a pure second-order phase transition

The zero field susceptibility, measured at 2.4 kHz in an ac driving field of 30 mOe rms, is presented in figure 5.3; obviously, there is no evidence of the existence of a first-order phase transition. Figure 5.17(a) presents magnetization isotherms for sample 1 measured between liquid helium temperature and 350 K; these isotherms possess conventional shapes without any indication of an "S" shape. An Arrott plot for this specimen is shown in figure 5.17(b) by replotting the magnetization isotherms in M^2 versus H/M format; no negative slopes are observed in such plots over the entire field range measured, which also suggests that the nature of this phase transition is pure second-order. This point can be further confirmed in the insert of the upper panel of figure 5.18, which shows ac susceptibility isokaps for this specimen measured in fields between 1800 Oe and 14 kOe. These critical peaks also indicate a second-order phase transition near 310 K, as discussed earlier. Detailed critical analyses, figure 5.19, yield a set of exponents, $\gamma+\beta=1.78\pm0.03$, $\gamma=1.38\pm0.03$, $\delta=4.13\pm0.04$, which are close to the predictions of the 3D Heisenberg model

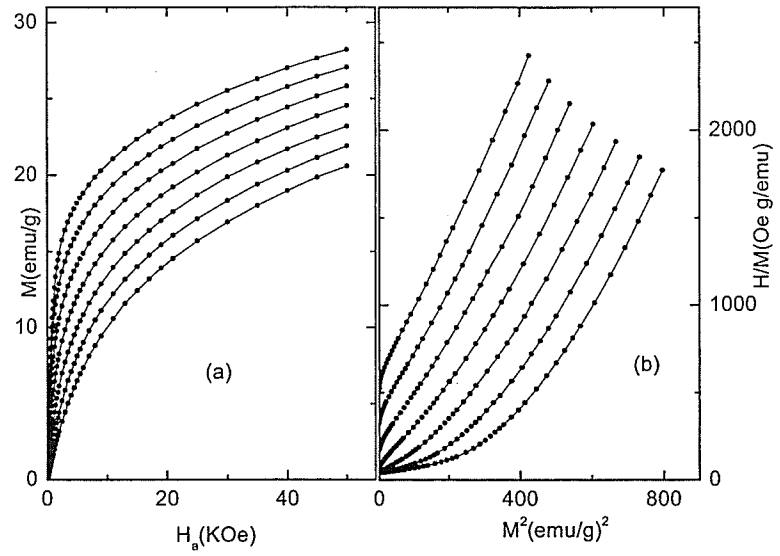

Figure 5. 17 (a) Magnetization isotherms for sample 1 from 300 K (top) to 324 K (bottom) in 4 K steps; (b) Magnetization data in figure 5.14 (a) replotted in M^2 versus H/M format.

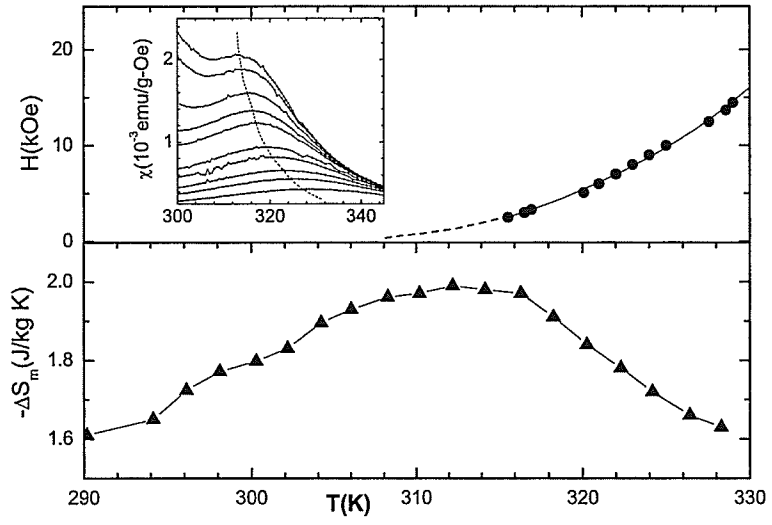

Figure 5.18 Upper panel: crossover line (T_P vs H, circles); Lower panel: ΔS_M (estimated in a field of 50 kOe) plotted against temperature for sample 1. Here there is no metamagnetic boundary as this sample has no first order transition. The upper panel insert shows ac susceptibility isokaps in static applied fields of 1800 Oe (top), 2000 Oe, 2500 Oe, 3000 Oe, 3500 Oe, 5000 Oe, 6000 Oe, 8000 Oe, 10,000 Oe and 14,000 Oe (bottom).

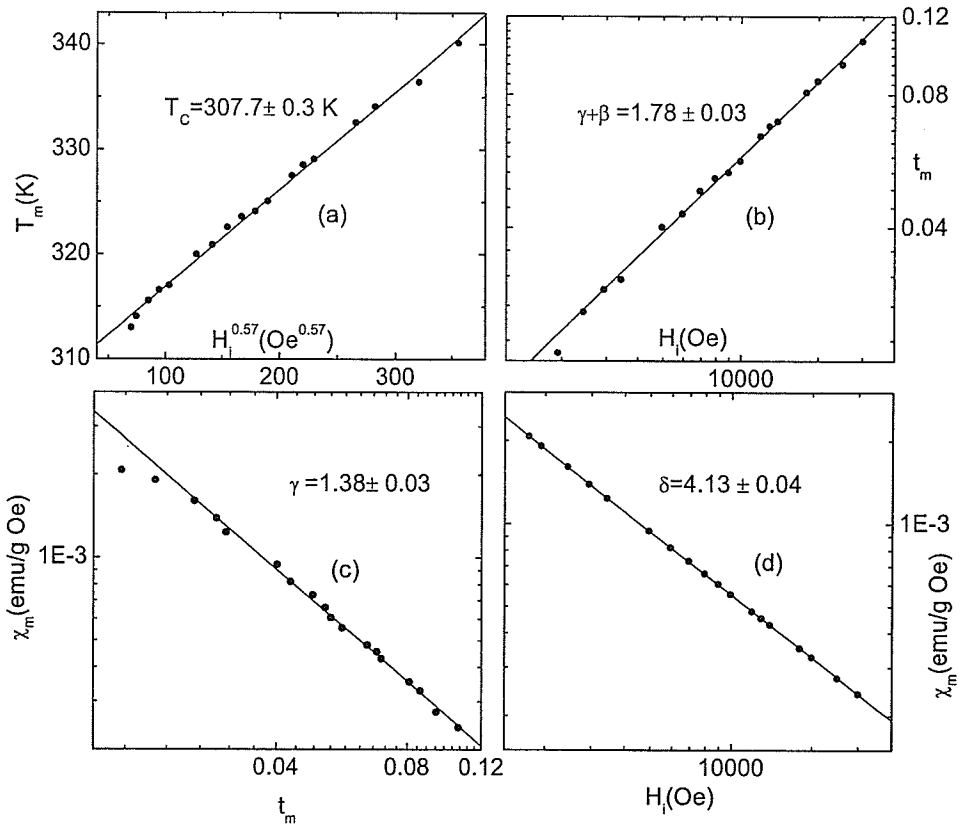

Figure 5.19 The plots show the data fit to find critical exponents values for the sample 1.

(β=0.365, γ=1.387, δ=4.8), although, for the studies earlier, a definitive identification of the universality class requires further studies. The combined plots (no metamagnetic boundary exists in this sample, the magnetization isotherms are conventional) of figure 5.18 show that the peak magnetic entropy change ΔS_m = -2.0 J kg^{-1} K^{-1} in a field of 50 kOe appears around the ordering temperature T_c =308 K,

i.e., effectively unenhanced. More importantly, in the absence of a first-order transition, the temperature dependent magnetic entropy change has a much wider peak, reaffirming the effective function of first-order transitions in this system in confining the occurrence of the magnetocaloric effect to a narrow temperature range, thus enhancing the peak value.

5.8.5 Discussion and conclusions

The merging of first- and second-order phase transitions in the Ni-Mn-Ga system leads to an enhanced magnetic entropy change; this has also been reported by other authors. In practice, this coincidence does not happen at some precise stoichiometric composition but rather it is observed over a composition range [148]. By choosing an excess of Ni, Vasil'ev et al. [19] found merged phase transitions take place in the range of $0.18 \leq x \leq 2.0$ in the series $Ni_{2+x}Mn_{1-x}Ga_x$. Using this criterion, a magnetic entropy change $\Delta Sm = -20.0$ J kg^{-1} K^{-1} in a field of 16 kOe has been reported in a $Ni_{12.9}Mn_{0.81}Ga$ sample with merged transitions [141]. Direct measurements of the temperature change accompanying the application of a field have also been made in polycrystalline sample of the same composition [149]. The present work, however, extends such studies by also varying the Ga content. In essence, the nature of the entropy change in Ni-Mn-Ga, although enhanced, is similar to that in other GMCE materials such as $Gd_5Si_2Ge_2$, $MnFeP_{0.45}As_{0.55}$ and $MnAs_{1-x}Sb_x$, which were reviewed

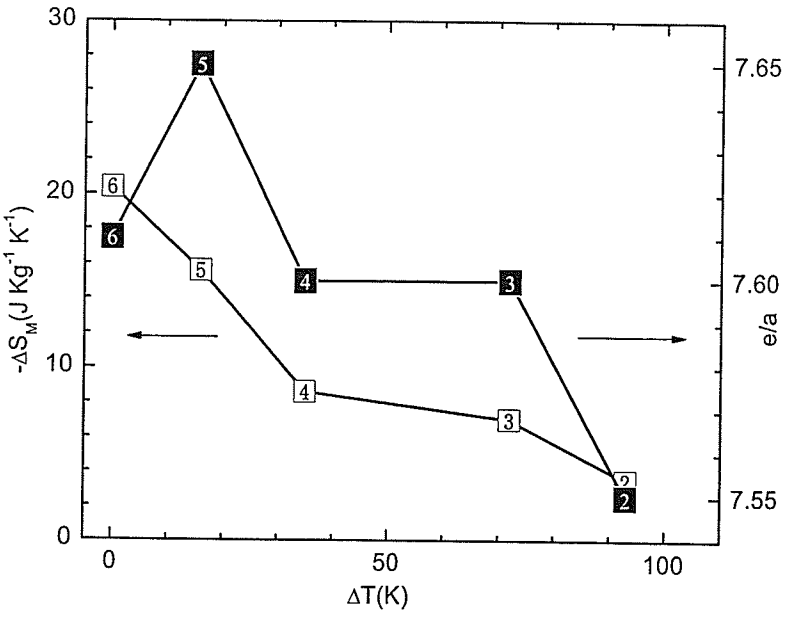

Figure 5.20 The temperature difference, ΔT, versus the maximum entropy change (open square) and ΔT versus the average number of valence electrons per atom e/a (solid square). The number inside the square shows samples index. Sample 1 is excluded in this plot since it has a second-order phase transition alone, hence no ΔT can be defined.

in the previous chapter; it originates here from a magnetostructural transition. However, the specific physical mechanism governing the magnetocaloric effect in Ni-Mn-Ga system shows some peculiarities. Recent work by Marcos et al. [150, 151] revealed that two kind of coupling mainly contribute to the MCE in this system; namely, the magnetostructural coupling between the magnetic moments and the martensitic variants (dominant in sequential transitions) and the spin-phonon coupling (dominant in merging phase transitions). Furthermore, these contributions could be suitably represented by the average number of electrons per atom, e/a, a

structurally influenced parameter; the entropy change is enhanced in this model as e/a increases and T_c-T_m approaches zero. The present data partially satisfy this criterion with the exception of the two extreme compositional specimens, as figure 5.20 shows. However, the present work focuses mainly on a quantitative appraisal of the magnetic transitions, rather than interactions on the macroscopic or microscopic scale.

In summary, by the establishment of the metamagnetic boundary at the first-order magnetic/martensitic structural transition and the crossover line at the second-order (continuous) magnetic transition, the discussion here provides a simple way to distinguish the dual character exhibited by this system. The entropy enhancement as T_m and T_c merge results from a magnetic transition displaying characteristics of both first- and second- order transitions simultaneously, rather than a co-occurrence which converts the ordering transition from second-order to first-order as claimed by [148]. The origin of the giant magnetocaloric effect (GMCE) in this system is clearly traced to the essential coincidence of these two transitions achieved by compositional tuning at $Ni_{55.2}Mn_{18.6}Ga_{26.2}$.

5.8.6 Advantages of the Ni-Mn-Ga system as a promising refrigerant

Excellent physical properties make the Ni-Mn-Ga system a promising candidate for magnetic refrigeration. In $Ni_{55.2}Mn_{18.6}Ga_{26.2}$, a magnetic entropy change ΔS_M = -20.4 J kg^{-1} K^{-1} near 317 K in a field of 50 kOe has been obtained; more importantly,

the entropy change in a relatively lower field of 15 kOe reaches ΔS_m = -9.2 J kg^{-1} K^{-1} at 317 K, which raises the possibility of operating in a field provided by a permanent magnet instead of a superconducting one. Since both the transition temperatures, T_m and T_c, are very sensitive to composition, it can be easily tuned to yield a working temperature at or above room temperature. It is also worth mentioning that the observed magnetocaloric effect in this system is reversible, which makes continuous magnetic refrigeration possible. Besides that, compared with other GMCE materials, this system does not contain the expensive rare-earth element Gd (as in the GdSiGe family) and the components of this system are abundant in nature; it also does not contain any toxic constituent such as As (present in the MnFePAs and MnAsSb systems), which makes the Ni-Mn-Ga environmentally friendly.

Although the maximum entropy change ΔS_M = -20.4 J kg^{-1} K^{-1} near 317 K in a field of 50 kOe (5 T) is amongst the largest value obtained in this system, including single crystal samples, in comparison with the maximum entropy change in other systems, such as $\Delta S_M \approx$ - 30.0 J kg^{-1} K^{-1} in the MnAs system (refer figure 5.1), there is still room for improvement. At same time, it is also important to consider the effects of magnetic hysteresis when assessing the usefulness of a material as a magnetic refrigerant. The magnetic hysteresis present in the Ni-Mn-Ga system is not favorable for continuous magnetic refrigeration. Large hysteretic losses will make the refrigeration less efficient. Preliminary studies show that hysteretic loss reduction can be realized by alloying the compound with a small amount of iron, but reducing

hysteretic losses on a larger scale is still a problem in this system. Possible mechanical instability arising from the structural transition also is an important concern for practical application. Work on these problems is ongoing.

Chapter 6

Concluding Summary

This thesis focused on two magnetic effects of some importance - the magnetoresistance and the magnetocaloric effects and their relationships to the associated magnetic phase transitions. The former involved detailed studies on two single crystal specimens - $La_{0.73}Ba_{0.27}MnO_3$ and $La_{0.73}Ca_{0.27}MnO_3$ - and a series of polycrystalline $(La_{1-x}Nd_x)_{0.67}Pb_{0.33}MnO_3$ ($0 \leq x \leq 1$) samples; the magnetocaloric studies concentrated on a series of composition related ferromagnetic shape memory alloys in the Ni-Mn-Ga system.

Critical behaviour studies on single crystal $La_{0.73}Ba_{0.27}MnO_3$ reveal the occurrence of a second-order/continuous ferromagnetic to paramagnetic phase transition near 240 K. In low and intermediate fields, a conventional critical analysis based on modified Arrott plots yields a set of exponents consistent with the 3D Heisenberg model. Estimates of the associated critical amplitudes confirm this result. Critical analysis based on an independent analysis of temperature-dependent ac susceptibility data has been performed between fields of 20 and 85 kOe and it is consistent with the above conclusions. The nature of this second-order/continuous phase transition can thus be described by the isotropic near neighbour 3D Heisenberg model, indicating

that short range interactions dominate. Such a result is consistent with model simulations for double-exchange systems, in which anisotropy does not play a significant role. A susceptibility/moment reduction near 200 K, about 45 K below the Curie temperature, is also observed in the temperature dependent ac susceptibility/ field cooled (FC) and zero field cooled (ZFC) curves in this system. This is attributed to a structural phase transition from a high moment/temperature rhombohedral (*R3c*) phase to a lower moment/temperature orthorhombic phase (*Pbmn*). Detailed measurements of the spontaneous magnetization of this sample show a marked reduction in this property below 60 K, which is consistent with a clearly discernible moment reduction, one of the few definitive conclusions about such effects provided by bulk measurements.

Detailed critical analysis of single crystal $La_{0.27}Ca_{0.73}MnO_3$ shows features characteristic of both second-order/continuous and first-order/discontinuous transitions. The latter is reflected in S-shaped magnetization isotherms, associated field-induced hysteresis and negative slopes appearing in the conventional Arrott plots; the former is associated with field modulated maxima in the ac susceptibility data. More importantly, within the experimental uncertainty, these two features are essentially coincident in the field and temperature (H_i –T) plane, a result which has never been reported previously for doped manganites. This behaviour is fundamentally different from crossover effects associated with sequential second-order to first-order transitions as $T \rightarrow T_c$, where the system approaches the ordering

temperature, T_c, from below as a second-order phase transition, but this is interrupted by a weakly first-order transition to the paramagnetic state. In this situation the power-laws discussed in chapter 2 of this thesis would be expected to occur as the transition is approached from higher (reduced) temperatures. Here these two kinds of phase transitions are essentially coincident, as the lack of power-laws confirm.

A series of polycrystalline $(La_{1-x}Nd_x)_{0.67}Pb_{0.33}MnO_3$ ($0 \leq x \leq 1$) samples have been investigated in detail in terms of both magnetic and transport behaviour. As far as the magnetic properties are concerned, the samples are ferromagnetic across the entire doping range. Critical analyses based on field and temperature dependent ac susceptibility data have been performed on all samples and revealed that the 3D Heisenberg exponents govern the paramagnetic to ferromagnetic phase transitions in samples with high Nd substitution ($x = 1.0, 0.8$). In the $x = 0.2$ sample, a set of exponents consistent with mean field predictions are obtained. Critical exponents for $x = 0.4$, extracted in the same manner, lie between 3D Heisenberg exponents and mean field model predictions. Studies of the transport behaviour reveal metal-insulator phase transitions in these samples, the temperature of which coincide with the ordering temperature. This suggests that the metal-insulator transitions are magnetically driven. Detailed analysis suggests that at high temperature, the resistivity data are best described by a variable range hopping conduction mechanism; in particular, variable range hopping appears to account for the behaviour at intermediate doping remarkably well. This may result from disorder with both spin

and site contributions in this doping regime, which in conjunction produce the necessary distribution of electronic energy levels. The substitution at the rare earth sites with fixed divalent cation doping significantly changes the average A site radius, $\langle r_A \rangle$, and the A site variance, σ^2; the disorder arising from the size mismatch and random site occupation plays a key role in controlling the magnetic and transport properties. In particular, the Curie temperature, T_c, increases linearly with increases of the average A site radius, $\langle r_A \rangle$ and with decreases in the A site variance, σ^2. With increasing $\langle r_A \rangle$, the metal-insulator transition temperature, T_{MI}, increases linearly and the corresponding maximum resistivity decreases exponentially. The relationship between the variance and maximum magnetoresistance suggests that higher disorder favours the appearance of a larger magnetoresistance in this system, contrary to what is observed in numerous other systems.

Ni-Mn-Ga ferromagnetic shape memory alloys of various compositions have been fabricated and analyzed. Results on structure, magnetism and magnetocaloric properties have been reported. Zero-field susceptibility data reveal that this system generally displays two sequential phase transitions, as in the case of the parent compound - Ni_2MnGa. On heating, these samples undergo a first-order structural transition from tetragonal martensite to cubic austenitic, causing an abrupt change in magnetization; on further heating, there is a second-order phase transition from a ferromagnetic to a paramagnetic state. However, both the type and the order of the phase transitions in this system can be tuned by varying the composition. As a result

of careful compositional tuning, a specimen, $Ni_{55.2}Mn_{18.6}Ga_{26.2}$, shows a giant magnetocaloric effect with a maximum magnetic entropy change in a field of 50 kOe which is -20.4 J kg^{-1} K^{-1} near 317 K; in a relatively low field of 15 kOe, the maximum entropy change is -9.2 J kg^{-1} K^{-1}. Both of these values are substantially larger than those of Gd. Further investigation, concentrating specifically on the relationship between the magnetic phase transitions and magnetic entropy change, particularly the establishment of the metamagnetic boundary and the crossover lines linked to the ac susceptibility peaks, show the enhanced magnetic entropy change in $Ni_{55.2}Mn_{18.6}Ga_{26.2}$ can be traced to the coincidence of a first-order/metamagnetic structural transition with a second-order / ferromagnetic continuous phase transition. For samples not at this optimal composition, which display isolated, sequential phase transitions, detailed studies suggest that the dominant entropy change occurs in the vicinity of the first-order phase transition (a combined magnetic and structural transition), just as in Gd-based $Gd_5(Si_2Ge_2)$ and transition-metals-based (MnFe)PAs magnetocaloric systems. The magnetic entropy change corresponding to the second-order phase transition possesses a much lower and wider peak than that appearing near the first-order phase transitions; this suggests that the function of the first-order phase transition is to confine the entropy change to a narrow temperature range. Excellent physical properties make the Ni-Mn-Ga system a promising candidate as a magnetic refrigerant. Since both transitions in this system are very sensitive to composition, they can be easily tuned to yield a working temperature close to or at

room temperature. In addition to the large giant magnetocaloric effect exhibited by this system, compared with other candidate magnetic refrigerants, it does not contain the expensive rare-earth element Gd (as in the GdSiGe system) nor any toxic components such as As (as in the MnFePAs and MnAsSb systems).

References:

1. Kittel, C., *Introduction to Solid State Physics*. 1996, New York: John Willey & Sons, Inc.
2. Ramirez, A.P., *Colossal magnetoresistance.* Journal of physics: Condensed matter, 1997. **9**(39): p. 8171.
3. Albert Fert, J.-M. George, H. Jaffres, R. mattana, and P. Seneor, *The new ear of spintronics.* Europhysics News, 2003. **34**(6). http://www.europhysicsnews.com/full/24/article9/article9.html
4. Millis, A.J., *Lattice effects in magnatoresistive manganese perovskites.* Nature, 1998. **392**: p. 147.
5. Zener, C., *Interaction Between the d Shells in the Transition Metals.* Phys. Rev., 1950. **81**: p. 440.
6. Anderson, P.W. and H. Hasegawa, *Considerations on double exchange.* Phys. Rev., 1955. **100**: p. 675.
7. Jonker, G. and J.V. Santen, Physics (Amsterdam), 1950. **16**: p. 337.
8. Radaelli, P.G., G. Iannone, M. Marezio, H.Y. Hwang, S.W. Cheong, J.D. Jorgensen, and D.N. Argyriou, *Structural effects on the magnetic and transport properties of perovskite A(1-x)A(x)'MnO_3 (x=0.25, 0.30).* Physical Review B, 1997. **56**(13): p. 8265-8276.
9. Radaelli, P.G., D.E. Cox, M. Marezio, S.-W. Cheong, P.E. Schiffer, and A.P. Ramirez, *Simultaneous Structural, Magnetic, and Electronic Transitions in $La_{1-x}Ca_xMnO_3$ with x=0.25 and 0.50.* Physical Review Letters, 1995. **75**: p. 4488.
10. Fontcuberta, J., B. Martinez, A. Seffar, S. Pinol, J.L. GarciaMunoz, and X. Obradors, *Colossal magnetoresistance of ferromagnetic manganites:*

Structural tuning and mechanisms. Physical Review Letters, 1996. **76**(7): p. 1122-1125.

11. Hwang, H.Y., S.-W. Cheong, N.P. Ong, and B. Batlogg, *Spin-Polarized Intergrain Tunneling in $La_{2/3}Sr_{1/3}MnO_3$.* Physical Review Letters, 1996. **77**: p. 2041.
12. Schiffer, P., A.P. Ramirez, W. Bao, and S.-W. Cheong, *Low Temperature Magnetoresistance and the Magnetic Phase Diagram of $La_{1-x}Ca_xMnO_3$.* Physical Review Letters, 1995. **75**: p. 3336.
13. Beznosov, A.B., V.A. Desnenko, E.L. Fertman, C. Ritter, and D.D. Khalyavin, *Magnetic and neutron diffraction study of $La_{2/3}Ba_{1/3}MnO_3$ perovskite manganites.* Physical Review B, 2003. **68**(5): p. 054109.
14. Warburg, E., Ann. Phys. Chem, 1881. **13**: p. 141.
15. Giauque, W.F., J. Amer. Chem. Soc., 1927. **49**: p. 1864.
16. Pecharsky, V.K. and K.A. Gschneidner, *Tunable magnetic regenerator alloys with a giant magnetocaloric effect for magnetic refrigeration from similar to 20 to similar to 290 K.* Applied Physics Letters, 1997. **70**(24): p. 3299-3301.
17. Tegus, O., E. Bruck, K.H.J. Buschow, and F.R. de Boer, *Transition-metal-based magnetic refrigerants for room-temperature applications.* Nature, 2002. **415**(6868): p. 150-152.
18. *http://mse.iastate.edu/files/elements/2002_fall_mse_elements.pdf.*
19. Vasil'ev, A.N., A.D. Bozhko, and V.V. Khovailo, *Structural and magnetic phase transitions in shape-memory alloys $Ni_{2+x}Mn_{1-x}Ga$.* Physical Review B, 1999. **59**: p. 1113.
20. Bulgadaev, S.A., *BKT phase transitions in two-dimensional systems with internal symmetries.* http://arxiv.org/abs/hep-th/9906091.
21. Toledano, J.C. and P. Toledano, The Landau theory of phase transitions. Applications to structural, incommensurate, magnetic and liquid crystals systems (1987) World Scientific, Singapore. , 1987.

22. Stanley, H.E., *Introduction to phase transition and critical phenomena.* 1971: Oxford University Press, Oxford.
23. Campostrini, M., M. Hasenbusch, A. Pelissetto, P. Rossi, and E. Vicari, *Critical exponents and equation of state of the three-dimensional Heisenberg universality class.* Physical Review B, 2002. **65**: p. 144520.
24. Campostrini, M., M. Hasenbusch, P. Rossi, and E. Vicari, *Improved high-temperature expansion and critical equation of state of three-dimensional Ising-like systems.* Physical Review E, 1999. **60**: p. 3526.
25. Campostrini, M., M. Hasenbusch, A. Pelissetto, P. Rossi, and E. Vicari, *Critical behavior of the three-dimensional XY universality class.* Physical Review B, 2002. **63**: p. 214503.
26. Ma, M., B.I. Halperin, and P.A. Lee, *Strongly Disordered Superfluids - Quantum Fluctuations and Critical-Behavior.* Physical Review B, 1986. **34**(5): p. 3136-3143.
27. Widom, B., Journal of Chemical Physics, 1965. **43**: p. 3892.
28. Domb, C. and D.L. Hunter, *On the critical behaviour of ferromagnets.* Proc. Roy. Soc. , 1965. **86**: p. 1147.
29. Patashinshii, A.Z. and V.L. Pokrovskii, Soviet JETP, 1966. **23**: p. 292.
30. Kadanoff, L.P., *Scaling laws for Ising Models near T_c.* Physics, 1966. **2**: p. 263.
31. Ho, S.C., I. Maartense, and G. Williams, *AC susceptibility and resistivity of the ferromagnetic phase of PdMn.* J. Phys. F: Met. Phys., 1981. **11**: p. 699.
32. Ho, S.C., I. Maartense, and G. Williams, *Mixed ordering in PdMn alloys.* J. Phys. F: Met. Phys., 1981. **11**: p. 1107.
33. Zhao, J.H., H.P. Kunkel, X.Z. Zhou, and G. Williams, *Critical Behavior of the Magnetoresistive Pyrochlore $Tl_2Mn_2O_7$.* Applied Physics Letters, 1999. **83**: p. 219.

34. Roshko, R.M. and G. Williams, *Comparisons of Scaling Predictions with an Sk-Like Model in the Ferromagnetic Regime.* Journal of Physics F-Metal Physics, 1984. **14**(3): p. 703-709.

35. Houvel, J.S.M., *methods for determining the Curie temperature of a ferromagnet.* General Electric Research Lab. Report No 57-RL-1799, 1957.

36. Aharoni, A., *Introduction to the theory of ferromagnetism.* 2000.

37. Banerjee, S.K., Phys. Lett., 1964. **12**: p. 16.

38. Arrott, A. and J.E. Noakes, *Approximate Equation of State For Nickel Near its Critical Temperature.* Physical Review Letters, 1967. **19**: p. 786.

39. Quantum Design, http://www.qdusa.com.

40. Quantum Design, *PPMS user manual.*

41. D, Halliday., R. Resnick, and J. Walker, *Fundamentals of Physics.* 2005: John Wiley & Sons, Inc.

42. Baibich, M.N., J.M. Broto, A. Fert, F.N.V. Dau, F. Petroff, P. Eitenne, G. Creuzet, A. Friederich, and J. Chazelas, *Giant Magnetoresistance of (001)Fe/(001)Cr Magnetic Superlattices.* Physical Review Letters, 1998. **61**: p. 2472.

43. Shimakawa, Y., Y. Kubo, T. Manako, Y.V. Sushko, D.N. Argyriou, and J.D. Jorgensen, *Structural and magnetotransport properties of the colossal magnetoresistance material $Tl_2Mn_2O_7$.* Physical Review B, 1997. **55**(10): p. 6399-6404.

44. Calderon, M.J., L.G.L. Wegener, and P.B. Littlewood, *Magnetic polarons and magnetoresistance in EuB_6.* http://arxiv.org/PS_cache/cond-mat/pdf/0312/0312437.pdf, 2005.

45. Chattopadhyay, A. and A.J. Millis, *Theory of transition temperature of magnetic double perovskites.* Physical Review B, 2001. **6402**(2): p. 024424.

46. Yakel, H.L., Acta Crystallogr., 1955. **8**: p. 394.

47. Wollan, E.O. and W.C. Koehler, *Neutron Diffraction Study of the Magnetic Properties of the Series of Perovskite-Type Compounds [(1-x)La, xCa]MnO_3.* Phys. Rev., 1955. **100**: p. 545.

48. Goodenough, J.B., *magnetism and the chemical bond (Huntington: Krieger).* 1976.

49. Shannon, R.D., Acta Crystallogr. Sec. A., 1976. **32**: p. 751.

50. Coey, J.M.D., M. Viret, L. Ranno, and K. Ounadjela, *Electron Localization in Mixed-Valence Manganites.* Physical Review Letters, 1995. **75**(21): p. 3910-3913.

51. Jahn and Teller, Proc. Roy. Soc., 1937: p. A161.

52. Peles, A., H.P. Kunkel, X.Z. Zhou, and G. Williams, *Field-dependent magnetic and transport properties and anisotropic magnetoresistance in ceramic $La_{0.67}Pb_{0.33}MnO_3$.* Journal of Physics-Condensed Matter, 1999. **11**(41): p. 8111-8130.

53. Zhao, J.H., H.P. Kunkel, X.Z. Zhou, and G. Williams, *Magnetic and transport behavior of electron-doped $La_{1-x}Mg_xMnO_3$ (0.45 <= x <= 0.6).* Physical Review B, 2002. **66**(18): p. 184428.

54. Worledge, D.C., G.J. Snyder, M.R. Beasley, T.H. Geballe, R. Hiskes, and S. Dicarolis, *Anneal-tunable Curie temperature and transport of $La_{0.67}Ca_{0.33}MnO_3$.* 1996. **80**(9): p. 5158.

55. Terea, J.M.D., K. Dorr, K.H. Muller, L. Schultz, and R.I. Chakalova, *Strong influence of the Mn_{3+} content on the binding energy of the lattice polarons in manganese perovskites.* Physical Review B, 1998. **58**: p. R5928.

56. Zhao, J.H., H.P. Kunkel, X.Z. Zhou, and G. Williams, *Magnetic and transport properties and the phase diagram of hole-doped $La_{1-x}Mg_xMnO_3$ (x <= 0-4).* Journal of Physics-Condensed Matter, 2001. **13**(41): p. 9349-9367.

57. Jakob, G., W. Westerburg, F. Martin, and H. Adrian, *Small-polaron transport in $La_{0.67}Ca_{0.33}MnO_3$ thin films.* Physical Review B, 1998. **58**(22): p. 14966-14970.

58. Kubo, K. and N. Ohata, Journal of Physical Society of Japean, 1972. **33**: p. 21.

59. Akimoto, T., Y. Moritomo, A. Nakamura, and N. Furukawa, *Observation of Anomalous Single-Magnon Scattering in Half-Metallic Ferromagnets by Chemical Pressure Control.* Physical Review Letters, 2000. **85**: p. 3914.

60. Osborn, J.A., *Demagnetizing factors of the general ellipsoid.* Physical Review B, 1945. **67**: p. 351.

61. Kim, D., B.L. Zink, F. Hellman, and J.M.D. Coey, *Critical behavior of $La_{0.75}Sr_{0.25}MnO_3$.* Physical Review B, 2002. **65**(21): p. 214424.

62. Tomioka, Y., A. Asamitsu, H. Kuwahara, Y. Moritomo, and Y. Tokura, *Magnetic-field-induced metal-insulator phenomena in $Pr_{1-x}Ca_xMnO_3$ with controlled charge-ordering instability.* Physical Review B, 1996. **53**: p. R1689.

63. Ju, H.L., J. Gopalakrishnan, J.L. Peng, Q. Li, G.C. Xiong, T. Venkatesan, and R.L. Greene, *Dependence of giant magnetoresistance on oxygen stoichiometry and magnetization in polycrystalline $La_{0.67}Ba_{0.33}MnO_z$.* Physical Review B, 1995. **52**: p. 6143.

64. Helmolt, R.V., J. Wecker, B. Holzapfel, L. Schultz, and K. Samwer, *Giant negative magnetoresistance in perovskitelike $La_{2/3}Ba_{1/3}MnO_z$ ferromagnetic films.* Physical Review Letters, 1993. **71**: p. 2331.

65. Morrish, A., *The physical principles of magnetism.* 2001: Wiley-IEEE Press.

66. Milosevic, S. and H.E. Stanley, *Equation of State near the Critical Point. I. Calculation of the Scaling Function for S=1 / 2 and S= [infinity] Heisenberg Models Using High-Temperature Series Expansions.* Physical Review B, 1972. **6**: p. 986.

67. Krasnow, R. and H.E. Stanley, *Specific-Heat Scaling Functions for Ising and Heisenberg Models and Comparison with Experiments on Nickel.* Physical Review B, 1972. **8**: p. 332.

68. Kaul, S.N., *Static critical phenomena in ferromagnets with quenched disorder.* Journal of Magnetism and Magnetic Materials, 1985. **53**(1-2): p. 5.

69. Moutis, N., I. Panagiotopoulos, M. Pissas, and D. Niarchos, *Structural and magnetic properties of $La_{0.67}(Ba_xCa_{1-x})_{(0.33)}MnO_3$ perovskites (O <= x <= 1).* Physical Review B, 1999. **59**(2): p. 1129-1133.

70. Ghosh, K., *Critical phenomena in the double-exchange ferromagnet $La_{0.7}Sr_{0.3}MnO_3$.* Physical Review Letters, 1998. **81**(21): p. 4740.

71. Alonso, J.L., L.A. Fernandez, F. Guinea, V. Laliena, and V. Martin-Mayor, *Hybrid Monte Carlo algorithm for the double exchange model.* Nuclear Physics B, 2001. **596**: p. 587.

72. Xue, Y.Y., B. Lorenz, A.K. Heilman, M. Gospodnov, S.G. Dobreva, and C.W. Chu, Preprint cond-mat/0002468, 2000.

73. Ziese, M., *Critical scaling and percolation in manganite films.* Journal of physics: Condensed Matter, 2001. **13**(13): p. 2919.

74. Aharony, A., *Critical behaviour of anisotropic cubic system.* Physical Review B, 1973. **8**: p. 3363.

75. Aharony, A. and E.F. Michael, *Critical Behavior of Magnets with Dipolar Interactions. I. Renormalization Group near Four Dimensions.* Physical Review B, 1973. **8**: p. 3323.

76. Laukhin, V., B. Martinez, J. Fontcuberta, and Y.M. Mukovskii, *Pressure effects on the structural phase transition in $La_{0.8}Ba_{0.2}MnO_3$.* Physical Review B, 2001. **63**: p. 214417.

77. Arkhipov, V.E., N.G. Bebenin, V.P. Dyakina, V.S. Gaviko, A.V. Korolev, and V.V. Mashkautsan, *Magnetic-field-driven structural transition in a $La_{0.8}Ba_{0.2}MnO_3$ single crystal.* Physical Review B, 2000. **61**: p. 11229.

78. Brown, T., W. Li, H.P. Kunkel, X.Z. Zhou, G. Williams, Y. Mukovskii, and A. Arsenov, *Anomalous temperature dependence of the spontaneous magnetization of single-crystal* $La_{0.73}Ba_{0.27}MnO_3$. Journal of physics: Condensed Matter, 2005. **17**: p. 1-10.

79. Brown, T., *Master Thesis*: *Bulk Magnetic Measurement on Single Crystal* $La_{0.73}Ba_{0.27}MnO_3$ *and Polycrystalline* $La_{0.5}Sr_{0.5}CoO_3$. 2005, University of Manitoba: Winnipeg.

80. Keffer, R., *Spin Waves, Handbuch der Physik XVIII/2*. 1996: Springer, Belin.

81. Smolyaninova, V.N., J.J. Hamilton, R.L. Greene, Y.M. Mukovskii, S.G. Karabashev, and A.M. Balbashov, *Low-temperature field-dependent magnetization of* $La_{0.7}Sr_{0.3}MnO_3$. Physical Review B, 1997. **55**(9): p. 5640-5642.

82. Chatterji, T., L.P. Regnault, and W. Schmidt, *Spin dynamics of* $La_{0.7}Ba_{0.3}MnO_3$. Physical Review B, 2002. **66**(21): p. 214408

83. Adams, C.P., J.W. Lynn, V.N. Smolyaninova, A. Biswas, R.L. Greene, W. Ratcliff, S.W. Cheong, Y.M. Mukovskii, and D.A. Shulyatev, *First-order nature of the ferromagnetic phase transition in (La-Ca)*MnO_3 *near optimal doping.* Physical Review B, 2004. **70**(13): p. 134414.

84. Lynn, J.W., R.W. Erwin, J.A. Borchers, Q. Huang, A. Santoro, J.-L. Peng, and Z.Y. Li, *Unconventional Ferromagnetic Transition in* $La_{1-x}Ca_xMnO_3$. Physical Review Letters, 1996. **76**: p. 4046.

85. Perring, T.G., G. Aeppli, S.M. hayden, S.A. Cater, J.P. Remeika, and S.-W. Cheong, *Spin Waves throughout the Brillouin Zone of a Double-Exchange Ferromagnet.* Physical Review Letters, 1996. **77**: p. 711.

86. Gennes, P.G.d., *Effects of double exchange in magnetic crystals.* Physical Review 1961. **118**: p. 141.

87. Solovyev, I.V. and K. Terakura, *Spin canting in three-dimensional perovskite manganites.* Physical Review B, 2001. **63**: p. 174425.

88. Biotteau, G., M. Hennion, R. Moussa, J. Rodriguez-Carvajal, L. Pinsard, A. Revcolevschi, Y.M. Mukovskii, and D. Shulyatev, *Approach to the metal-insulator transition in $La_{1-x}Ca_xMnO_3$ (0 <= x <= 0.2): Magnetic inhomogeneity and spin-wave anomaly.* Physical Review B, 2001. **6410**(10): p. 104421.

89. Gordon, J.E., C. Marcenat, J.P. Franck, I. Isaac, G. Zhang, R. Lortz, C. Meingast, F. Bouquet, R.A. Fisher, and N.E. Philips, *Specific heat and thermal expansion of $La_{0.65}Ca_{0.35}MnO_3$: Magnetic-field dependence, isotope effect, and evidence for a first-order phase transition.* Physical Review B, 2002. **65**: p. 024441.

90. Kim, D., B. Revaz, B.L. Zink, F. Hellman, J.J. Rhyne, and J.F. Mitchell, *Tricritical Point and the Doping Dependence of the Order of the Ferromagnetic Phase Transition of $La_{1-x}Ca_xMnO_3$.* Physical Review Letters, 2002. **89**: p. 227202.

91. Souza, J.A., Y.K. Yu, J.J. Neumeier, H. Terashita, and R.F. Jardim, *Method for analyzing second-order phase transitions: Application to the ferromagnetic transition of a polaronic system.* Physical Review Letters, 2005. **94**(20): p. 207209.

92. Mira, J., R. J., F. Rivadulla, Vazquez-Vazquez, and M.A. Lopez-Quintela, *Change from first- to second-order magnetic phase transition in $La_{2/3}(Ca,Sr)_{(1/3)}MnO_3$ perovskites.* Physical Review B, 1999. **60**(5): p. 2998.

93. Hong, C.S., W.S. Kim, and N.H. Hur, *Transport and magnetic properties in the ferromagnetic regime of $La_{1-x}Ca_xMnO_3$.* Physical Review B, 2001. **6309**(9): p. art. no.-092504.

94. Shulyatev, D., D. Darabashev, A. Arsenov, and Y.M. Mukovskii, *Growth and investigation of doped rare earth manganite single crystals* Journal of Crystal Growth, 1999. **199**: p. 511.

95. Stampe, P.A., X.Z. Zhou, H.P. Kunkel, J.A. Cowen, and G. Williams, *Anomalous magnetoresistance near the metamagnetic transition in Gd_2In.* Journal of Physics-Condensed Matter, 1997. **9**(18): p. 3763-3777.

96. Kunkel, H.P., X.Z. Zhou, P.A. Stampe, J.A. Cowen, and G. Williams, *Giant magnetoresistive behavior near the metamagnetic transition in $Ce(Fe_{0.93}Ru_{0.07})(2)$.* Physical Review B, 1996. **53**(22): p. 15099-15105.

97. Huang, K., *Statistical mechanics*. 1987: New York: Wiley.

98. Rivadulla, F., J. Riva, and J.B. Goodenough, *Suppression of the magnetic phase transition in manganites close to the metal-insulator crossover.* Physical Review B, 2004. **70**: p. 172410.

99. Young, S.L., H.Z. Chen, C.H. Lin, L. Horng, J.B. Shi, and Y.C. Chen, *Magnetization processes in polycrystalline $(La_{0.7-x}Nd_x)Pb_{0.3}MnO_3$.* Journal of Magnetism and Magnetic Materials, 2002. **239**(1-3): p. 70-72.

100. Gutierrez, J., J.M. Barandiaran, M. Insausti, A. Lezama, A. Pena, J.J. Blanco, and T. Rojo, *Magnetic and transport properties of Pb perovskites and Fe containing giant magnetoresistance perovskites.* Journal of Applied Physics, 1998. **83**(11): p. 7171-7173.

101. Ghosh, N., S. Elizabeth, H.L. Bhat, G.N. Subanna, and M. Sahana, *Crystal growth, structural and magnetic properties of $Nd_{1-x}Pb_xMnO_3$.* Journal of Magnetism and Magnetic Materials, 2003. **256**(1-3): p. 286-292.

102. Ghosh, N., S. Elizabeth, H.L. Bhat, U.K. Rossler, K. Nenkov, S. Rossler, K. Dorr, and K.H. Muller, *Effect of rare-earth-site cations on the physical properties of $La_{0.7-y}NdyPb_{0.3}MnO_3$ single crystals.* Physical Review B, 2004. **70**(18): p. 184436.

103. Munoz, A., J.A. Alonso, M.J. Martinez-Lope, J.L. Garcia-Munoz, and M.T. Fernandez-Diaz, *Magnetic structure evolution of $NdMnO_3$ derived from neutron diffraction data.* Journal of Physics-Condensed Matter, 2000. **12**(7): p. 1361-1376.

104. Zhao, J.H., T. Song, H.P. Kunkel, X.Z. Zhou, R.M. Roshko, and G. Williams, *$La_{0.95}Mg_{0.05}MnO_3$: an ideal ferromagnetic system?* Journal of Physics-Condensed Matter, 2000. **12**(30): p. 6903-6918.

105. Williams, G., *Critical behaviour of some perovskites and pyrochlores: what's unusual and what's not.* Journal of Alloys and Compounds, 2001. **326**(1-2): p. 36-46.

106. Wang, Z., H.P. Kunkel, and G. Williams, *Ac-Susceptibility of the Dilute Pdfe System.* Journal of Physics-Condensed Matter, 1992. **4**(50): p. 10385-10398.

107. Sahana, M., U.K. Rossler, N. Ghosh, S. Elizabeth, H.L. Bhat, K. Dorr, D. Eckert, M. Wolf, and K.H. Muller, *Critical properties of the double-exchange ferromagnet $Nd_{0.6}Pb_{0.4}MnO_3$.* Physical Review B, 2003. **68**(14): p. 144408.

108. RodriguezMartinez, L.M. and J.P. Attfield, *Cation disorder and size effects in magnetoresistive manganese oxide perovskites.* Physical Review B, 1996. **54**(22): p. 15622-15625.

109. Hwang, H.Y., S.W. Cheong, P.G. Radaelli, M. Marezio, and B. Batlogg, *Lattice Effects on the Magnetoresistance in Doped Lamno3.* Physical Review Letters, 1995. **75**(5): p. 914-917.

110. Coey, J.M.D., M. Viret, and S. von Molnar, *Mixed-valence manganites.* Advances in Physics, 1999. **48**(2): p. 167-293.

111. Ziese, M. and C. Srinitiwarawong, *Polaronic effects on the resistivity of manganite thin films.* Physical Review B, 1998. **58**(17): p. 11519-11525.

112. Viret, M., L. Ranno, and J.M.D. Coey, *Colossal magnetoresistance of the variable range hopping regime in the manganites.* Journal of Applied Physics, 1997. **81**(8): p. 4964-4966.

113. Appel, J., *Solid State Physics* Vol. 21. 1968: New York: Academic.

114. Mott, N., *Conduction in Non Crystalline Materials.* 1993: Oxford: Clarendon. 17ff.

115. Hasanain, S.K., M. Nadeem, W.H. Shah, M.J. Akhtar, and M.M. Hasan, *Effects of iron doping on the transport and magnetic behaviour in* $La_{0.65}Ca_{0.35}Mn_{1-y}Fe_yO_3$. Journal of Physics-Condensed Matter, 2000. **12**(42): p. 9007-9017.

116. Laiho, R., K.G. Lisunov, E. Lahderanta, V.N. Stamov, and V.S. Zakhvalinkshi, *Variable-range hopping conductivity in* $La_{1-x}Ca_xMnO_3$. Journal of Physics: Condensed Matter, 2001. **13**: p. 1233.

117. Viret, M., L. Ranno, and J.M.D. Coey, *Magnetic localization in mixed-valence manganites.* Physical Review B, 1997. **55**(13): p. 8067-8070.

118. Crespi, V.H., L. Lu, Y.X. Jia, K. Khazeni, A. Zettl, and M.L. Cohen, *Thermopower of single-crystal* $Nd_{1-x(}Sr,Pb)_{(x)}MnO_{3-delta}$. Physical Review B, 1996. **53**(21): p. 14303-14308.

119. Pecharshy, V.K. and J. K. A. Gschneidner, *Giant Magnetocaloric Effect in* $Gd_5(Si_2Ge_2)$. Physical Review Letters, 1996. **78**: p. 4494.

120. Cooke, A.H., Proc. Roy. Soc. A, 1950. **62**: p. 269.

121. Bleaney, B., Proc. Roy. Soc. A, 1950. **204**: p. 203.

122. Buchal, C., K.J. Fisher, M. Kubota, R.M. Mueller, and F. Pobell, J. Phys. Lett., 1978. **39**: p. L457.

123. Annaorazov, M.P., S.A. Nikitin, A.L. Tyurin, K.A. Asatryan, and A.K. Dovletov, *Anomalously high entropy change in FeRh alloy.* Journal of Applied Physics 1996. **79**(3): p. 1689.

124. Provenzano, V., A.J. Shapiro, and R.D. Shull, *Reduction of hysteresis losses in the magnetic refrigerant* $Gd_5Ge_2Si_2$ *by the addition of iron.* Nature, 2004. **429**(6994): p. 853-857.

125. Gschneidner, K.A. and V.K. Pecharsky, *Magnetocaloric materials.* Annual Review of Materials Science, 2000. **30**: p. 387-429.

126. Wada, H., K. Taniguchi, and Y. Tanabe, *Extremely Large Magnetic Entropy Change of $MnAs_{1-x}Sb_x$ near Room Temperature* Materials Transcations, 2002. **43**(1): p. 73.

127. Wada, H. and Y. Tanabe, *Giant magnetocaloric effect of $MnAs_{1-x}Sb_x$.* Applied Physics Letters, 2001. **79**(20): p. 3302.

128. Goto, T., M.I. Bartashevich, K. Kondo, K. Terao, H. Yamada, and H. Ido, *Magnetic properties of $MnAs_{0.7}Sb_{0.3}$ under high pressure Comparison with the magnetic moment calculated for MnAs with the NiAs-type structure* Journal of Alloys and Compounds, 2001. **325**: p. 18.

129. Hu, F.-X., S. Bao-gen, J.-r. sun, and W. Guang-heng, *Large magnetic entropy change in a Heusler alloy $Ni_{52.6}Mn_{23.1}Ga_{24.3}$ single crystal.* Physical Review B, 2001. **64**: p. 132412.

130. Zhou, X.Z., W. Li, H.P. Kunkel, and G. Williams, *A criterion for enhancing the giant magnetocaloric effect: (Ni-Mn-Ga) - a promising new system for magnetic refrigeration.* Journal of Physics-Condensed Matter, 2004. **16**(6): p. L39-L44.

131. Brown, G.V., *Magnetic heat pumping near room temperature.* Journal of Applied Physics 1976. **47**(8): p. 3673.

132. Zimm, C., A. Jastrab, A. Stemberg, V. Pecharsky, J. K. A. Gschneidner, M. Osborne, and I. Anderson, Advances in Cryogenic Engineering, 1998. **43**: p. 1759.

133. Pecharsky, V.K. and K.A.G. Jr., *Magnetocaloric effect and magnetic refrigeration.* Journal of Magnetism and Magnetic Materials, 1999. **200**(1-3): p. 44.

134. Giguere, A., M. Foldeaki, B.R. Gopal, R. Chahine, T.K. Bose, A. Frydman, and J.A. Barclay, *Direct Measurement of the "Giant" Adiabatic Temperature Change in $Gd_5Si_2Ge_2$.* Physical Review Letters, 1999. **83**: p. 2262.

135. Pecharsky, V.K., K.A. Gschneider, A.O. Pecharsky, and A.M. Tishin, *Thermodynamics of the magnetocaloric effect.* Physical Review B, 2001. **6414**(14): p. 144406.

136. James, R.D. and M. Wuttig, *Magnetostriction of Martensite.* Philosophical Magazine, 1998. **77A**: p. 1273.

137. Kakeshita, T., K. Shimizu, S. Funada, and M. Date, *Magnetic field-induced martensitic transformations in disordered and ordered Fe-Pt alloys.* Transactions of Japan Institute of Metals, 1984. **25**: p. 837.

138. Oikawa, K., L. Wulff, T. Iijima, G. Gejima, T. Ohmori, A. Fujita, K. Fukamichi, R. Kainuma, and K. Ishid, *Promising ferromagnetic Ni-Co-Al shape memory alloy system.* Applied Physics Letters, 2001. **81**: p. 3290.

139. Ullakko, K., J.K. Huang, C. Kantner, C. O'handley, and V.V. Kokorin, *Large magnetic-field-induced strains in Ni_2MnGa single crystals.* Journal of Applied Physics Letters, 1996. **69**: p. 1966.

140. O'Handley, R.C., *Model for strain and magnetization in magnetic shape-memory alloys.* Journal of Applied Physics, 1998. **83**: p. 3263.

141. Parcti, L., M. Solzi, F. Albertini, and A. Paoluzi, *Giant entropy change at the co-occurrence of structural and magnetic transitions in the $Ni_{2.10}Mn_{0.81}Ga$ Heusler alloy.* Eur. Phys. J. B, 2003. **32**: p. 303.

142. Wirth, S., A. Leithe-Jasper, A.N. Vasil'ev, and J.M.D. Coey, *Structural and magnetic properties of Ni_2MnGa* Journal of Magnetism and Magnetic Materials, 1997. **167**(1-2): p. L7.

143. Casanova, F., A. Labarta, X. Batlle, J. Marcos, L. Manosa, A. Planes, and S.d. Brion, *Effect of a magnetic field on the magnetostructural phase transition in $Gd_5(Si_xGe_{1-x})_4$.* Physical Review B, 2004. **69**: p. 104416.

144. Levin, E.m., V.K. Pecharsky, and J. K. A. Gschneidner, *Unusual magnetic behavior in $Gd_5(Si_{1.5}Ge_{2.5})$ and $Gd_5(Si_2Ge_2)$* Physical Review B, 2000. **62**: p. R14625.

145. Wada, H., Y. Tanabe, K. Hagiwara, and M. Shiga, *Magnetic phase transition and magnetocaloric effect of $DyMn_2Ge_2$* Journal of Magnetism and Magnetic Materials, 2000. **218**: p. 203.

146. Kunkel, H.P., R.M. Roshko, and G. Williams, *Field-Dependent Susceptibility of a Paramagnet.* Physical Review B, 1988. **37**(10): p. 5880-5883.

147. Enkovaara, J., A. Ayuela, L. Nordstrom, and R.M. Nieminen, *Magnetic anisotropy in Ni_2MnGa.* Physical Review B, 2002. **65**: p. 134422.

148. Albertini, F., F. Canepa, S. Cirafici, E.A. Franceschi, M. Napoletano, A. Paoluzi, L. Pareti, and m. Solzi, *Composition dependence of magnetic and magnetothermal properties of Ni-Mn-Ga shape memory alloys.* Journal of Magnetism and Magnetic Materials, 2004. **272-276**: p. 2111.

149. Aliev, A., A. Batdalov, S. Bosko, V. Buchelnikov, I. Dikshtein, V. Khovailo, V. Koledov, R. Levitin, V. Shavrov, and T. Takagi, *Magnetocaloric effect and magnetization in a Ni-Mn-Ga Heusler alloy in the vicinity of magnetostructural transition.* Journal of Magnetism and Magnetic Materials, 2004. **272-76**: p. 2040-2042.

150. Marcos, J., L. Manosa, A. Planes, F. Casanova, X. Batlle, and A. Labarta, *multiscale origin of the magnetocaloric effect in Ni-Mn-Ga shape-memory alloys.* Physical Review B, 2003. **68**: p. 094401.

151. Marcos, J., L. Manosa, A. Planes, F. Casanova, X. Batlle, A. Labarta, and B. Matinez, *Magnetocaloric and shape-memory effects in Ni-Mn-Ga ferro-magnetic alloys.* Journal De Physique Iv, 2004. **115**: p. 105-110.